POLITECNICO DI MILANO

Scuola di Ingegneria Industriale e dell'Informazione

Corso di Laurea Magistrale in Ingegneria Aeronautica

DROPLET-WALL INTERACTION MODELLING FOR IN-FLIGHT ICE ACCRETION

Relatore: Prof. Alberto GUARDONE

Co-relatori: Ing. Gianluca PARMA
Ing. Marta ZOCCA

Tesi di laurea di:
Giorgia CAMAULI
Matr. 852673

Anno Accademico 2016 - 2017

A mamma, papà, Andrea

Abstract

Ice accretion is one of the main concerns about in-flight applications and it plays a crucial role in aircraft design and safety requirements. When an aircraft or rotorcraft flies in cold wet air, water collected from clouds may freeze on its surfaces, leading to a degradation of aerodynamic performances which may severely compromise controllability and passengers safety. Ice protection systems improve safety standards, but their design requires a deep knowledge of the icing phenomenon and an accurate prediction of the related performance degradation. In this context, the challenge of an improvement of numerical ice accretion prediction tools arises and the present work stems from this need. The framework for ice accretion simulations developed at Politecnico di Milano is updated by merging the open-source suite SU2 for the computation of the flow field and the in-house codes performing the computation of particle trajectories (PoliDrop) and ice accretion (PoliMIce). In particular, the present thesis improves the particle tracking code including a more detailed description of the behaviour of Supercooled Large Droplets (SLD). These droplets, due to their bigger dimension, have a greater tendency to deform under the influence of aerodynamic shear forces and they are more likely to splash or rebound upon impact on the surface. If this happens, only a portion of the approaching mass is deposited at the predicted impingement location while the splashed or rebounded mass fraction is re-introduced into the flow field. This may potentially result in re-impingements on aerodynamic surfaces located downstream of the impact position. Different drag coefficients for droplets and droplet-wall interaction models are implemented in the particle tracking code and results are compared with reference solutions and experimental data in order to assess their accuracy. A modified splashing model is introduced, which leads to a significant improvement in the collection efficiency computation. Conversely, the rebound model is used to simulate the behaviour of Super Hydrophobic Surfaces (SHS), whose surface roughness can be exploited in the design of anti-icing systems. Particle tracking simulations are performed to study the influence of different flight and atmospheric conditions on the impingement limits and on the effectiveness of two different SHS.

Keywords: ice accretion, PoliMIce, SU2, PoliDrop, droplet-wall interaction models, splash, rebound, supercooled large droplets, SLD, super hydrophobic surfaces, SHS.

Sommario

L'accrescimento di ghiaccio è uno dei principali problemi in campo aeronautico e riveste un ruolo fondamentale nella progettazione di velivoli per quanto riguarda i requisiti di sicurezza. Quando un velivolo vola in aria fredda e umida, l'acqua presente nelle nuvole può impattare sulla sua superficie e congelare, causando un degrado delle prestazioni aerodinamiche che può compromettere la controllabilità del velivolo e la sicurezza dei passeggeri. I sistemi anti-ghiaccio migliorano gli standard di sicurezza, ma una corretta progettazione richiede una profonda conoscenza del fenomeno dell'icing e una previsione accurata del degrado delle prestazioni. In questo contesto nasce la necessità di migliorare i codici numerici per la previsione dell'accrescimento di ghiaccio, da cui deriva il lavoro qui presentato. La piattaforma per simulare l'accrescimento di ghiaccio sviluppata al Politecnico di Milano è stata aggiornata interfacciando il software open-source SU2 per il calcolo del campo di moto con i codici per il calcolo delle traiettorie delle gocce (PoliDrop) e dell'accrescimento di ghiaccio (PoliMIce). In particolare, la tesi migliora il codice di calcolo delle traiettorie, includendo una descrizione più accurata del comportamento delle Supercooled Large Droplets (SLD). A causa delle loro dimensioni, queste gocce presentano una maggiore tendenza a deformarsi per effetto degli sforzi aerodinamici ed è inoltre più probabile che si verifichino fenomeni di splash e rimbalzo a seguito dell'impatto sulla parete. Se ciò avviene, solo una porzione della goccia incidente viene depositata sulla superficie, mentre una frazione della massa viene reimmessa nella corrente sotto forma di gocce secondarie. Ciò può provocare successivi impatti sulle superfici aerodinamiche poste a valle. Diversi modelli per il coefficiente di resistenza della goccia e per l'interazione goccia-parete sono stati implementati nel codice di tracciamento delle traiettorie e i risultati sono stati confrontati con soluzioni di riferimento e dati sperimentali per valutarne l'accuratezza. Il modello introdotto per lo splash permette di ottenere un notevole miglioramento nel calcolo della collection efficiency, mentre il modello di rimbalzo è stato usato per simulare il comportamento di superfici superidrofobe (SHS), la cui rugosità superficiale può essere utilizzata per progettare sistemi anti-ghiaccio. Sono quindi state effettuate simulazioni per studiare l'influenza di diverse condizioni di volo e atmosferiche sui limiti di impatto e sull'efficacia di due diverse SHS.

Parole chiave: accrescimento di ghiaccio, PoliMIce, SU2, PoliDrop, interazione goccia-parete, splash, rimbalzo, supercooled large droplets, SLD, superfici superidrofobe, SHS.

Contents

List of Symbols

CFD	Computational Fluid Dynamics
LWC	Liquid Water Content
MVD	Median Volume Diameter
SHS	Super Hydrophobic Surface
SLD	Supercooled Large Droplet
A	Area
B	Ice layer thickness
C_D	Drag coefficient
d	Parcel diameter
h	Water layer thickness
H	Dimensionless water film thickness
L	Latent heat
m	Mass
$\dot{m}$	Mass flow
N_s	Number of secondary droplets
P	Pressure
$\dot{Q}$	Heat transfer
R_a	Surface roughness amplitude
R_w	Surface roughness wavelength
R	Dimensionless roughness parameter
s	Curvilinear abscissa
t	Time
T	Temperature
$\mathbf{u_p}$	Parcel velocity
$\mathbf{u_f}$	Flow field velocity
u_n	Normal velocity component
u_t	Tangential velocity component
V_∞	Airspeed
$\mathbf{x_p}$	Parcel position
z	Distance from the surface

Ca	Capillary number
K_c	Cossali parameter
K_y	Yarin and Weiss splashing parameter
M	Mach number
Oh	Ohnesorge number
Re	Reynolds number
We	Weber number
α	Airfoil angle of attack
β	Collection efficiency
θ	Contact angle
Θ	Water layer temperature
λ	Thermal conductivity
μ	Dynamic viscosity
ξ	Parcel incidence angle
ρ	Density
σ	Surface tension
φ	Parcel impact angle
Φ	Mass loss coefficient

List of Figures

List of Tables

Chapter 1

Introduction

Ice accretion is one of the main concerns in aircraft flight and it plays a crucial role in aircraft design and safety prevention. Indeed, when an aircraft or rotorcraft flies in cold wet air, water collected from clouds may freeze on its surfaces, leading to an increase of the total weight. Moreover, ice formed on lifting surfaces could degrade aerodynamic performances [1]: passive drag increases, resulting in a corresponding increase in fuel consumption, while the lift coefficient is decreased and the stall angle might undergo considerable reductions, which may cause troubles in aircraft stability and manoeuvrability [2]. Furthermore, localised ice structures accumulating on the external sensors may cause misleading information to be conveyed to the pilot and ice accreting on the inner mechanisms might lock control surfaces leading to a total loss of control. As far as the operation of engines is concerned, ice accretion on the engine nacelle may alter the airflow in the inlet manifold, whereas the ice accumulating on rotating devices possibly gives rise to aerodynamic and structural load unbalancing and to shedding phenomena [3]. Icing may severely compromise aircraft controllability and passengers safety leading to the occurrence of a number of in-flight accidents every year.

The interest towards ice accretion prediction is not only limited to aeronautical engineering, but it is relevant also in nautical, civil and energy production applications. For instance, ice accretion on blades reduces the efficiency of wind turbines operating in cold environments [4], on the top of mountains or in the Arctic sea, or can damage slender structures such as cables and antennas because of overloads and destructive aeroelastic phenomena activated under the action of the atmospheric wind [5].

All the listed reasons claim for effective tools to deal with the ice accretion problem. Icing research began in the late 1920s and early 1930s, but it was not until the World War II that icing was seriously addressed in response to the war effort and the first icing tunnels were built [6]. Since the 1940s, several experiments have been performed to investigate the physics behind structural icing and to measure icing effects on the lift and drag of airfoils or on the overall aircraft performance parameters.

The modern icing research program started in 1978 at NASA Glenn Research Center. Here, the first flow field measurements were performed and Computational Fluid Dynamics (CFD) began to be developed and applied to the prediction of aerodynamic performances of iced airfoils. In 1994 the Roselawn ATR-72 accident reinforced the importance of the aerodynamics research on icing and changed its focus from a mere scientific exercise to one clearly focused on aircraft safety. This includes experimental and computational investigations of different types of ice accretions in order to identify the most critical conditions and develop more effective ice protection systems.

Figure 1.1: In-flight ice accretion testing on a rotorcraft. Ref. [7]

For a reliable investigation, suitable and accurate tools are needed, that may help researchers and engineers to tackle the ice accretion problem. Flight tests, wind tunnel tests and numerical simulations are complementary approaches to the study of ice accretion, applied to different extents in each design step. Flight tests are very expensive as they require the aircraft or rotorcraft to fly behind another craft spraying water droplets behind it so as to reproduce the cloud conditions (Fig. 1.1). Moreover, measurements during flight tests are difficult and often inaccurate, while wind tunnels icing tests require special wind tunnels that can operate at low temperatures, so that their cost is much higher than usual aeronautical wind tunnels. Although flight and wind tunnel tests cannot be totally replaced in the certification phase, in the design phase numerical simulations can be used in place of experimental tests in order to reduce economic costs. The aims of an ice accretion software are diverse and nowadays it represents a fundamental tool in aircraft design. It can be used to predict ice shapes, to investigate performances degradation of the lifting surfaces and to help the design of anti-icing prevention systems.

1.1 Physics of ice accretion

Aircraft icing is defined as flight in clouds at temperatures at or below the freezing point of water, when supercooled water droplets impinge and freeze on the unprotected areas of the aircraft. However, ice accretion generated from clouds of supercooled water droplets does not represent the only natural hazard to the aircraft. It is also likely that the aircraft would encounter other forms of ice-producing precipitations, such as drizzle rain and snow.

Precipitations occur when a portion of the atmosphere becomes saturated with water vapour and it condenses and precipitates. According to Mason [8], water vapour normally begins to condense on condensation nuclei to form clouds. Condensation nuclei, also known as ice nucleating particles, are particles dissolved in air which catalyse ice accretion. They might be constituted by mineral powder, volcanic ash, aerosol, dust or previously accreted ice droplets. When the temperature drops under the freezing temperature, water droplets condensed on nuclei should freeze and form ice. Nevertheless, due to their relatively small size, cloud droplets may frequently exist in the supercooled state, that is to say that water will remain liquid down to 253 K and, less frequently, as low as 243 to 238 K in case of very small droplets of a few micrometres diameter. These supercooled droplets will freeze spontaneously at temperatures below 233 K, or if a perturbation of their unstable equilibrium condition occurs. This perturbation may be caused by the collision with an ice particle, an ice nucleus or by the impact on the surface of an aircraft flying in the cloud [9]. Indeed, when a forward-facing component of an aircraft such as a wing leading edge passes through the supercooled droplet cloud, the impinging droplets will try to release their latent heat and freeze to form ice accretion.

The rate and the amount of ice accretion over an unheated surface depends on different parameters such as the shape, the surface finish and the local curvature, on the speed at which the body is travelling, the temperature, the liquid water content and the size of the droplets in the cloud. It is convenient to split ice accretion in two distinct stages. The first one is related to the rate at which the water droplets are intercepted by the body. This is given by the product of the efficiency of collision of water droplets on the body, the amount of water contained in the cloud and the speed of the body through the cloud. Whereas the second one is related to the rate at which the impinging water will freeze to form the ice accretion and it is primarily governed by the heat transfer between the surface of the body and the surrounding air.

1.1.1 Parameters governing ice accretion

Collection efficiency (β)

The local value of the collection efficiency β represents the fraction of the freestream water content which impacts at a given surface location of the body. Given the trajectories of the particles, it is possible to calculate the collection efficiency using different procedures. Anyhow, all the methods relate the initial cross-sectional area of the droplet stream tube to the impact area on the surface.

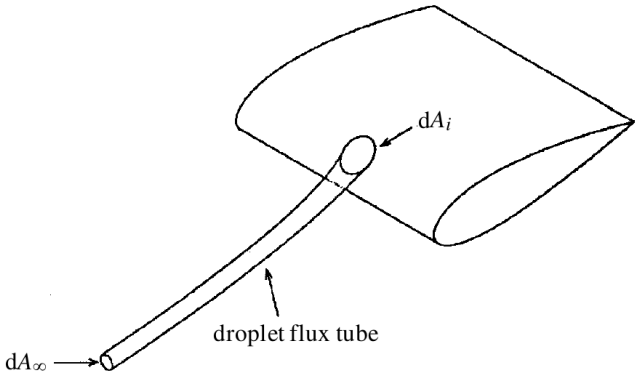

Figure 1.2: Definition of the local collection efficiency on a 3D geometry, Ref. [10].

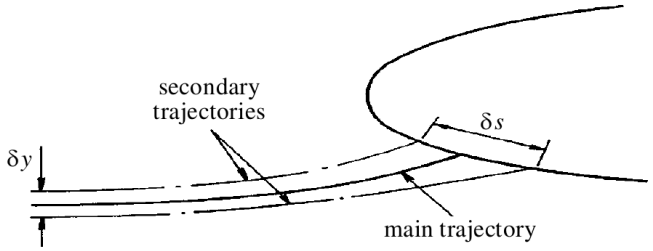

Figure 1.3: Definition of the local collection efficiency on a 2D surface, Ref. [10].

On three-dimensional geometries the collection efficiency can be defined as the ratio between the area far upstream A_∞ and the area on the surface enclosed by the same droplet trajectories A_i (Fig. 1.2):

$$\beta = \frac{dA_\infty}{dA_i} \tag{1.1}$$

In two-dimensional geometries, instead, given a main droplet trajectory, the collection efficiency is approximated as the ratio of the separation between two secondary trajectories in the freestream y_∞ to their separation at impact on the surface s (Fig. 1.3):

$$\beta = \frac{dy_\infty}{ds} \tag{1.2}$$

The collection efficiency is one of the most important parameters in the ice accretion process because it is strictly related to the accretion rate. It represents the distribution of the water collected by the surface from the cloud and can be an index of the extension of the area which will be affected by the ice accretion. Typically, the distribution has a peak close to the aerodynamic stagnation point and reduces to zero at some aft location on the upper and lower surfaces of the body. The locations where β reaches zero value are referred to as impingement limits. Typical values of the collection efficiency go from 0 for the clean surface to 0.8 in proximity of the stagnation point. High values of β are related to high values of the ice-accretion rate.

Liquid Water Content (LWC)

The Liquid Water Content (LWC) is defined as the mass of water per cubic metre of air. The term "liquid" reflects the supercooled nature of the droplets and also acts to distinguish water droplets from ice crystals. In terms of the ice accretion process, the LWC affects both the type of ice accretion and the rate at which the accretion forms. Intuitively, it is possible to say that in general the mass of water at the surface of the body will increase linearly with the LWC. Hence the greater the LWC, the greater is the potential for a large accumulation of ice. However, this is not strictly correct, since the collection efficiency will have an equally important significance in determining the actual mass of water impinging on the surface. Typical values of the LWC are between 0.2 and 1.5 g/m^3 depending on the type of cloud, as it is shown in Tab. 1.1.

Cloud type	**LWC** $[g/m^3]$
Cirrus	0.002-0.03
Fog	0.06
Cumulus	0.26-0.30
Stratus	0.28-0.30
Stratocumulus	0.44
Cumulonimbus	1.0-3.0

Table 1.1: Typical values of LWC in different cloud types, Ref. [11].

Median Volume Diameter (MVD)

The Median Volume Diameter (MVD) of the cloud is defined as the median value of the probability distribution of the diameters of the droplets. This means that half the mass and volume of water contained in the cloud is in the shape of parcels

with diameter above the MVD, while the remaining part consists in droplets with diameter below the MVD. Hence, droplets with diameter below the MVD may be numerous in the cloud, but the mass of water associated with them will be small. On the contrary, droplets with diameter bigger than the MVD may be present in the cloud, but they will be relatively few in number. However, as a rough approximation, the maximum diameter of droplets in a cloud is usually of the order of twice the MVD. Typical values of the MVD are between 15 and 40 μm and droplets with higher values are called Supercooled Large Droplets (SLD). The diameter of the droplets directly affects the collection efficiency as it shown in Fig. 1.4. In fact, the mass of a water droplet is proportional to the cube of its diameter, whereas the influence of the airflow on the droplet is proportional to the square of the diameter. As a consequence, droplets with a large diameter will follow straighter trajectories due to the dominant effect of inertial forces, while the trajectories of small droplets will be more affected by the local aerodynamic forces, resulting in a lower collection efficiency.

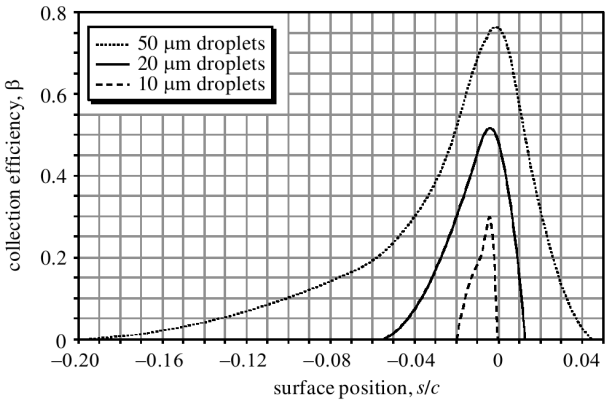

Figure 1.4: Collection efficiency as a function of the Median Volume Diameter, Ref. [10].

Airspeed (V_∞)

The primary influence of the airspeed in terms of icing severity lies in the fact that the higher is the airspeed, the greater is the intercepted volume of air in a given time and hence the greater is the mass of water that impacts on the body surface. It is thus the product of the LWC, the collection efficiency and the airspeed which determines the mass of water that impacts on the surface. However, high speed may also lead to a small ice thickness, as the portion of water which does not freeze instantaneously is drifted away by the high shear at the wall. Another effect of the airspeed to be considered is the kinetic heating induced by high velocities. The higher is the kinetic energy of impinging parcels, the more the surface is heated and the less ice accretes on the body.

Heat transfer ($\dot{Q}$)

For the impacting water droplets to freeze, their latent heat of fusion must be released through the body surface and the surrounding air. This heat transfer includes kinetic heating, convective cooling, evaporative cooling, latent heat of freezing and a number of smaller contributions from sensible heating and cooling mechanisms. The heat fluxes involved are:

- $\dot{Q}_l = \rho_i L_f \frac{\partial B}{\partial t} A$ is the heat flux associated to the release of the *latent* heat of fusion or solidification. L_f is the latent heat of fusion of water and A is the surface area.
- $\dot{Q}_c = h_c(T - T_{air})A$ is the *convective* heat flux exchanged between ice (rime regime) or water (glaze regime) with the surrounding air. h_c is the convective heat transfer coefficient. The convective heat transfer is largely controlled by the geometry and the speed of the body in the airflow, the roughness of the iced surface and the temperature difference between the surface (T) and the local air temperature (T_{air}).
- $\dot{Q}_e = \chi_e[e(T) - e(T_{air})]A$ is the *evaporative* heat flux between water and the surrounding air. χ_e is the evaporation coefficient and $e(T)$ is the evaporation function. The evaporative cooling is a function of the air temperature T_{air} and pressure P at the surface.
- $\dot{Q}_s = \chi_s[s(T) - s(T_{air})]A$ is the *sublimation* heat flux between ice and the surrounding air. χ_s is the sublimation coefficient and $s(T)$ is the sublimation function.
- $\dot{Q}_d = \beta LWCV_\infty C_{Pw}(T_{air} - T_d)A$ takes into account the *cooling* provided *by the incoming droplets* releasing their latent heat upon impact on the surface. This term is different from zero only if the temperature of droplets (T_d) is different from the air static temperature (T_{air}). C_{Pw} is the specific heat of water.
- $\dot{Q}_k = \frac{1}{2}(\beta LWCV_\infty A)V_\infty^2$ is the heat flux associated to the *kinetic* energy of the impinging droplets.
- $\dot{Q}_a = \frac{1}{2}\frac{R_c h_c V_\infty^2}{C_{Pair}} A$ is the heat flux associated to *aerodynamic* heating provided by the friction of the air over the surface. R_c is the adiabatic recovery factor, which takes into account the compressibility of the air and C_{Pair} is the specific heat of air evaluated at constant pressure.

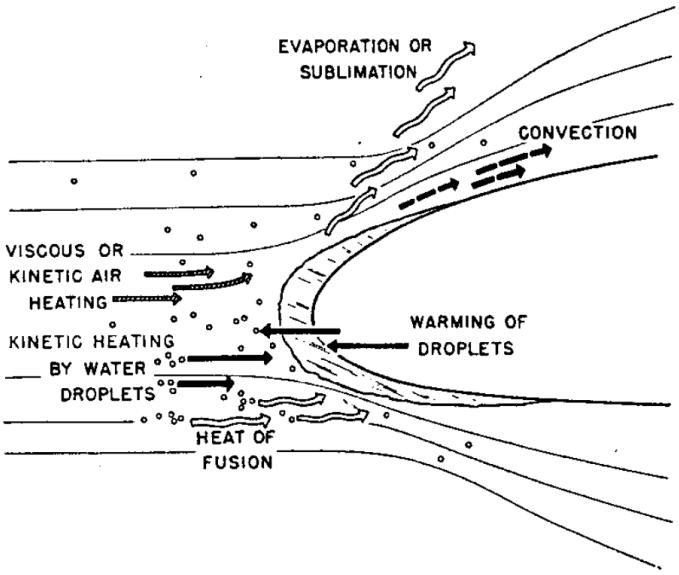

Figure 1.5: Representation of the heat exchange terms involved in the icing process from Ref. [12].

Outside air temperature (T_{air})

The most critical parameter influencing heat transfer and therefore ice accretion is the ambient temperature. It controls the degree of available convective cooling and, hence, the dissipation of latent heat released from impinging droplets. The higher the potential for convective cooling, the greater is the tendency to freeze any impinging droplet. Moreover, as the air temperature is reduced, the probability of encountering large amounts of supercooled water droplets is reduced. Although static temperature is an important parameter and it is relatively easily measured and available to the pilot, it represents only a part of the accretion physical process. In practice, it is the surface temperature of the body which dictates whether ice accretion is possible and the rate at which it will proceed. However, the most relevant parameter is the total temperature, which takes into account also kinetic heating due to high speed. Civil transport aircraft usually cruise at high subsonic Mach numbers, hence avoiding significant risk of icing, but they must be protected for low speed climb and descent through clouds. Military fast jet aircraft, instead, rarely have wing ice protection systems, since they have the option to accelerate to an ice-free airspeed.

Surface pressure (P)

The surface pressure of the body affects the degree of evaporative cooling $\dot{Q}_e$. As a matter of fact, $\dot{Q}_e$ is a function of the vapour pressure of water, which is itself a function of the temperature and the pressure at the surface. On low-pressure regions, such as the upper surface of an airfoil or the suction side of a rotor, evaporative

cooling is enhanced and combined with the effects of adiabatic expansion it can lead to the formation of beak-ice accretions.

1.1.2 Ice accretion types

Depending on the external environmental conditions, the physics of the ice formation process may lead to different kinds of ice accretions characterised by different properties and behaviours. It is possible to discern between two main different accretion mechanisms which are relevant to aerospace applications, commonly identified as *rime ice* and *glaze ice*. A mathematical model aimed at predicting ice accretion should enforce two different accretion laws, one for the rime and another one for the glaze regime, and clearly establish the ranges in which the two laws hold so as to identify a reliable criterion to switch between them.

Rime ice

Rime ice tends to form at combinations of low ambient temperatures (below 263 K), low speeds, low value of cloud water content and small droplets. It is the result of droplets freezing immediately and completely at impact against the wing surface and it forms a white opaque accretion which is usually relatively streamlined, with smooth shapes accreting on the leading edge of the wings (Fig. 1.6). The almost instantaneous freezing process causes the collected iced water to trap inside some bubbles of air, giving the rime ice its typical opaque aspect, low density (880 kg/m^3) and fragility, which makes it easier to be removed by de-icing systems. Rime ice is generally very rough and porous due to the air bubbles, with a surface roughness which is much greater than that of the wing or other components on which ice accretes.

Figure 1.6: Example of rime ice accretion from Ref. [13].

Glaze ice

Glaze ice forms at combinations of "warm" temperatures (close to the freezing temperature of water, 273 K), high speeds and in clouds with high values of LWC. In these conditions the freezing process is not instantaneous and not all the impinging water freezes upon impact. A peculiar feature of glaze ice formations is the thin liquid layer lying on top of the previously accreted ice layer. This thin film of unfrozen water is driven back by the wall shear stresses before it completely freezes, leading to the formation of run-back ice. This localised thickening of the ice profile may produce what appears to be horns in the vicinity of the leading edge that can protrude widely towards the direction of motion (Fig. 1.7). Glaze ice is characterised by a translucent appearance and it is denser (920 kg/m^3) and harder than rime ice, so it is more difficult to be broken by de-icing systems.

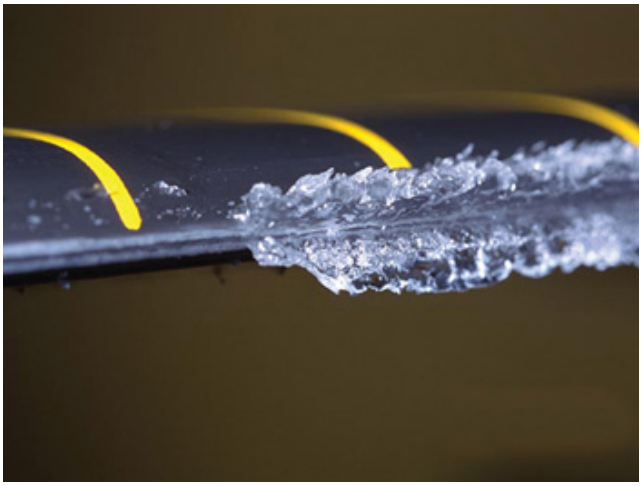

Figure 1.7: Example of glaze ice accretion from Ref. [14].

Mixed ice

Mixed ice is the transitional state between rime and glaze ice. It forms at temperature between 258 K and 265 K and has intermediate characteristics between the previously described ice types.

1.2 Ice protection systems

Airfoils and other bodies can be protected against icing in two basic ways. Anti-icing protection systems entirely prevent ice from forming, while de-icing systems allow ice to form to a tolerable thickness and periodically remove it.

Anti-icing systems

Anti-icing protection systems avoid ice accretion by chemical or thermal means. In the first case, the aircraft surface is covered with chemical sprays or foams before take off. These substances have the function of lowering the freezing point of water or creating a layer on which ice slips away. The heating systems instead are activated during aircraft flight. The leading edge of the wing can be heated by hot air bleeding out of the jet engine or by an electro-thermal system consisting of a resistive circuit buried in the airframe structure to generate heat when a current is applied. Note that water resulting from ice melting would flow back on the surface and might re-freeze behind the protected area, originating the so called run-back ice. To avoid this occurrence, it is recommended to design fully evaporative anti-icing systems.

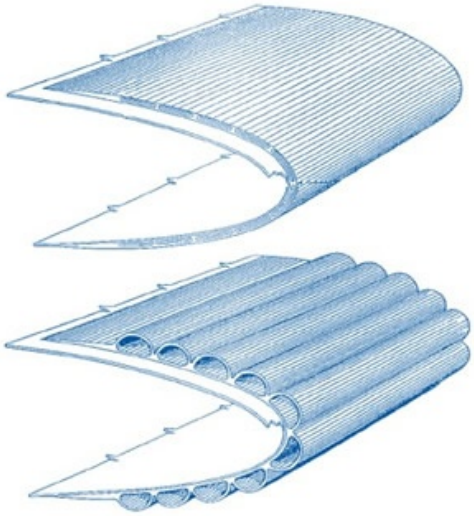

Figure 1.8: Inflatable pneumatic boot de-icing system, Ref. [15].

De-icing systems

De-icing protection systems are used to remove the ice already accreted on the aircraft surface. Ice can be melted with a cyclic application of heat or broken by an inflatable pneumatic boot (Fig. 1.8) typically placed on the leading edge of the wing. The boot is usually made of layers of rubber, with one or more air chambers between the layers, which are rapidly inflated and deflated. The change of shape causes the adhesive forces between the ice and the rubber to break and ice is carried away by the relative wind flowing past the aircraft.

In this context stems the development of ice protection systems based on super hydrophobic surfaces, which may reduce the power needed to avoid ice accretion both in anti-icing and de-icing systems. Indeed, as it will be discussed in Ch. 5, super hydrophobic surfaces both reduce water deposition and adhesive forces between the ice and the surface.

1.3 Scope and structure of the thesis

Ice protection systems improve safety standards and reduce operational costs and environmental impact, but their design requires a deep knowledge of the icing phenomenon and an accurate prediction of the related performance degradation. From an engineering point of view arises the challenge of an improvement of ice accretion prediction tools so as to guarantee safety with the least possible economic cost and resources employed.

For a reliable prediction of ice shapes a proper numerical tool is necessary and the present work stems from this need. In this context, the framework for ice accretion simulations used at the Politecnico di Milano is updated merging different tools already developed for the computation of the flow field, particle trajectories and ice accretion. In particular, the focus of this work is to improve the particle tracking code to describe in a more detailed way the droplet-wall interaction. The accurate modelling of this phenomenon results to be of particular importance in case of Supercooled Large Droplets (SLD), which are cloud droplets with a diameter greater than 40 μm. These droplets, due to their bigger dimension, have a greater tendency to deform under the influence of aerodynamic shear forces and they are more likely to splash or rebound upon impact on the surface. In fact, when a droplet impinges on a surface different types of interaction could occur: the droplet may stick, rebound or splash, depending on different physical variables, such as its diameter, impact velocity, surface tension and surface roughness. The latter is exploited in the design of anti-icing systems based on super hydrophobic surfaces, whose surface finish rebounds the droplets away from the wall, preventing them from sticking on the surface.

The present work is organised as follows. In Ch. 1 the physics of ice accretion was introduced and the most important parameters governing the icing problem were listed. The different types of ice that can occur depending on these variables and the main methods for ice protection in aeronautical applications were described. Ch. 2 deals with the description of the ice accretion framework used in this work. Its modular structure is presented and its components are analysed in detail. The particle tracking code is considered in Ch. 3. The results obtained for the collection efficiency are compared with reference solutions, experimental data and solutions computed with different numerical algorithms. In Ch. 4 the study of droplet-wall interaction models is carried out. Different models are implemented in the particle tracking code and then tested. Results are once again compared with experimental data to assess their accuracy. Wall interaction models are then employed in Ch. 5 to analyse the behaviour of super hydrophobic surfaces exploited as anti-icing protection systems. Eventually, Ch. 6 provides conclusions and recommendations for future developments.

Chapter 2

Ice accretion computation with PoliMIce

The certification of aircraft operating in icing conditions and the design of anti- and de-icing systems requires the knowledge of the impingement limits and ice thickness. This analysis can be performed in two different ways: experimental tests and numerical simulations. In the past, the certification of aircraft for flight in icing conditions relied totally on flight tests and experiments conducted in icing wind tunnels, which are both very expensive. To reduce this economic burden, in very recent years the computational power has allowed basing the design on numerical analyses, with flight tests performed as a final verification.

The traditional approach to aircraft-icing analyses begins with the computation of the trajectories of droplets to determine where and at what rate cloud water droplets impact on the surface under analysis. The portion of the freestream water content which impinges on the structure can thus be evaluated. Once the water collection efficiency distribution is known, the analysis proceeds to determine the location and the rate at which impinging water freezes. From the solution of the Stefan problem for ice accretion, the ice profile is obtained and eventually its effect on the aircraft performances can be analysed.

To carry out this computational analysis it is necessary to use proper tools. Hence, different ice accretion simulation frameworks have been developed in the last thirty years:

- *LEWICE* [16]: *NASA LEWis ICE accretion prediction code* developed by the Icing Branch at NASA Glenn Research Center.
- *CANICE* [17]: code developed at the *École Polytechnique de Montréal*.
- *ONERA* [18]: ice accretion software developed in France by the *Office National d'Études et de Recherches Aérospatiales*.

- *TRAJICE* [19]: code developed in the United Kingdom by DERA (*Defence Evaluation and Research Agency*).
- *FENSAP-ICE* [20]: initially developed by the McGill University of Montreal and later included in the ANSYS suite.
- *MULTICE* [21]: a code for the evaluation of ice accretion on multi-element airfoils developed by CIRA (*Centro Italiano di Ricerca Aerospaziale*).
- *PoliMIce* [22]: *Politecnico di Milano Ice accretion software.*

PoliMIce is a modelling framework developed to perform two and three dimensional simulations of ice accretion over solid bodies in a wet air flow. In this chapter its modular structure is briefly described and afterwards its components are analysed in detail.

2.1 PoliMIce modular structure

Ice accretion is a time dependent problem: as ice starts to form, the shape of the surface changes and therefore the aerodynamic flow field around the body is modified. As a consequence, the trajectories of droplets are altered and impingement points displaced, thereby modifying the ice accretion rate. In this process two different time scales can be identified. The former is the aerodynamic time scale during which variations in the flow field and aerodynamic performances are attained due to the body shape modification. The latter is the ice accretion time scale defined as the characteristic time resulting in significant ice accretion over the surface. Therefore the ice accretion problem is solved using the iterative process illustrated in Fig. 2.1 and here summarised:

1. *Aerodynamic flow field computation*: the aerodynamic flow field around the body is computed by a CFD solver.
2. *Particle Tracking*: the trajectories of water droplets are computed using a Lagrangian approach. Given the impact points, it is possible to calculate the water mass distribution over the surface and condense this information in the collection efficiency parameter.
3. *Interface*: the output of the CFD simulation is rearranged in the proper format adopted by the icing code. Ice accretion parameters are also calculated.
4. *Ice Accretion*: the ice accretion for the considered time step is performed by the PoliMIce software and the new body geometry is obtained.
5. *Mesh update*: the new mesh is created to fit the new iced geometry. This new mesh is used as the baseline grid for a new iteration starting from point 1.

This procedure is repeated until the total exposure time is reached.

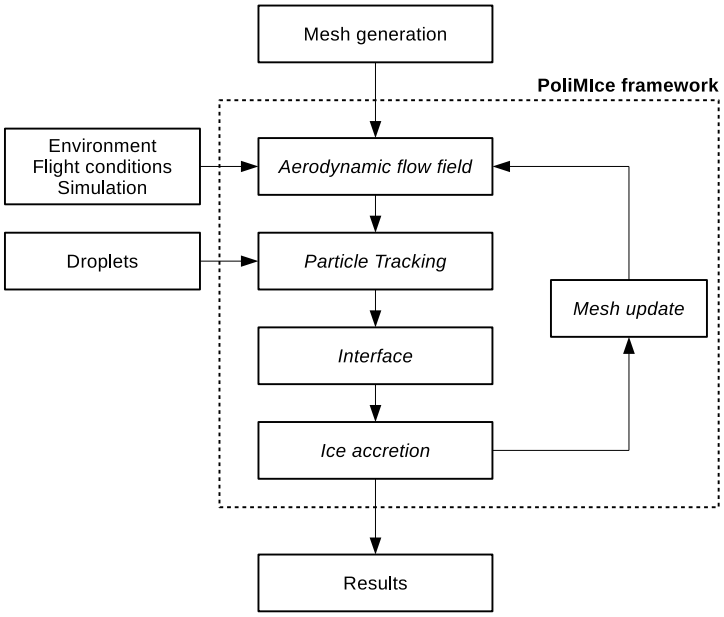

Figure 2.1: Block diagram illustrating PoliMIce modular structure.

The PoliMIce framework is thought to be highly modular, that is to say that the previously mentioned steps (1, 2, 3, 5) can be performed with the user's preferred tool. This is always true, provided that each module receives as input the results given by the previous module and returns as output the data needed by the following module. All the modules used in this work are written in C++. A bash script is used to couple the different modules of the framework and, if necessary, the corresponding interfaces.

2.2 Flow field computation and particle tracking

The first stage in any icing analysis is to determine where and at what rate the cloud water droplets are deposited on the surface of the body under investigation. This characteristic is usually referred to as the water collection efficiency distribution, which by definition needs the trajectories of the droplets to be computed previously. Trajectories in turn can be calculated only if the flow field solution is known.

In this work the open source code SU2 (Palacios et al. [23, 24]) is used to compute the aerodynamic solution around airfoils, given the computational grid and the proper boundary conditions. The velocity field in the whole domain is used by the particle tracking module to track the position of cloud droplets over time, while the flow field solution on the surface of the airfoil is required in the accretion analysis.

Once the velocity is known in each cell, trajectories can be computed. A Lagrangian Particle Tracking code, named PoliDrop, is used to track droplets and determine

their impact positions, which are necessary for the computation of the collection efficiency. The PoliDrop software requires as input:

- the computational grid in SU2 format
- the SU2 flow field solution
- the SU2 configuration file
- the PoliDrop configuration file which contains the simulation parameters, the properties of droplets and their initial positions and velocities.

The outputs are the positions of the droplets at each time step t in the *cloud_t.vtk* files and the collection efficiencies on the selected boundaries *beta_label.vtk*, where label stands for the name of the boundary. The algorithm employed by PoliDrop to track particles trajectories will be analysed in Ch. 3.

2.3 Interface

To run an ice accretion simulation it is necessary to interface the CFD and particle tracking codes with the PoliMIce code. In past works the flow field and trajectories of droplets were computed using the open-source CFD solver OpenFOAM. Results were then post-processed using an interface between OpenFOAM and the ice accretion module and given as input to PoliMIce.

In this work instead the aerodynamic flow field is solved using a different open-source software, SU2, and the trajectories of droplets are calculated with PoliDrop, code developed ad hoc at the Department of Aerospace Science and Technology of the Politecnico di Milano. Obtained results must then be post-processed to generate the necessary input for the ice accretion computation, which are the surface mesh and the ice accretion parameters. It is thus necessary to load the mesh, the flow field solution, the aerodynamic data and the collection efficiency and rewrite them in the correct format to allow reading by PoliMIce. At each time step t, PoliMIce needs the following files as input [25]:

- *WALLS.txt*. It is the boundary file and it is created reading the input file *input_boundaries.txt*. It contains the number of boundaries and, for each boundary, its label, boundary type and the ID of its first and last face.
- *t_NODES.txt*. It is the file containing the coordinates of boundary nodes and it is created reading the complete domain mesh. It contains the mesh dimension and the number of boundary nodes. Each line corresponds to a node and contains the node coordinates.
- *t_kinship.txt*. It is the file which allows mapping from the ID of nodes in the global mesh to the ID of nodes in the surface mesh. The first column lists the

ID of nodes of the surface mesh in increasing order. For each node the second column provides the ID of the node in the global mesh.

- *t_CONSTRAIN.txt*. It is the file specifying the constraints on each boundary node. For each node there is a sequence of values corresponding to the constraints in displacement applied to each node. The value 0 means unconstrained displacement, the value 1 constrained displacement and the value 2 means displacement to be assigned by PoliMIce after the ice accretion computation.
- *t_CONNECTIVITY.txt*. It is the connectivity map of boundary faces. The file contains the number of boundary faces. Each line represents a face and contains the number of nodes belonging to the considered face and their ID. Nodes are ordered using the right hand rule.
- *t_beta.txt*. It is the collection efficiency file and it is written using values read from the *beta_label.vtk* files created by PoliDrop. For each boundary it contains the number of faces and the value of β for each face. Note that the particle tracking code used in this work returns directly the collection efficiency for each boundary.
- *t_AeroDynamicData.txt*. It is the flow field solution file created reading the *flow.vtk* file. The *t_AeroDynamicData.txt* file must contain the solution on faces while the SU2 solution is given on nodes. It has thus been necessary to interpolate the solution on boundary faces: the solution on the face is computed as the weighted mean of the solutions on nodes, where the weights are chosen to be the inverse of the distance of the nodes from the face centroid. Each line of the file corresponds to a boundary face and contains:
  - collection efficiency β
  - heat transfer coefficient, assumed to be constant and equal to 1000 W/m^2K
  - recovery factor, assumed to be constant and equal to 0.7
  - wall shear stresses (or flow field velocity at the wall in Euler simulations), used to compute the direction of the moving liquid film
  - pressure P
  - face wallflag ($0 \rightarrow$ no ice accretion, $1 \rightarrow$ ice accretion).

In this work, a new interface between SU2 and the ice accretion module PoliMIce, named *SU2_2PoliMIce*, was implemented. The interface takes as input the mesh and the CFD solution and returns the previously listed files (Fig. 2.2), so as not to modify the iterative process of the PoliMIce solver. The modular structure of the program is preserved so that it is always possible to select the preferred CFD and particle tracking solver, modifying only the interface.

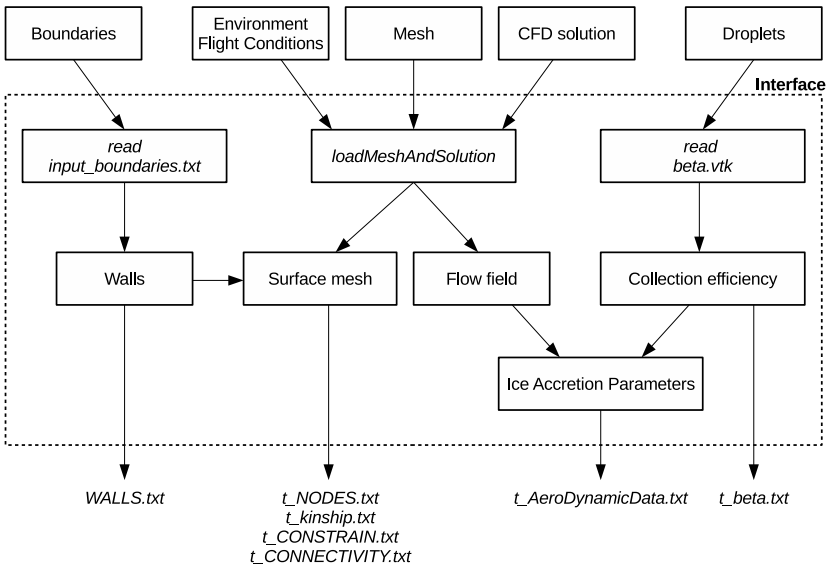

Figure 2.2: Block diagram of the *SU2_2PoliMIce* interface.

2.4 Ice accretion computation

The computational domain for the ice accretion solver is the surface mesh, defined as the set of all boundary faces of the global mesh. The surface domain is divided into elementary cells, which for convenience are coincident with the elements of the surface CFD mesh. Over each cell a piecewise constant representation of the solution is assumed and a one-dimensional ice accretion problem is solved in the direction normal to the surface. For each cell the presence of water both in the liquid and in the solid phase is assumed. The two phases are separated by an interface of infinitesimal thickness, at which the phase change occurs.

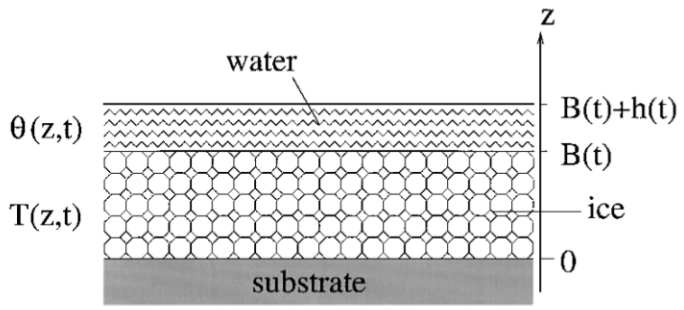

Figure 2.3: Reference system for the one-dimensional ice accretion problem from Ref. [26].

The reference framework considered is shown in Fig. 2.3: the z coordinate is measured along the local normal to the surface and provides the distance of a point from the surface. The unknowns of the multi-phase problem for ice accretion are the thickness B and temperature T of the ice layer and the thickness h and temperature Θ of the water layer. The thickness of the two layers is a function of time t, while the temperature is in general a function of time t and distance from the surface z. For each surface element, the solution of PoliMIce contains:

- h, liquid water film thickness $[m]$
- B, ice layer thickness $[m]$
- B_g, limiting thickness for rime ice regime $[m]$
- T_{surf}, temperature over the ice surface (rime) or water surface (glaze) $[K]$
- T_{wall}, wall temperature $[K]$
- $\dot{Q}_w$, heat flux at the wall $[J/m^2s]$
- R_a, ice surface roughness $[\mu m]$
- $\dot{m}_{in}$, mass flux related to incoming water from neighbouring cells $[Kg/s]$
- $\dot{m}_{out}$, mass flux related to outgoing water to neighbouring cells $[Kg/s]$

These parameters can be computed solving a one-dimensional ice accretion problem over each cell using different models. In PoliMIce software this model is based on the Myers model [26] which is a reduction of the Stefan problem [27].

2.4.1 Stefan problem

The first mathematical formulation of a two-phase problem was given by Stefan in 1889 [27] and it is considered as the prototype of all physical problems concerning phase changes. It consists of a set of four partial differential equations referred to the control volume in Fig. 2.3. For the liquid water-ice two-phase case:

$$\begin{cases} \dot{m}_{fr} + \dot{m}_h = \dot{m}_d + \dot{m}_{in} - \dot{m}_{out} \\ \dfrac{\partial \Theta}{\partial t} = \dfrac{\lambda_w}{\rho_w C_{Pw}} \dfrac{\partial^2 \Theta}{\partial z^2} \\ \dfrac{\partial T}{\partial t} = \dfrac{\lambda_i}{\rho_i C_{Pi}} \dfrac{\partial^2 T}{\partial z^2} \\ \dot{Q}_{change} = \dot{Q}_{up} + \dot{Q}_{down} \end{cases} \tag{2.1}$$

where:

- The first equation is the continuity equation which enforces mass conservation: the mass rate related to the phase change $\dot{m}_{fr}$ (freezing water) and water film thickness change $\dot{m}_h$ equals the net mass flux entering the cell. The net mass

flux is given by the mass flux related to impinging droplets $\dot{m}_d = \beta LWCV_\infty A$, the mass flux related to incoming water from neighbouring cells $\dot{m}_{in}$ and the mass flux related to outgoing water to neighbouring cells $\dot{m}_{out}$.

- The second and third equations are the one dimensional heat diffusion equations in the liquid and solid phase respectively, where λ is the thermal conductivity, ρ the density and C_P is the specific heat capacity at constant pressure. Note that subscripts w and i refers to liquid water ad ice respectively.
- The fourth equation is the Stefan condition enforcing the heat conservation law across the interface: the latent heat due to the phase change $\dot{Q}_{change} = \rho_i L_f \frac{\partial B}{\partial t}$ equals the net flux of heat from the upper and lower layers, where $\dot{Q}_{up} = \lambda_i \frac{\partial T}{\partial z}\big|_B$ and $\dot{Q}_{down} = -\lambda_w \frac{\partial \Theta}{\partial z}\big|_B$.

All the ice accretion models analysed hereafter are based on the Stefan set of equations (Eq. 2.1), with additional hypotheses on the physics of the problem and a different representation of heat fluxes.

2.4.2 Myers model

In 2001 Myers presented a new model to obtain a more accurate transition from rime to glaze regime and to improve the prediction of the heat transfer at the aircraft surface, with respect to the Messinger model. The model proposed by Messinger in 1953 [12] was based on a local energy balance, enforcing that the heat exchanged by the surface with the air equals latent heat related to phase change. In practice, only the Stefan condition was considered. Conversely, as illustrated in Ref. [26], the Myers model is obtained from the complete Stefan problem with the following assumptions:

- Ice and water properties do not depend on temperature.
- The wall is at constant temperature T_{wall}, assumed to be equal to the freestream air temperature T_∞.
- The phase change occurs at a specified temperature, when the ice surface reaches the water freezing temperature $T_{freezing}$.
- The liquid film layer thickness h is assumed to be 100 μm height and constant in time.
- Water temperature Θ is considered to be constant in the water layer thickness.
- Droplets are in thermal equilibrium with the surrounding air and therefore their temperature T_d is equal to the air temperature T_∞.
- The time scale governing the heat diffusion problem is larger than the ice accretion time scale.

The resulting equations are the following:

$$\begin{cases} \rho_i \dfrac{\partial B}{\partial t} + \rho_w \dfrac{\partial h}{\partial t} = \beta LWCV_\infty \\ \dfrac{\partial \Theta}{\partial t} = \dfrac{\lambda_w}{\rho_w C_{Pw}} \dfrac{\partial^2 \Theta}{\partial z^2} \\ \dfrac{\partial T}{\partial t} = \dfrac{\lambda_i}{\rho_i C_{Pi}} \dfrac{\partial^2 T}{\partial z^2} \\ \rho_i L_f \dfrac{\partial B}{\partial t} = -\lambda_w \dfrac{\partial \Theta}{\partial z}\Big|_B + \lambda_i \dfrac{\partial T}{\partial z}\Big|_B \end{cases} \tag{2.2}$$

It is then necessary to distinguish between rime ice and glaze ice conditions. This is done evaluating the limiting thickness for rime ice regime B_g. This parameter is defined as the maximum ice thickness for which it is possible to satisfy the Stefan condition imposing the water layer thickness and the related accretion rate equal to zero and it is computed as:

$$B_g = \frac{\lambda_i (T_{freezing} - T_{wall}) A}{L_f \beta LWCV_\infty A - (\dot{Q}_c + \dot{Q}_e + \dot{Q}_d - \dot{Q}_k - \dot{Q}_a)} \tag{2.3}$$

Depending on the value of the computed limiting thickness we have different regimes:

$$\begin{cases} B_g < 0 \rightarrow \text{no ice is formed on the surface} \\ \\ B_g > 0 \rightarrow \text{ice accretion} \begin{cases} B < B_g \rightarrow \text{rime ice regime} \\ \\ B > B_g \rightarrow \text{glaze ice regime} \end{cases} \end{cases}$$

and for each one of them different equations have to be used to compute the ice layer thickness.

Rime ice accretion law

In rime ice conditions the collected water freezes almost instantaneously. In this case the accretion scheme is only composed by the ice layer, the body surface and the surrounding air. The liquid water thickness $h(t)$ and its first derivative are null and thus the accretion rate in the rime ice condition can be immediately derived from the mass conservation law. Eq. 2.2(a) becomes:

$$\rho_i \frac{\partial B}{\partial t} = \beta LWCV_\infty \tag{2.4}$$

Integrating the ice accretion rate with the initial condition $B(0) = 0$ the following equation for the rime ice thickness is obtained:

$$B(t) = \frac{\beta LWCV_\infty}{\rho_i} t \tag{2.5}$$

It can be observed that the accretion rate in rime ice conditions is constant in time and consequently the ice thickness $B(t)$ is a linear function of time.

The hypothesis that the time scale governing the heat diffusion problem is much larger than the ice accretion time scale, leads to a great simplification of Eq. 2.2(c) which becomes:

$$\frac{\partial^2 T}{\partial z^2} = 0 \tag{2.6}$$

Integrating twice this equation with the proper boundary condition:

$$-\lambda_i \frac{\partial T}{\partial z}\bigg|_B = \dot{Q}_c + \dot{Q}_d + \dot{Q}_s - \dot{Q}_a - \dot{Q}_k - \dot{Q}_l \tag{2.7}$$

a linear temperature profile in the ice layer is obtained:

$$T(z) = T_{wall} + \frac{\dot{Q}_a + \dot{Q}_k + \dot{Q}_l - \dot{Q}_c - \dot{Q}_d - \dot{Q}_s}{A\left(\lambda_i + \frac{B}{A(T_{wall} - T_\infty)}(\dot{Q}_c + \dot{Q}_d + \dot{Q}_s)\right)} z \tag{2.8}$$

Glaze ice accretion law

In glaze ice conditions the surface of the ice layer is always covered by a thin film of liquid water because the amount of collected water does not freeze immediately. In this case the following boundary conditions are set for the ice layer:

$$\begin{cases} T(0,t) = T_{wall} \\ T(B,t) = T_{freezing} \end{cases} \tag{2.9}$$

and for the liquid water layer:

$$\begin{cases} \Theta(B,t) = T_{freezing} \\ -\lambda_w \dfrac{\partial \Theta}{\partial z}\bigg|_B = \dot{Q}_c + \dot{Q}_d + \dot{Q}_e - \dot{Q}_a - \dot{Q}_k \end{cases} \tag{2.10}$$

Integrating Eq. 2.2(b) and (c) and applying the proper boundary conditions the temperature profiles in the two layers are obtained:

$$T(z) = T_{wall} + \frac{T_{freezing} - T_{wall}}{B} z \tag{2.11}$$

$$\Theta(z) = T_{freezing} + \frac{\dot{Q}_a + \dot{Q}_k - \dot{Q}_c - \dot{Q}_d - \dot{Q}_e}{A\left(\lambda_w + \frac{h}{A(T_{wall} - T_\infty)}(\dot{Q}_c + \dot{Q}_d + \dot{Q}_e)\right)} z \tag{2.12}$$

Substituting the derivatives of the temperature profiles (Eq. 2.11 and Eq. 2.11) in the Stefan condition and neglecting the rate of liquid film accretion, the glaze ice accretion rate is obtained. The ice layer thickness in glaze conditions is computed integrating the ice accretion rate over time.

2.4.3 PoliMIce ice accretion model

The major drawback of the Myers model is that the liquid film is considered only in the computation of the ice accretion rate $\frac{\partial B}{\partial t}$, while it is neglected in the computation of the limiting thickness B_g. Therefore a model of the problem is not provided in case of a rime cell next to a glaze cell from which it receives an incoming mass flow $\dot{m}_{in}$. An improved Myers models is thus introduced [28], which allows mass flow from a glaze cell to an adjacent rime cell, so as to guarantee mass conservation also in this case. The outgoing mass fluxes related to sublimation are also accounted for in the computation of the rime ice thickness:

$$B(t) = \frac{\beta LWCV_\infty A + \dot{m}_{in} - \frac{\dot{Q}_s}{L_s}}{A\rho_i} t \tag{2.13}$$

Another difference introduced is that the linear temperature profile approximation proposed by Myers for the ice layer is replaced by the non linear temperature profile in Eq. 2.14, to better respond to the constant wall temperature assumption. This hypothesis in fact calls for high thermal conductivity and thermal inertia at the wall, leading to an infinite heat flux at the body surface.

$$T(z) = T_{wall} + \frac{T_{freezing} - T_{wall}}{\sqrt{B}} \sqrt{z} \tag{2.14}$$

Moreover, the PoliMIce model departs from the Myers model in that it introduces an unsteady treatment of the heat diffusion problem through the ice layer [28] and it considers the local temperature of the airflow to evaluate the heat exchanged by convection at the water-air interface.

2.5 Mesh update

Once the ice accretion has been computed, it is necessary to update the mesh to account for the ice layer formed over the surface. The mesh generation tool used in this thesis is called *uhMesh*. It is an unstructured-hybrid grids generator developed by Rebay et al. [29, 30] which allows the generation of 2D grids through a simple input file. In the input file the boundary points are listed and control points and mesh refinement are defined. In particular, for the airfoil case the farfield corners are selected and airfoil coordinates are read from the *airfoil_coordinates.dat* file. To this purpose a C++ code was written to read the airfoil coordinates from the *t_NODES.txt* file created by PoliMIce and to write them in the proper format for *uhMesh*. In this way the mesh is updated at each time step, taking into account the new geometry computed by the ice accretion code.

2.6 SU2-PoliMIce framework

All the elements described must be linked together as shown in Fig. 2.4 to perform the ice accretion computation with the iterative process illustrated at the beginning of the chapter. Parallel simulations are performed on the *Megamind* cluster, which is equipped with 204 computational units. The bash file *Run.sh* is written to perform all the computations in sequence and to copy input and output files in the right folders. Starting from the initial time, the described process is repeated in a cyclic way for each considered time step, until the total exposure time is reached.

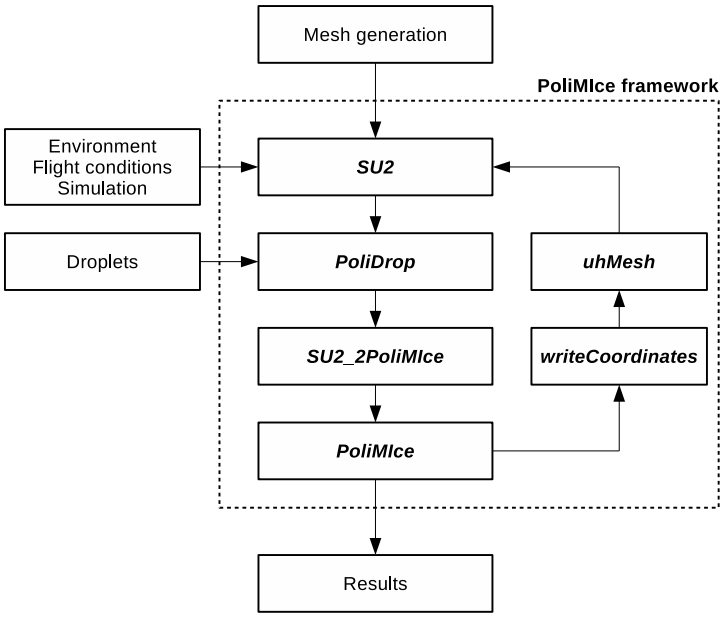

Figure 2.4: Block diagram illustrating the SU2-PoliMIce framework.

2.6.1 Test cases

The new updated framework has been tested on a reference case to evaluate its accuracy with respect to the coupling with OpenFOAM adopted in Ref. [22]. An ice accretion simulation was run on a NACA 0012 airfoil, with the flight and atmospheric conditions illustrated in Tab. 2.1.

	Case 1
Airfoil	NACA 0012
Chord	0.3 m
$\mathbf{V}_\infty$	129 m/s
α	0 deg
$\mathbf{d_p}$	20 μm
$\mathbf{T}_\infty$	260.55 K
$\mathbf{P}_\infty$	90700 Pa
LWC	0.5 g/m^3
$\mathbf{t_{exp}}$	120 s
$\mathbf{\Delta t}$	5 s
Model	Ref. [22]

Table 2.1: Ice accretion parameters for the assessment of the SU2+PoliMIce framework (Case 1).

The total exposure time t_{exp} is 120 s. Ice accretion is performed every second, while the flow field and trajectories of droplets are updated every 5 seconds. Results at different time steps are shown in Fig. 2.5 where the solution is represented every 20 seconds for the sake of graph readability. As expected it is observed that at $\alpha = 0$ deg ice accretion is symmetric on the upper and lower sides of the airfoil. The final ice shape is then compared with experimental data, LEWICE results taken from Ref. [31] and with results obtained with PoliMIce coupled with OpenFOAM from Ref. [25]. Fig. 2.6 shows the comparison of the ice shapes at $t = 120$ s.

From the obtained results it is observed that the new framework shows a good accordance with respect to the coupling with OpenFOAM. As far as experimental data are concerned, the impingement limits are well identified and the value of the ice layer thickness close to the stagnation point is accurate. However, the horns that appears moving away from the stagnation point and the irregularities following these regions are not well represented, nor by the OpenFOAM coupling, nor by the SU2 coupling. These discrepancies with respect to experimental data may be traced back to the complex phenomenology that characterises the air flow and ice accretion in these regions, together with some assumptions made to simplify the numerical solution. For example, the model selected for ice accretion is based on the asymptotic temperature T_∞ for computing heat fluxes. Using the local temperature value T_{local} at each panel location would result in a better representation of the ice shape.

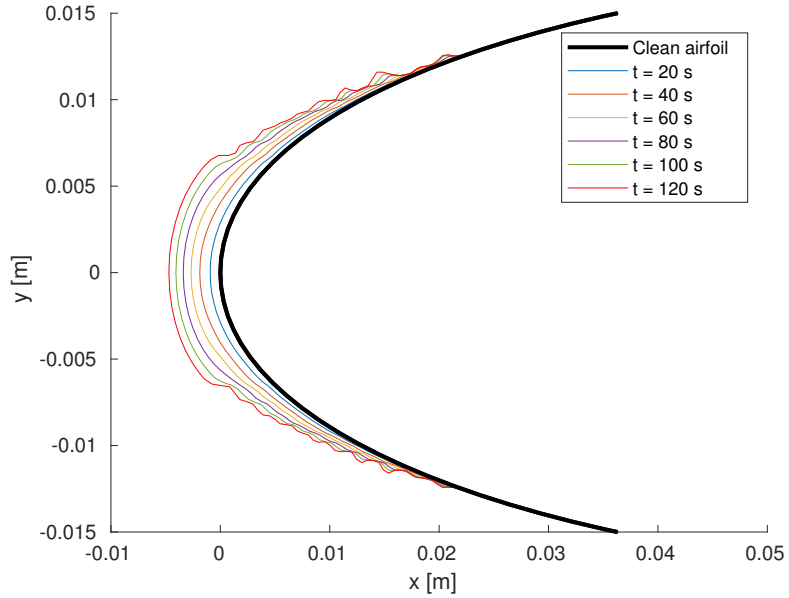

Figure 2.5: Ice accretion over a NACA 0012 airfoil at $\alpha = 0$ deg from 0 to 120 s (Case 1).

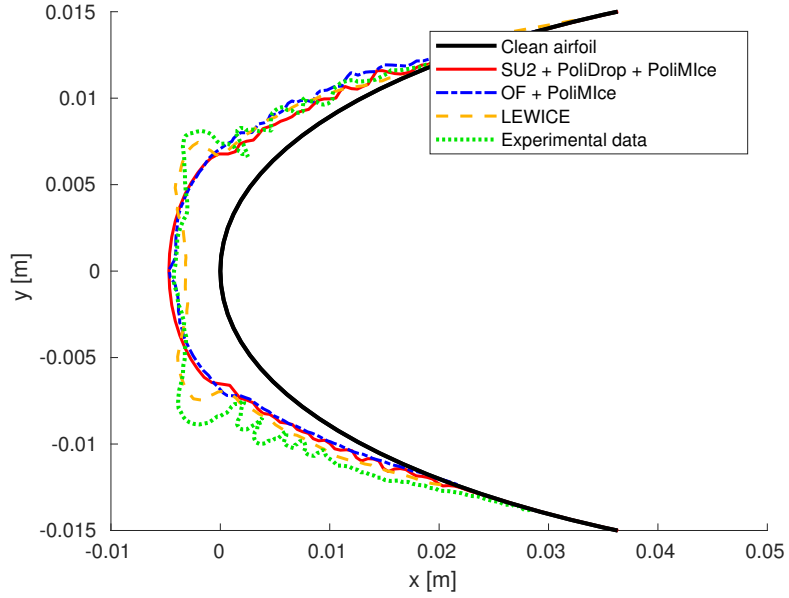

Figure 2.6: Ice accretion over a NACA 0012 airfoil at $\alpha = 0$ deg. Comparison with other codes and experimental data for $t_{exp} = 120$ s (Case 1).

Moreover, the geometry deformation due to the ice layer is performed moving nodes along the panel normal direction, which is not updated as the geometry is deformed, but it is computed only once for the clean airfoil. Although this decision prevents the correct representation of complicated ice shapes, it has been introduced necessarily in order to avoid problems during the advancement of the ice front and the grid generation. Furthermore, as it will be seen in Sec. 3.1.1, the dynamics of the droplet impact on the surface was considerably simplified. Indeed, the hypothesis of completely inelastic collision was made. The impact energy is totally dissipated upon impingement and the droplet remains stuck to the surface. No rebound and splashing phenomena are modelled, neglecting the possibility of small secondary droplets to be formed in the process, which may re-impinge at different surface locations. A more accurate modelling of the droplet-wall interaction is the scope of the present work, while the problem related to the normal direction is not handled here.

For the sake of completeness, other comparisons with experimental data are conducted changing different parameters and results are reported below. Two simulations were run on a NACA 0012 airfoil, with chord $c = 0.533\ m$ and angle of attack $\alpha = 4$ deg, with the flight and atmospheric conditions reported in Tab. 2.2.

	Case 2	**Case 3**
Airfoil	NACA 0012	NACA 0012
Chord	0.533 m	0.533 m
$\mathbf{V}_\infty$	102.8 m/s	67.0 m/s
α	4 deg	4 deg
$\mathbf{d_p}$	20 μm	20 μm
$\mathbf{T}_\infty$	262.04 K	262.04 K
$\mathbf{P}_\infty$	10^5 Pa	10^5 Pa
LWC	0.55 g/m^3	1.0 g/m^3
$\mathbf{t_{exp}}$	420 s	360 s
$\mathbf{\Delta t}$	10 s	10 s
Model	Ref. [22]	Ref. [22]

Table 2.2: Ice accretion parameters for the assessment of the SU2+PoliMIce framework (Cases 2-3).

In both cases ice accretion is performed every second, while the flow field and trajectories of droplets are updated every 10 seconds until the total exposure time t_{exp} is reached. Results for the time evolution of the ice layer are shown in Fig. 2.7 and 2.8, where the computed ice shape is represented every 60 seconds. It is observed that, if the angle of attack is increased from 0 deg to 4 deg, the ice shapes become asymmetric, with wider impingement limits on the lower side and lower impingement limits on the upper side. Moreover, aerodynamic shear stresses drag the liquid film along the airfoil surface, leading to an higher ice layer thickness above the nose of the airfoil. Fig. 2.9 and 2.10 show the comparison of the computed ice shapes with experimental data from Ref. [32]. From these comparisons it can be stated that the

new PoliMIce framework coupled with SU2 and PoliDrop allows to obtain a good agreement with experimental results in both cases.

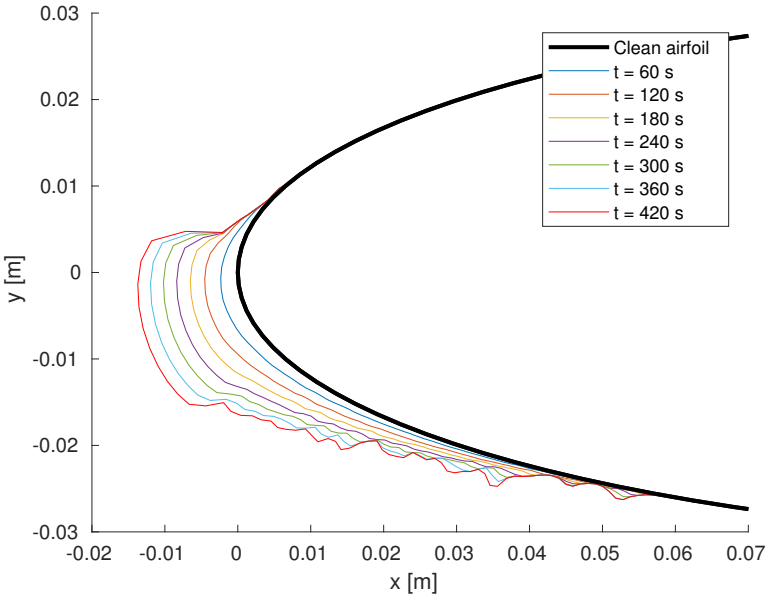

Figure 2.7: Ice accretion over a NACA 0012 airfoil at $\alpha = 4$ deg from 0 to 420 s (Case 2).

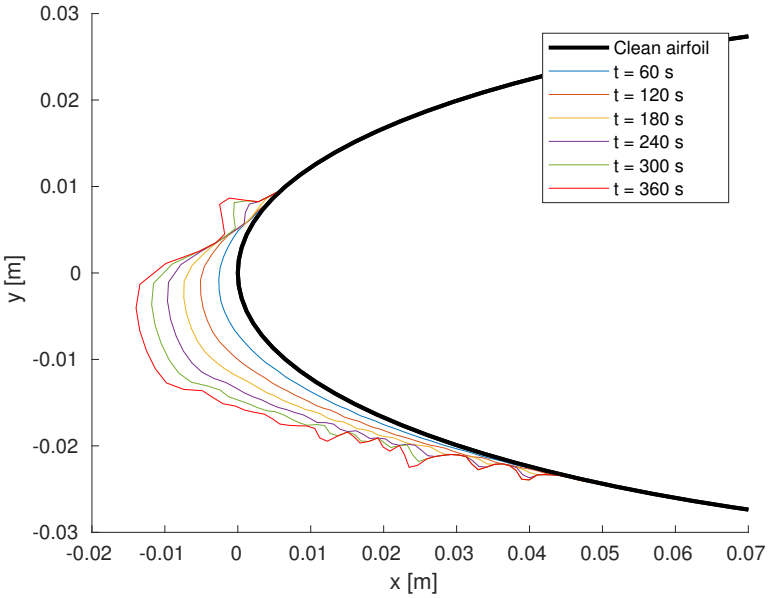

Figure 2.8: Ice accretion over a NACA 0012 airfoil at $\alpha = 4$ deg from 0 to 360 s (Case 3).

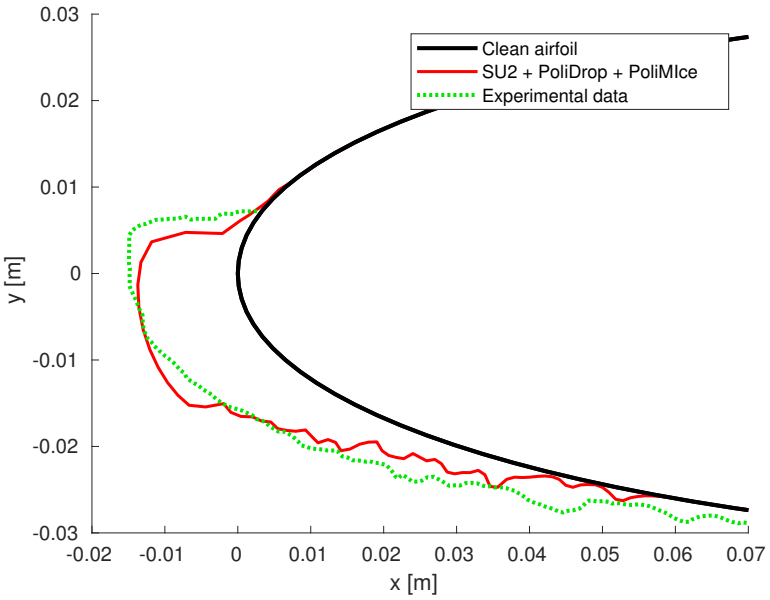

Figure 2.9: Ice accretion over a NACA 0012 airfoil at $\alpha = 4$ deg. Comparison with experimental data for $t_{exp} = 420$ s (Case 2).

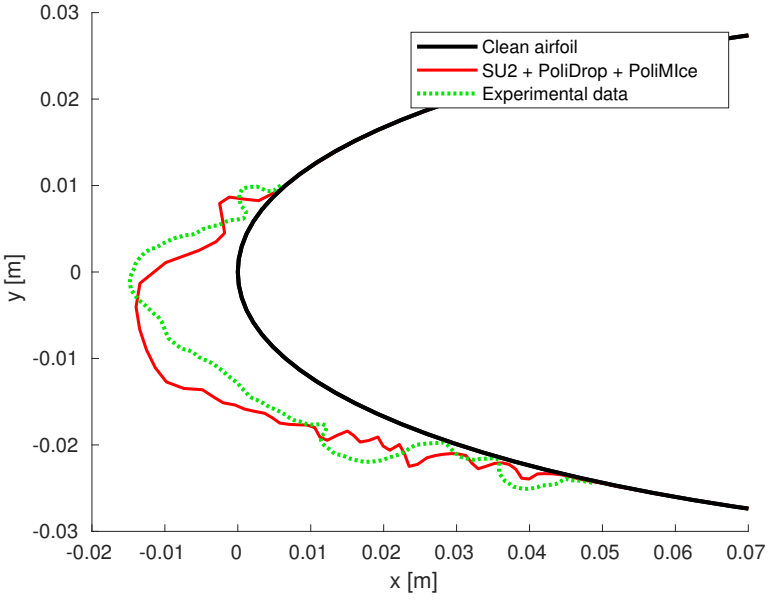

Figure 2.10: Ice accretion over a NACA 0012 airfoil at $\alpha = 4$ deg. Comparison with experimental data for $t_{exp} = 360$ s (Case 3).

Chapter 3

Lagrangian Particle Tracking

To perform an ice accretion analysis it is necessary to accurately know the collection efficiency distribution on the surface of the body under study. This estimation can be obtained with the aid of a particle tracking code. In the present chapter the particle tracking code exploited in this work, PoliDrop, is briefly described and tested through comparison with data available in the open literature, including experimental data and numerical solutions computed with different codes.

3.1 PoliDrop algorithm

The aim of the PoliDrop algorithm is to track cloud particles and to determine their impact positions. From this information the collection efficiency is determined as the mass of water deposited at each surface location in a prescribed time. In order to compute trajectories it is necessary to know the flow field around the body under study. Open-source or commercial CFD tools are normally employed to compute the flow around the component of interest. Methods adopted depend on the application and range from simple panel methods to full Navier-Stokes solvers. For ease of operation, the majority of two-dimensional ice-accretion codes have a flow solver embedded within the trajectory code. This is usually an inviscid incompressible-flow panel method, as in the case of LEWICE [16] and TRAJICE2 [33]. With panel methods, the flow solution is evaluated at each position of the droplet trajectory by summing the contribution to the flow of the calculated circulation from a series of panels that describe the airfoil or body profile. The alternative is a grid-based solution in which the velocity is known at discrete node points of a grid around the body. The velocity at a given point in space is then estimated by interpolation using the surrounding grid nodes. This is what is usually done if a CFD solver is used to compute the flow field, as it is done in this work.

As regards the computation of the trajectories of the particles, there are two main methods. In the last years an Eulerian approach to collection efficiency computation

has been adopted, which is based on a set of partial differential equations representing the continuity and momentum equation of the dispersed droplet phase. With this method no individual particles are tracked, but the volume fraction of water is directly computed at each node of the mesh, together with the flow field variables (see [34] for a more detailed explanation). This approach is particularly useful for complex three-dimensional flow problems and other complex flows such as those through rotor and stator blades at the inlet of a jet engine. For simpler problems, instead, the most frequently adopted method is a traditional Lagrangian formulation in which the trajectory of each individual water droplet is tracked from a specified starting point upstream of the body to the impact point on the surface.

3.1.1 Governing equations

The particle tracking code used hereafter is based on a Lagrangian approach, which integrates in time the equations for trajectories of the droplets. The equations used to track the trajectories of the particles are based on the following primary assumptions [10]:

- Droplets are spherical and do not deform or break up.
- No collision and coalescence of droplets occur.
- Droplets do not bounce or splash upon impact on the surface.
- Turbulence effects may be neglected.
- The only forces acting on the droplet are due to aerodynamic drag and buoyancy. The effect of gravity is not considered here since it is negligible with respect to aerodynamic forces in high-speed flow fields.
- The water droplets concentration is sufficiently small for the droplets to have a negligible effect on the aerodynamic flow and therefore the airflow and water droplets may be treated as independent systems.

Based on these hypotheses, the equations for the trajectories can be deduced from the momentum equation:

$$m_p \frac{d\mathbf{u_p}}{dt} = \mathbf{F_a} \tag{3.1}$$

where the particle mass m_p is computed as the particle volume multiplied by its density and $\mathbf{F_a}$ is the aerodynamic force acting on the particle:

$$m_p = \rho_p \frac{4}{3}\pi \left(\frac{d_p}{2}\right)^3 \tag{3.2}$$

$$\mathbf{F_a} = \frac{1}{2}\rho_f(\mathbf{u_f} - \mathbf{u_p})^2 C_D \pi \left(\frac{d_p}{2}\right)^2 \tag{3.3}$$

By substituting these two definitions in the momentum equation and defining the particle relative Reynolds number as:

$$Re_r = \frac{\rho_f d_p(\mathbf{u_f} - \mathbf{u_p})}{\mu_f} \tag{3.4}$$

the following system for the trajectory of the particle is obtained:

$$\begin{cases} \dfrac{d\mathbf{u_p}}{dt} = \dfrac{3}{4}\dfrac{C_D Re_r \mu_f}{\rho_p d_p^2}(\mathbf{u_f} - \mathbf{u_p}) \\ \dfrac{d\mathbf{x_p}}{dt} = \mathbf{u_p} \end{cases} \tag{3.5}$$

where the first equation gives the acceleration of the particle and the second one its velocity. Note that quantities with the p subscript are referred to the particle while the f subscripts identify the fluid variables.

Integrating this set of equation in time the particle trajectory is obtained. In PoliDrop, System 3.5 is integrated using the explicit forward Euler method. The trajectory computation method is shown in Fig. 3.1 and here briefly described. Starting from the initial parcel position $\mathbf{X}_{P,0}$, the owner cell is found. The owner cell is defined as the cell of the computational grid where the parcel is located. Flow variables in the nodes of the owner cell are interpolated to compute their value in the position of the parcel. Using these computed values, the system is integrated until the trajectory intersects a cell face. With reference to Fig. 3.1(a), the system is integrated until the trajectory of the droplet intersects the face shared by cells 1 and 2. The particle is now considered to be displaced from the previous owner cell 1 to the new neighbour cell 2. System 3.5 is then integrated using the flow velocity in cell 2 until another intersection is found (Fig. 3.1(b)). For each droplet, this process is repeated (Fig. 3.1(c)) until on of the following exit conditions is reached: a) the final integration time is reached, b) the droplet has left the domain, c) the droplet has impinged on a surface. Indeed, when a particle reaches a mesh boundary it is deactivated and it is no more tracked. The collection efficiency β is computed as the ratio between droplet panel density and cloud density, where the droplet panel density is expressed as the ratio of the number of droplets impinged on each panel to the panel area and the cloud density as the ratio of the total number of droplets in the cloud to the volume of the cloud:

$$\beta = \frac{collected\ parcels/panel\ area}{total\ number\ of\ parcels/cloud\ volume} \tag{3.6}$$

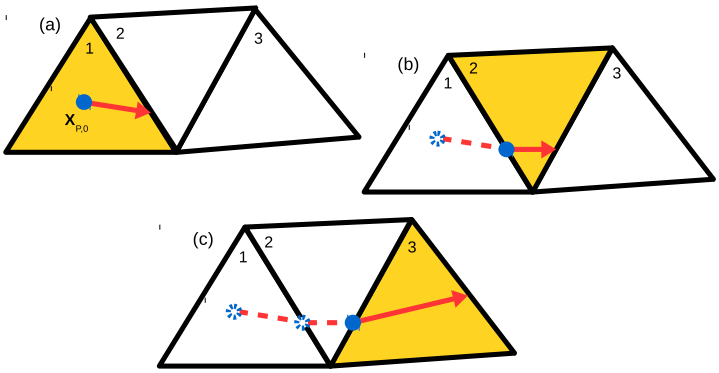

Figure 3.1: Scheme for the computation of the trajectories by the PoliDrop algorithm.

3.1.2 Drag coefficient

In Eq. 3.5 C_D is the drag coefficient of the particle. Since the particles are assumed to be spherical and not to deform, C_D is approximated as the drag coefficient of the sphere, which can be computed as a function of the Reynolds number following different models. The simplest one is the Stokes model, which assumes the C_D to be inversely proportional to Re:

$$C_{D\ \text{Stokes}} = \frac{24}{Re} \tag{3.7}$$

This is a good approximation for low Reynolds numbers, but differs from experimental data when Reynolds increases. Therefore, a correction to Eq. 3.7 has to be introduced. Different high Reynolds corrections can be found in [10] and in [35], for example:

$$C_{D\ \text{Gent}} = \frac{24}{Re}(1 + 0.197Re^{0.63} + 2.6 \cdot 10^{-4} Re^{1.38}) \tag{3.8}$$

$$C_{D\ \text{Schiller Naumann}} = max\left(\frac{24}{Re}(1 + 0.15Re^{0.687}), 0.44\right) \tag{3.9}$$

$$C_{D\ \text{Morris}} = \frac{24}{Re} + 2.6 \cdot \frac{\frac{Re}{5}}{1 + (\frac{Re}{5})^{1.52}} + 0.411 \cdot \frac{(\frac{Re}{263000})^{-7.94}}{1 + (\frac{Re}{263000})^{-8}} + \frac{Re^{0.8}}{461000} \tag{3.10}$$

$$C_{D\ \text{Shankar Subramanian}} = 0.19 - \frac{8 \cdot 10^4}{Re} \tag{3.11}$$

A more accurate representation of the drag coefficient of the sphere is given by the Morris approximation when $Re < 10^6$ and the Shankar Subramanian approximation

when $Re > 10^6$:

$$C_{D\ \mathrm{MSS}} = \begin{cases} C_{D\ \mathrm{Morris}} & Re < 10^6, \\ C_{D\ \mathrm{Shankar\ Subramanian}} + \delta & Re > 10^6 \end{cases} \tag{3.12}$$

where $\delta = 0.0315$ is a correction factor necessary to link the two curves. As it is shown in Fig. 3.2, this model is the one which best fits experimental data.

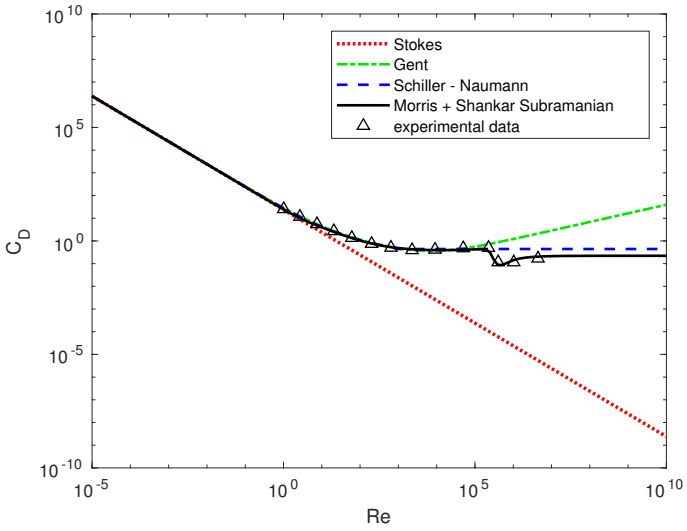

Figure 3.2: Logarithmic scale representation of the drag coefficient of the sphere as a function of the Reynolds number for different analytical models and experimental data from Ref. [35]

3.1.3 Parameters

To perform the computation with PoliDrop some parameters must be set up:

- Simulation parameters: initial and final simulation time, integration time-step.
- Cloud parameters: number of parcels, position and extension of the initial cloud.
- Parcels properties: diameter, density, initial velocity.
- Drag coefficient model.

In particular, it is interesting to analyse the effect of the number of parcels and drag coefficient model on the computed collection efficiency. To this purpose, the flow around a cylinder of unitary radius is considered. The flow is characterised by $M = 0.1$ and $Re = 33$, so as to avoid separation and keep the regime laminar and steady. The numerical solution of the flow field is calculated with SU2, using a hybrid

quadrilateral-triangular computational grid made of 14531 nodes and 23761 elements. Parcels are water droplets with $\rho_p = 1000\ kg/m^3$ and $d_p = 10^{-4}\ m$. In these conditions the collection efficiency is computed for different cloud densities, obtained changing the number of droplets as shown in Tab. 3.1.

Number of droplets	**Cloud density [droplets/m]**
50	100
125	250
250	500
500	1000
1250	2500
2500	5000
5000	10000
50000	100000

Table 3.1: Cloud density as a function of the number of droplets.

As it is shown in Fig. 3.3, if the simulation is performed with a number of droplets less than 500 the collection efficiency shows an irregular trend. At increasing number of droplets, i.e. at increasing cloud density, the collection efficiency profile becomes smoother, until it becomes almost independent from the cloud density for densities greater than 1000 droplets/m.

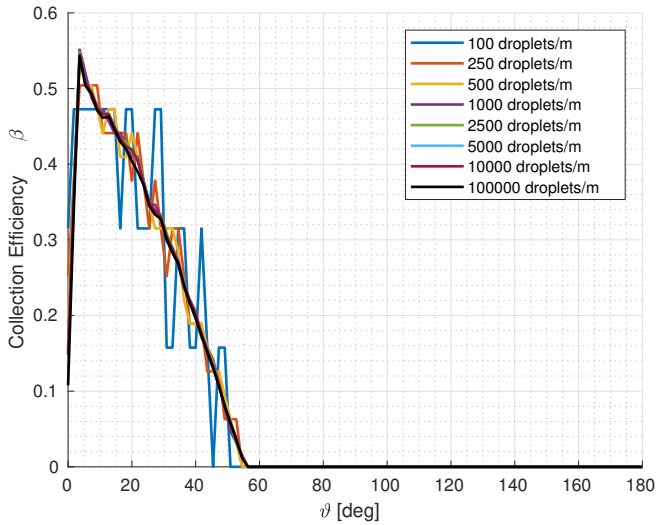

Figure 3.3: Collection efficiency over the surface of a cylinder as a function of the angle ϑ measured counter-clockwise starting from the stagnation point. Different curves are obtained changing the cloud droplet density.

This is due to the fact that the body surface must be discretised in a certain number of panels. If the panels are small and the cloud density low, the number of droplets impacting on each panel is consequently low, giving a collection efficiency highly

dependent from the total number of droplets. Therefore, when running a simulation, the number of parcels must be chosen high enough to obtain a result independent from it. In Fig. 3.3, the black collection efficiency curve computed for a cloud density of 100000 droplets/m represents the β profile at convergence. In the following, simulations are run with a cloud density of 100000 droplets/m.

As commented at the beginning of the current section, another interesting aspect to be considered is the choice of the drag coefficient model to be used in the trajectory equation. In the considered case, parcels are given an initial speed of 51 m/s and the highest computed relative speed between the parcels and the surrounding air is almost 17.5 m/s, which is soon drastically reduced as the parcel is slowed down by the fluid shear forces. The resulting relative Reynolds number is approximately 0.00168. Looking at Fig. 3.2, it is apparent that in the range of Re_r considered in the present simulation, the four C_D models of Eq. 3.7, 3.8, 3.9 and 3.12 give very similar results. This is confirmed if the trajectory of a single droplet is considered and Re_r and C_D are plotted at each time step (Fig. 3.4)

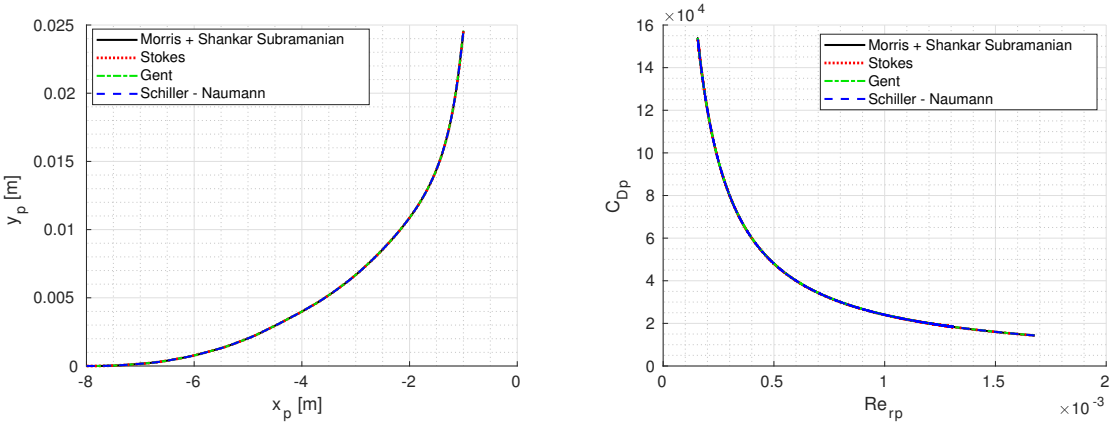

(a) (b)

Figure 3.4: Comparison between C_D models for a single parcel: (a) trajectory of the parcel, (b) C_D-Re curve.

Comparison of results of different simulations run with the same high cloud density (100000 droplets/m) and varying the C_D model revealed that, even if the C_D model has a slight influence on the time of flight, it does not influence the trajectories of droplets. Moreover, Fig. 3.5 shows that, the collection efficiencies obtained perfectly overlap. The conclusion is that at low relative Reynolds numbers the influence of the drag model is irrelevant, thus for all the simulations reported in this work the C_D model is always kept equal to the C_{DMSS} (Eq. 3.12).

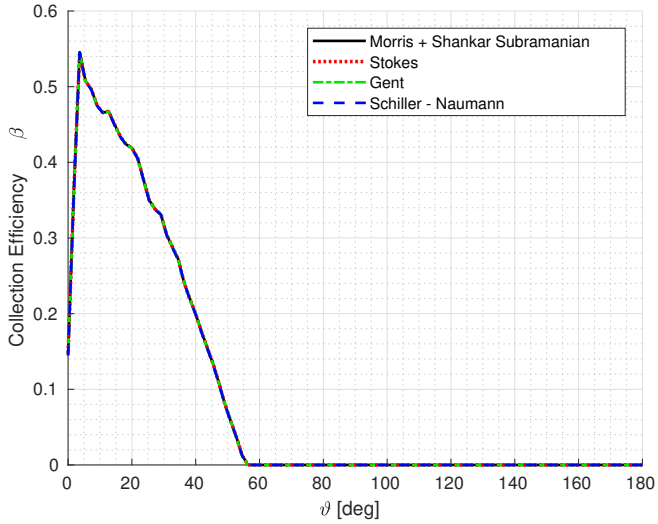

Figure 3.5: Collection efficiency over the surface of a cylinder as a function of the angle ϑ measured counter-clockwise starting from the stagnation point. Different curves are obtained changing the drag coefficient model.

3.2 Reference solutions

Before using PoliDrop as a tool for ice accretion simulations it is necessary to test it through comparisons with experimental data and computations performed with other codes. In particular, comparison in drawn between the collection efficiencies on the body surface computed with different tools.

3.2.1 Exact solution for a cylinder

For the cylinder case, it is possible to compare the solution computed using SU2 and PoliDrop with the exact solution. In fact, for the inviscid incompressible flow around a cylinder the exact solution can be calculated with the method of separation of variables [36]. For a symmetric flow field, the radial and tangential velocity components in polar coordinates are given by Eq. 3.13:

$$\begin{aligned} u_{rad}(r,\vartheta) &= U\left(1-\frac{R^2}{r^2}\right)cos\vartheta \\ u_{tang}(r,\vartheta) &= -U\left(1+\frac{R^2}{r^2}\right)sin\vartheta \end{aligned} \tag{3.13}$$

where U is the asymptotic speed value, R is the cylinder radius, r is the distance from the centre of the cylinder and ϑ is the angular position measured starting from the forward stagnation point.

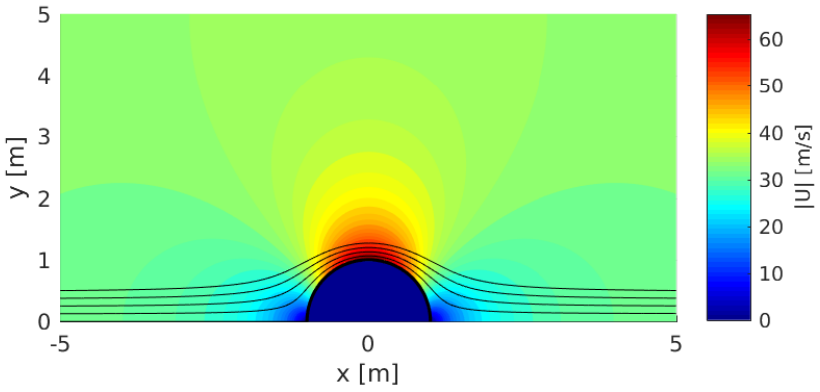

Figure 3.6: Velocity module in m/s and streamlines for the symmetric inviscid incompressible flow field around a cylinder.

Given the initial position of particles, it is possible to integrate Eq. 3.5 with a Runge-Kutta method to compute trajectories. In particular, the *ode45* MATLAB function is used for time integration. Note that, as the exact flow field solution is known, at each time step of the integration the exact flow velocity at the parcel location is evaluated from Eq. 3.13. As for PoliDrop simulations, also in this case it is necessary to discretise the body surface in order to compute the collection efficiency, but a smooth trend can be obtained if a high number of panels associated with a high number of droplets is used. The results obtained from the numerical integration of Eq. 3.13 can be compared with those obtained with PoliDrop applied to the Euler flow field solution computed with SU2. Several computations are performed on different unstructured meshes so as to verify that results are independent from the grid resolution.

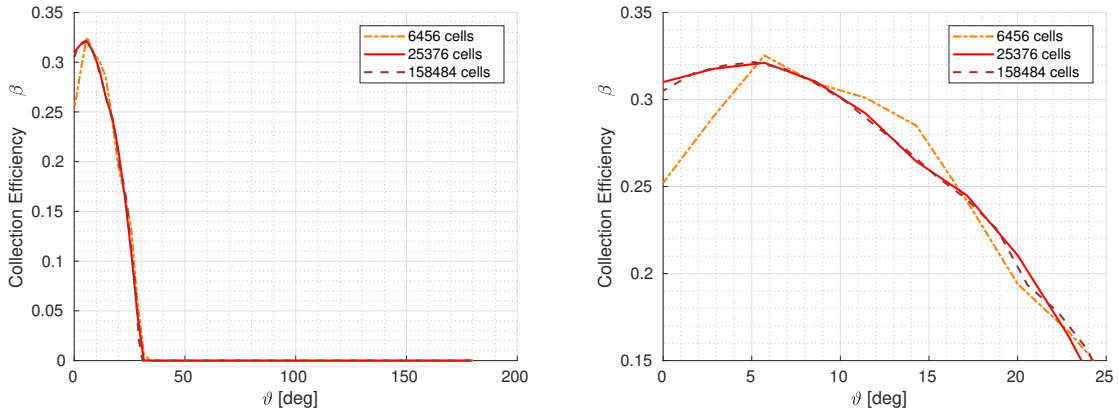

(a) (b)

Figure 3.7: Collection efficiencies varying the mesh density for particles with $d_p = 10^{-4}$. Picture (b) is obtained as a zoom of picture (a) in proximity of the collection efficiency peak.

As it is shown in Fig. 3.7 for parcels with $d_p = 10^{-4}$ the collection efficiencies obtained with the 25376-cell mesh and with the 158484-cell mesh are nearly superimposed, while the collection efficiency computed on the 6458-cell mesh is considerably different. Therefore, the coarsest mesh is too loose for the computation, while the finest mesh is unnecessarily dense as the result obtained with it is no further improved. The medium density mesh is thus used in all the following comparisons. Using particles with $d_p = 10^{-4}$ m, trajectories obtained with the exact solution and with PoliDrop are nearly superimposed (Fig. 3.8) and consequently a good agreement for the collection efficiency is achieved (Fig. 3.9(c)).

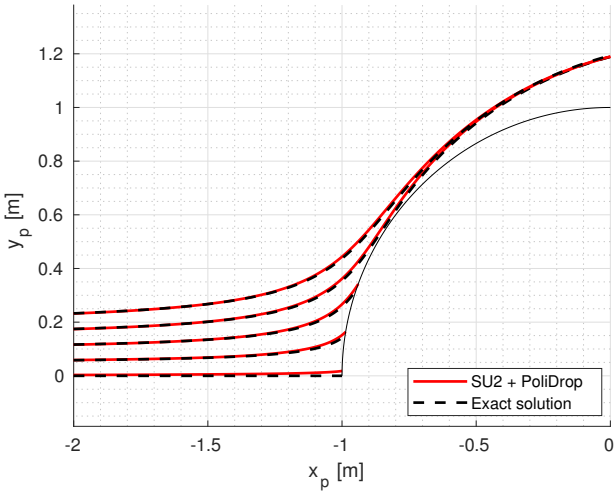

Figure 3.8: Trajectories of water droplets: comparison between exact solution and numerical solution for particles with $d_p = 10^{-4}$ m.

As the diameter of the particles is increased the agreement is improved, while results depart from each other for smaller particles. This is due to the fact that the velocities used in the two cases slightly differ from each other, as the SU2 flow field is computed for each cell and than interpolated at the parcel location, while the flow velocity in the exact solution case is exactly evaluated. Since smaller particles have lower inertia, they are more affected by this error, as it can be seen in Fig. 3.9, where particle dimensions are decreased from $1 \cdot 10^{-3}$ m (a) to $5 \cdot 10^{-5}$ m (d). However, even if the collection efficiencies are no more superimposed in Fig. 3.9 (d), an indicative estimate of impingement limits and β peak value is achieved. Note that even smaller particles do not impact on the cylinder surface. Indeed, since the inviscid flow around the cylinder is characterised by a non-zero velocity at the wall, and since small droplets are prone to following the streamlines due to their reduced inertia, droplets are deviated from the body surface without impacting.

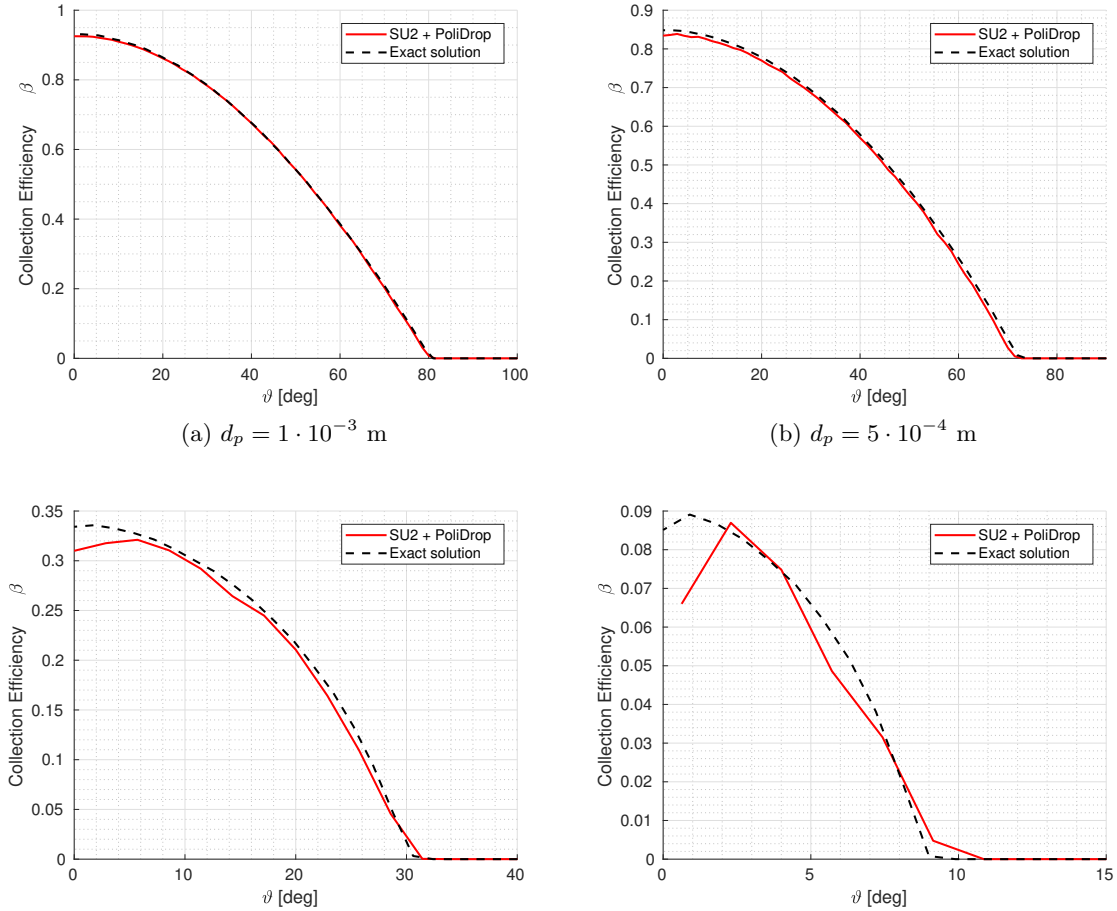

(a) $d_p = 1 \cdot 10^{-3}$ m

(b) $d_p = 5 \cdot 10^{-4}$ m

(c) $d_p = 1 \cdot 10^{-4}$ m

(d) $d_p = 5 \cdot 10^{-5}$ m

Figure 3.9: Collection efficiencies: comparison between exact solution and numerical solution.

3.2.2 Potential flow solution for a NACA0012 airfoil

Contrary to the case of the cylinder, the exact solution of the flow field around an airfoil is unknown. However, it is possible to compute the potential flow solution using the Hess-Smith panel method, based on the following assumptions:

- high Reynolds number,
- incompressible flow,
- two-dimensional flow outside the boundary layer,
- irrotational flow outside the boundary layer.

Under these hypotheses the flow field is computed as the superposition of the asymptotic flow with the flow generated by a distribution of virtual singularities (vortexes and sources) on the surface panels. This test case is presented to provide

a further check of the results obtained with PoliDrop. The airfoil used for this comparison is the symmetric NACA 0012 airfoil. The solution obtained performing the particle tracking on the laminar solution computed with SU2 is compared to the results of a potential flow solver, which also computes particle trajectories and collection efficiency. The method and the code used for these computations are described in detail in Ref. [37]. In particular, the comparison is performed varying the diameter of the droplets and comparing the collection efficiency profiles expressed as functions of the curvilinear abscissa s, measured starting from the leading edge ($s = 0$) and considered positive on the lower surface and negative on the upper surface.

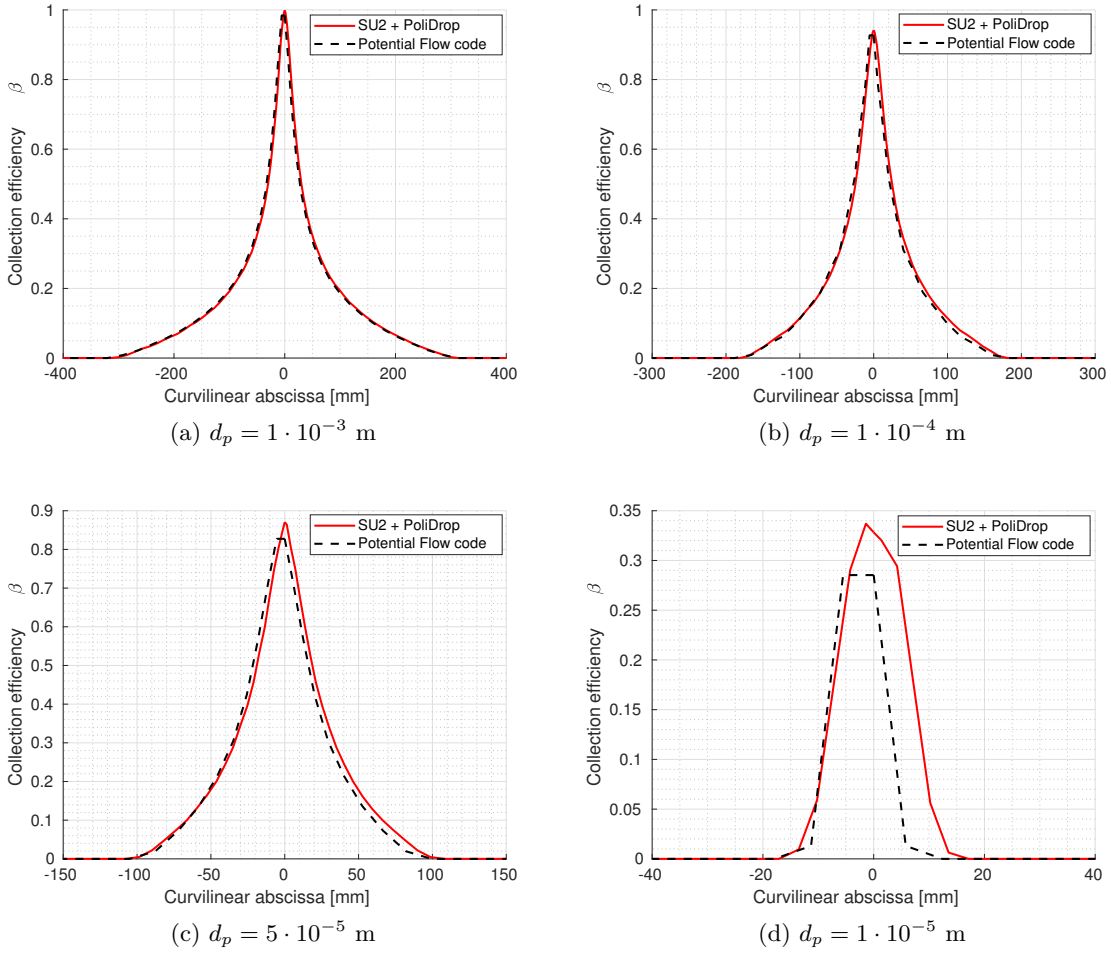

(a) $d_p = 1 \cdot 10^{-3}$ m

(b) $d_p = 1 \cdot 10^{-4}$ m

(c) $d_p = 5 \cdot 10^{-5}$ m

(d) $d_p = 1 \cdot 10^{-5}$ m

Figure 3.10: Collection efficiency as a function of the curvilinear abscissa: comparison between potential flow solution and SU2+PoliDrop solution.

Looking at Fig. 3.10 a good agreement can be noticed both for β and the impingement limits. In particular, the agreement is excellent for big parcels and it decreases with the droplets diameter, since the motion of smaller droplets is more sensitive to the computed value of the flow velocity, which differs in the two cases.

3.3 Comparison with experimental data

Eventually, the results obtained applying the PoliDrop algorithm to the SU2 solution are compared with experimental data and other numerical results obtained with different codes. In particular, experimental data and LEWICE results are taken from Ref. [38], while the other results are obtained running OpenFOAM simulations and SU2 and PoliDrop simulations.

Comparisons are carried out on two different airfoils shown in Fig. 3.11. The NACA 65_2-415 airfoil is a NACA 6-series airfoil characterised by low drag in a limited range of the lift coefficient (drag bucket). It is representative of general aviation wing sections as it is suitable for low speed flight due to low drag and gentle stall characteristics with a relative high thickness ratio to keep structural weight low and to provide sufficient space for fuel. The MS(1)-317 airfoil is representative of modern medium-speed airfoils. It was designed in the mid 1970's by Matthieu Scherrer for general aviation aircraft. In both cases the airfoil chord is 0.9144 m and the asymptotic speed 78.68 m/s.

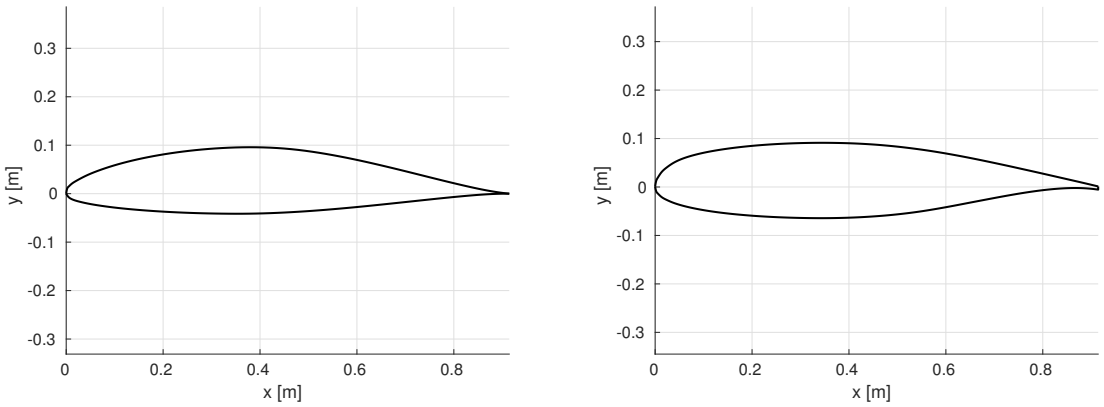

(a) NACA 65_2-415 (b) MS(1)-317

Figure 3.11: Airfoils used for the PoliDrop simulations.

Experimental impingement tests were conducted in the NASA Glenn Icing Research Tunnel (IRT) [38], which is a closed-loop refrigerated wind tunnel suitable for ice accretion simulations. In fact, it operates at or below atmospheric pressure and static temperature can be controlled between 238 K and 278 K. For ice accretion simulations, droplets are generated by a spray system capable of simulating icing clouds with LWC of 0.3-3 g/m^3 and MVD in the range of 14-40 μm. Recently, a small number of large droplets calibrations were performed permitting the generation of icing clouds with MVD in the range 70-270 μm.

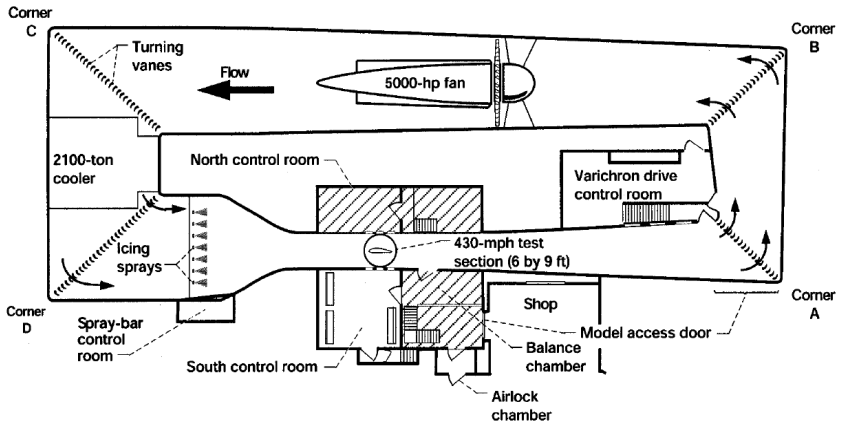

Figure 3.12: Plan view of NASA Glenn Icing Research Tunnel from Ref. [38].

In Ref. [38] the experimental procedure to measure the collection efficiency is described. Impingement tests were conducted in the IRT and a dye-tracer method was used to determine the collection efficiency. In this method, distilled water containing a known concentration of blue dye is injected into the air stream of the IRT in the form of a droplet cloud using the spray system. The test model is covered with thin strips of blotting paper in the areas of interest and it is exposed to the spray cloud. The amount of dye-mass collected by the blotting strip per unit area in a given time interval is measured using reflectance spectroscopy, which quantitatively measures the color and intensity of the light reflected by the body under investigation. The reflected light maintains the same wavelength of the incident light but the same wavelength is absorbed and reflected to different degrees by materials with different properties. Hence, the blotting paper reflects a different amount of light depending on the quantity of dye-tracer it has absorbed. The water impingement characteristics of a test model are obtained from the concentration and location of the dye distribution on the blotting paper.

Numerical simulations are carried out using hybrid grids. Quadrilateral elements are placed in proximity of the surface to properly resolve the boundary layer, while triangular elements are used in the rest of the domain. Meshes are made of 52192 elements and 29228 nodes for the NACA airfoil and of 54703 elements and 30528 nodes for the MS airfoil. The flow field is computed running SU2 CFD simulations based on the Reynolds Averaged Navier-Stokes equations (RANS) using Spalart-Allmaras turbulence model [39]. This one-equation turbulence model includes a single transport equation for the turbulent viscosity, and it is particularly suitable in case of aeronautical surfaces and slender bodies in general. Once the flow field solution has been computed, the trajectories of the particles and the collection efficiency are determined applying the PoliDrop and OpenFOAM algorithms to the same initial cloud. In order to compare only particle tracking algorithms, the OpenFOAM solver *uncoupledKinematicParcelFoam* is applied to the SU2 solution which has been

previously converted in the proper format together with the corresponding mesh. Simulations are performed with a cloud density of 100000 droplets/m. Increasing further the number of droplets, no additional improvements are obtained.

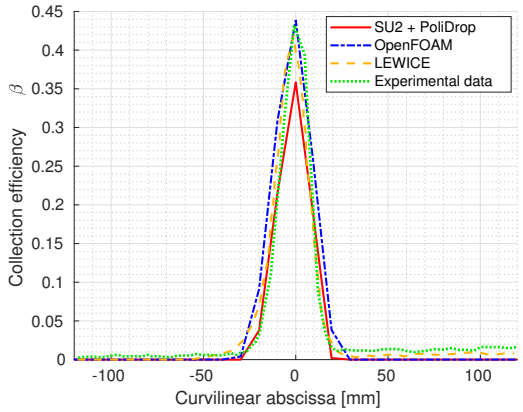

(a) NACA 65_2-415, MVD = 11.5 μm

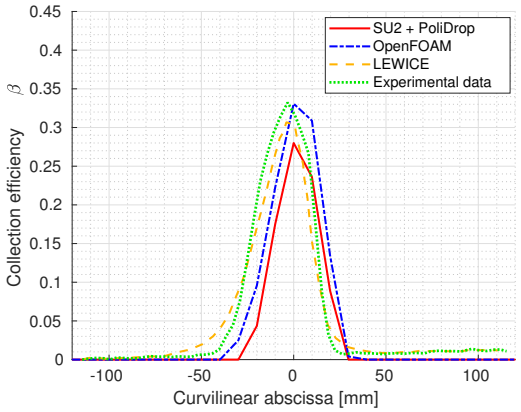

(b) MS(1)-317, MVD = 11.5 μm

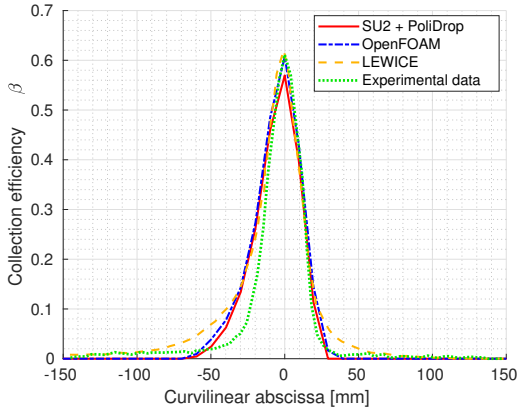

(c) NACA 65_2-415, MVD = 21.0 μm

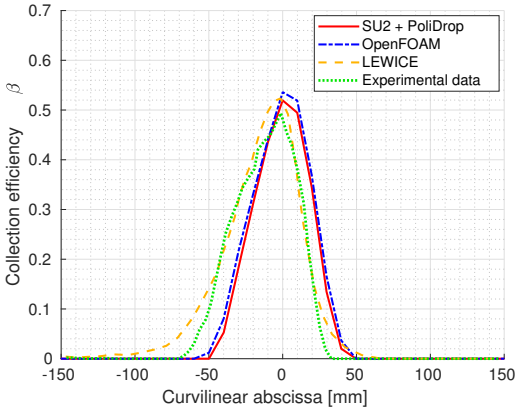

(d) MS(1)-317, MVD = 21.0 μm

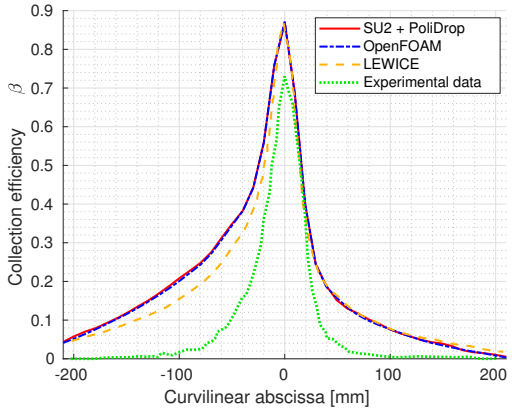

(e) NACA 65_2-415, MVD = 92.0 μm

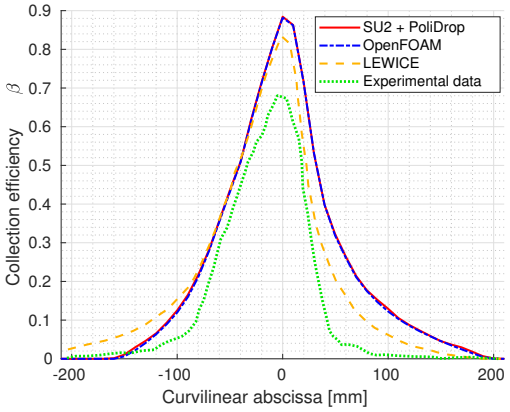

(f) MS(1)-317, MVD = 92.0 μm

Figure 3.13: Collection efficiency as a function of the curvilinear abscissa: comparison for $\alpha = 0$ deg.

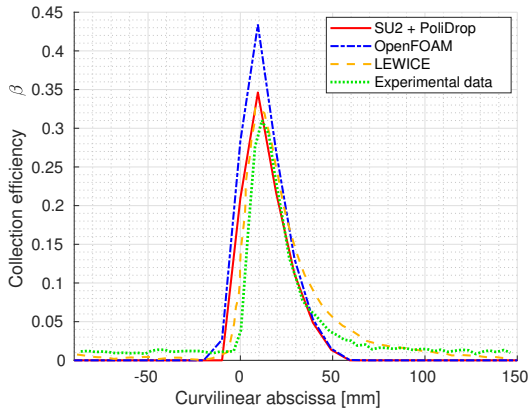

(a) NACA 65_2-415, MVD = 11.5 μm

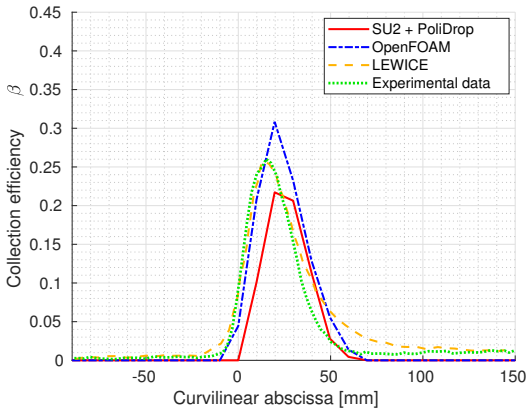

(b) MS(1)-317, MVD = 11.5 μm

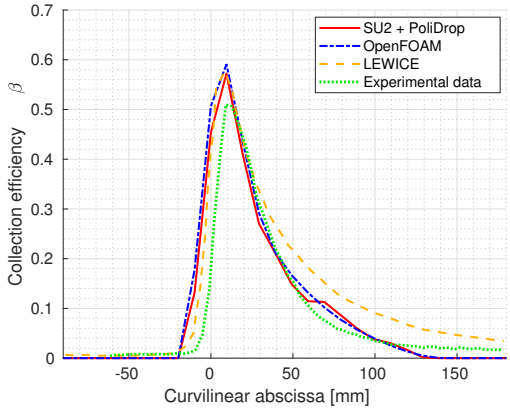

(c) NACA 65_2-415, MVD = 21.0 μm

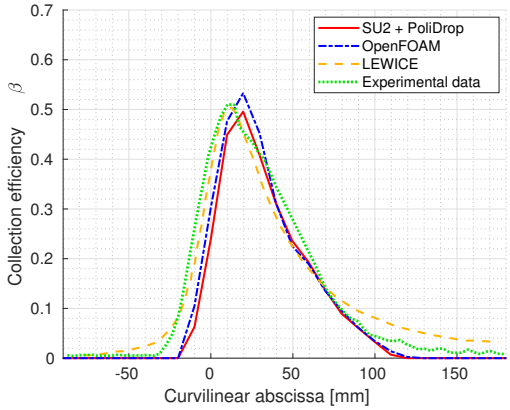

(d) MS(1)-317, MVD = 21.0 μm

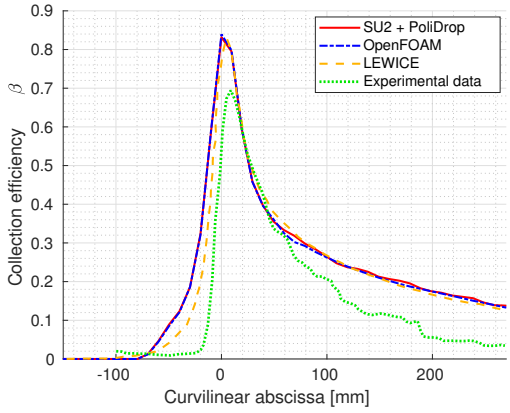

(e) NACA 65_2-415, MVD = 92.0 μm

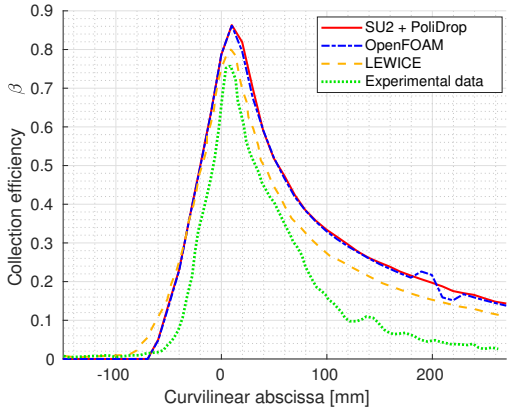

(f) MS(1)-317, MVD = 92.0 μm

Figure 3.14: Collection efficiency as a function of the curvilinear abscissa: comparison for $\alpha = 8$ deg.

As in the previous case (Sec. 3.2.2), collection efficiencies are represented as function of the curvilinear abscissa, measured starting from the leading edge and considered positive on the lower surface and negative on the upper surface. Different results are compared varying the droplets diameter and the angle of attack. With reference to Fig. 3.13 and 3.14 it can be observed that for $\alpha = 0$ deg the collection efficiency has a nearly symmetric trend. The slight skewness is due to the asymmetry of the chosen airfoils, which makes a greater number of particles impinge on the upper surface. When the angle of attack is increased, instead, β assumes a significant skewness caused by the flow field asymmetry, which leads a higher number of parcels to impact on the lower surface of the airfoil.

Moreover, some considerations on the choice of the drag coefficient model can be done, as it has been done in the case of the cylinder (Sec. 3.1.3, Fig. 3.5). For these simulations, the initial velocity of particles was set equal to the fluid velocity. Hence, the relative velocity and consequently the relative Reynolds number are null at the beginning of the time interval considered. By tracking a single droplet trajectory it can be observed that Re_r remains small also in the following time steps and since the results of different C_D models overlap when Re_r approaches zero, the influence of the chosen model is irrelevant as it is shown in Fig. 3.15.

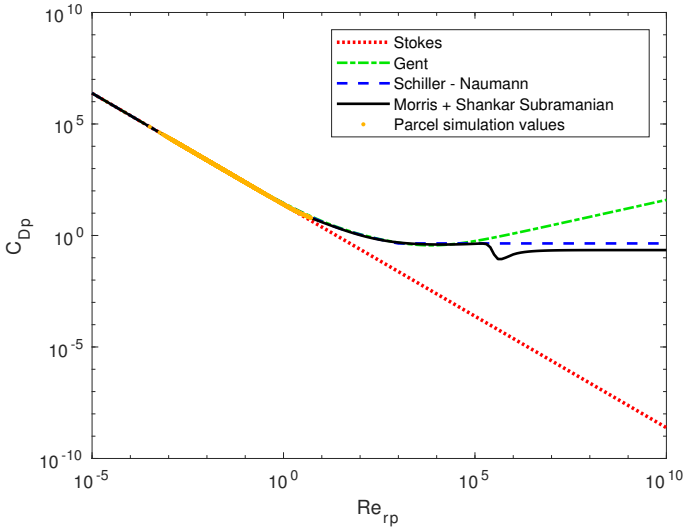

Figure 3.15: Comparison between C_D models and range of values taken by a single tracked droplet in the simulation with NACA 65_2-415 airfoil at $\alpha = 0$ deg and MVD $= 21.0$ μm.

Considering again Fig. 3.13 and 3.14, comparison between different codes and with experimental data is examined. The collection efficiency profiles computed with different codes show a good accordance, which is improved as the droplets diameter is increased. In particular, this is true for the results obtained with PoliDrop and the *OpenFOAM* solver. On the contrary, the accordance between experimental data and

numerical results becomes worse with the increase of the dimension of the particles. This fact can be explained if splashing phenomena occurring for bigger droplets are considered. Indeed, splashing phenomena are not taken into account in the described analytical model. This aspect will be treated in detail in Ch. 4.

Chapter 4

SLD and wall interaction models

In Ch. 3 PoliDrop has been used to compute the collection efficiency in different exemplary cases. As it is shown by comparisons to experimental data, the analytical model implemented is suitable to predict impingement limits and ice shapes when small droplets are involved, while its reliability is reduced when considering droplets with a greater diameter. These bigger droplets are referred to as Supercooled Large Droplets (SLD) and their behaviour is highly influenced by their dimensions. In this chapter SLD icing conditions are analysed, together with the related regulations. Different droplet-wall interaction models are then considered to describe in a specific way the impact behaviour of droplets, so as to improve PoliDrop results when SLD are involved.

4.1 Icing regulations

Icing regulations for transport category airplanes are dictated by the Federal Aviation Administration (FAA) and contained in the Code of Federal Regulations (CFR), in part 25 of title 14 (Aeronautics and Space). Appendix C describes different icing conditions and certification requirements, but only clouds characterised by a maximum droplet diameter $d_{max} < 100\mu m$ are taken into consideration [40]. In 1990s, the FAA became aware that the types of icing conditions considered during the certification needed to be expanded to include SLD in order to increase the level of safety during flight in icing.

Safety concerns about the adequacy of the icing certification standards were brought to the forefront of public and governmental attention by the 1994 accident in Roselawn, Indiana, involving an ATR 72-series airplane. The National Transportation Safety Board (NTSB) identified the probable cause of this accident in the loss of control of the aircraft, caused by the accretion of a ridge of ice aft of the de-icing boots, upstream

of the ailerons, due to a prolonged operation in a freezing drizzle environment, well beyond the aircraft's certification envelope [41]. The investigation further concluded that this ridge of ice contributed to an uncommanded roll of the airplane. Based on these findings, the NTSB recommended changes to the icing certification requirements, since the atmospheric condition that contributed to the Roselawn accident was outside the icing envelope used for certifying transport category airplanes.

The new certification requirements are defined in Appendix O, analysed in Ref. [42]. SLD icing conditions are defined and subdivided into two different atmospheric conditions, following this criterion:

- $100\ \mu m < d_{max} < 500\ \mu m\ \rightarrow$ Freezing Drizzle Environment
- $d_{max} > 500\ \mu m\ \rightarrow$ Freezing Rain Environment

where d_{max} is the maximum drop diameter of the spectra. Each of these environments can be then separated into two subconditions, one with MVD $< 40\ \mu m$ and one with MVD $> 40\ \mu m$. The ambient temperatures at which these two conditions are encountered is shown in Fig. 4.1, together with the corresponding LWC ranges.

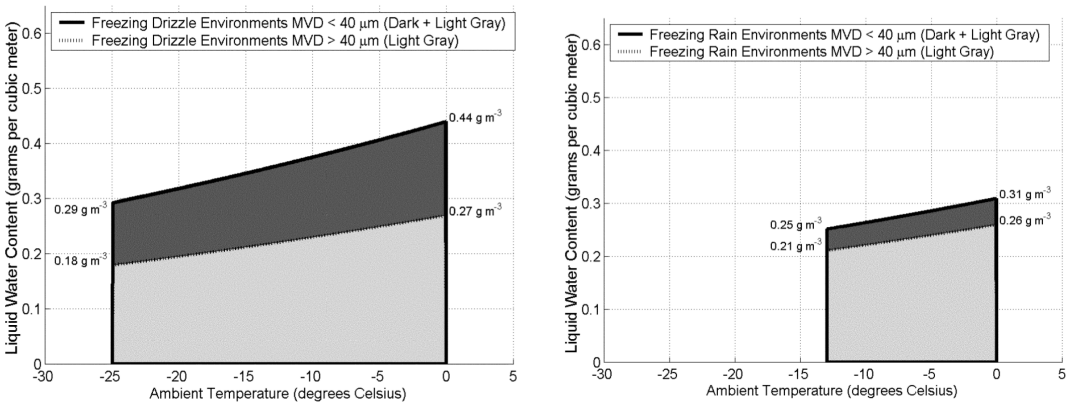

(a) Freezing Drizzle

(b) Freezing Rain

Figure 4.1: Ambient temperature ranges at which freezing drizzle and freezing rain are encountered and corresponding LWC, taken from Ref. [43].

The lowest temperature of icing conditions for Appendix C is as low as 233 K. At these low temperatures, however, only very small droplets can exist in the supercooled state. Instead, SLD icing conditions can occur only in smaller ranges at higher temperatures. In these ranges it is important to know the LWC of the cloud, as it is a fundamental parameter for the computation of the energy requirements during the Ice Protection System (IPS) design and validation. The higher is the LWC, the larger is the liquid water catch rate and consequently the larger is the amount of energy needed by the IPS.

If certification for flight in icing conditions is sought, the aircraft must be capable

of operating safely when encountering environmental conditions described in both Appendix C and Appendix O. *"To establish that the airplane can operate safely [...] an analysis must be performed to establish that the ice protection for the various components of the airplane is adequate, taking into account the various airplane operational configurations"* [40]. The results of the analysis must then be verified with the aid of wind tunnel tests and flight tests. Therefore, adequate engineering tools must be developed and validated for showing compliance with the new rule. In fact, dedicated icing wind tunnels are required to reproduce the correct LWC and MVD spectra and appropriate ice accretion prediction codes are needed to simulate SLD behaviour.

4.2 SLD

As it has been explained in Sec. 4.1, SLD conditions are identified when the cloud droplet maximum diameter is greater than 100 μm. Due to their bigger dimensions these droplets may violate the assumptions originally made for the particle tracking (see Sec. 3.1.1). In particular, larger droplets have a greater tendency to deform under the influence of aerodynamic shear forces, resulting in an increased aerodynamic drag. Moreover, since a lot of supercooled liquid water is caught by the aircraft, run-back ice problems may appear if the IPS cannot provide enough energy to fully clear the ice and to evaporate the liquid water. These run-back ice accretions may bring quite adverse aerodynamic effects, leading to control surface jams and seriously threatening flight safety. It is also likely that these bigger parcels bounce or splash upon impact on the aircraft. If this occurs, the approaching droplet mass is only partially deposited at the predicted impingement location while the splashed or rebounded mass fraction is re-introduced into the flow field, potentially resulting in re-impingements on aircraft lift and control surfaces located downstream of actively protected regions. Since SLD break up and splash when colliding with the aircraft surface and this process is very complicated, ice shapes computation and prediction become more difficult. To predict the correct shape of the ice accretion over a surface, it is thus necessary to modify the model to take into account these events.

The fundamental parameter influencing the droplet behaviour is the surface tension σ, which is a physical property of fluids: it is the measure of the attractive forces between surface particles in the fluid. This phenomenon must be analysed in detail to better understand its role both in the droplet deformation and wall-interaction processes.

Surface tension

The shape of a droplet is determined by the surface tension of the liquid, which is caused by the unbalance of cohesive forces of liquid molecules at the surface. In fact,

inside the volume of the droplet, each molecule is pulled equally in every direction by neighbouring liquid molecules, resulting in a zero net force. On the contrary, the molecules exposed to the surface do not have neighbouring molecules in all directions to provide a balanced net force, and consequently they cohere more strongly to those directly associated with them on the surface. As a result, the liquid voluntarily contracts its surface area to maintain the least surface free energy. This is the reason why small droplets and bubbles are spherical, as the sphere gives the minimum surface area for a fixed volume.

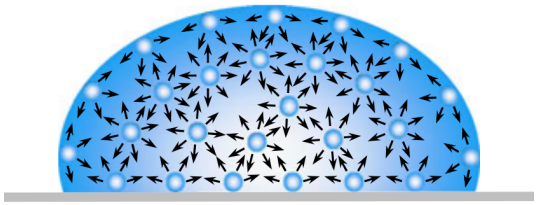

Figure 4.2: Cohesive forces between liquid molecules inside a droplet, giving rise to the surface tension. Ref. [44].

The surface tension of the liquid, together with the solid surface properties, define the wettability of the surface. The latter is determined from the measurement of the contact angle. Given a liquid droplet resting on a flat horizontal surface, the contact angle is defined as the angle between the liquid-solid interface and the line tangent to the liquid-vapour interface from the contact point. A contact angle less than 90 deg indicates that the wetting of the surface is favourable and the surface is said to be hydrophilic. In this case, the fluid spreads over a large area of the surface. On the contrary hydrophobic surfaces are characterised by contact angles greater than 90 deg. This means that the wetting of the surface is unfavourable and the fluid minimises its contact with the surface forming a compact droplet. The phenomenon of wetting, however, is not just a static condition: when the fluid is dropped on the surface, it moves to wet the solid surface. The contact angles formed by expanding and contracting liquid are referred to as the advancing contact angle θ_{adv} and receding contact angle θ_{rec}. The latter in particular is a fundamental parameter influencing the droplet interaction with a dry surface, as it will be explained in Sec. 4.4.1.

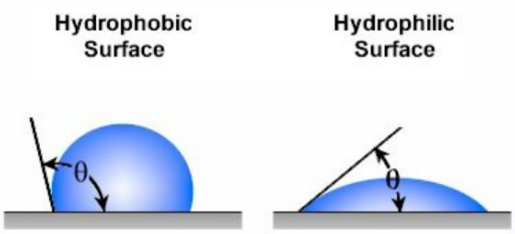

Figure 4.3: Contact angle between the liquid droplet and the surface. $\theta > 90$ deg for an hydrophobic surface, $\theta < 90$ deg for an hydrophilic surface. Ref. [45].

The surface tension and contact angle are strongly dependent on the liquid and solid materials involved and on the surface roughness and heterogeneity. Moreover, surface tension is a function of the fluid temperature. As the temperature raises, the liquid becomes more similar to vapour until the critical temperature T_c is reached. At this point the surface tension is equal to zero. The surface tension of a liquid thus decreases as the temperature is increased and this dependency is shown by experimental data taken from Ref. [46] and [47] represented in Fig. 4.4. In [47] the experimental procedure to measure σ is explained. If a column of a liquid of density ρ is put inside a capillary with inner diameter d, a spherical cap meniscus is formed. Changing the liquid temperature, the height of the meniscus over the surface changes. Measuring this height h and the contact angle θ between the liquid and the container, from the equilibrium between gravity force and surface tension the following relationship is obtained:

$$\sigma = \sigma_0 + \frac{\rho g d}{4 cos\theta}(h - h_0) \tag{4.1}$$

where variables with 0 subscript are referred to the reference state at $T_0 = 273\ K$ and g is the acceleration due to gravity equal to 9.81 m/s^2.

In [46] a useful empirical interpolating relationship have been derived to attempt to quantify the dependency of the surface tension on the temperature. Given a liquid and its temperature, σ can be calculated as:

$$\sigma = a\tau^n(1 + b\tau) \tag{4.2}$$

where for water the following parameters are be used:

- σ = surface tension [N/m]
- T = temperature [K]
- T_c = critical temperature [K] = 647.096 K
- τ = 1-T/T_c
- a = 235.8 $\cdot 10^{-3}$ N/m
- b = -0.625
- n = 1.256

This equation is valid between the triple point temperature (T_0 = 273 K) and the critical point temperature (T_c = 647.096 K) and, as it is shown in Fig. 4.4, it provides reasonably accurate values when extrapolated in the supercooled region, to temperatures as low as T = 248 K.

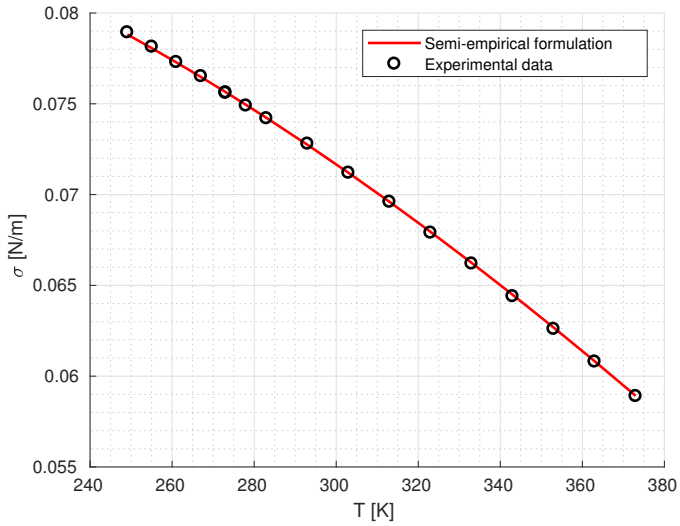

Figure 4.4: Surface tension as a function of temperature for water: comparison between experimental data and semi-empirical interpolating function. Experimental data are taken from Ref. [46] for $T > 273$ K and from Ref. [47] for $T < 273$ K.

However, it is not the surface tension by itself to dictate the droplet behaviour. What really matters is the ratio of the surface tension to inertial and viscous forces. In this context two dimensionless numbers can be defined: the Weber number We and the Ohnesorge number Oh. The Weber number is defined as the ratio of inertial forces to surface tension:

$$We = \frac{\rho_p \mathbf{u_p}^2 d_p}{\sigma} \tag{4.3}$$

while the Ohnesorge number is defined as the ratio of viscous forces to the product of inertial forces and surface tension:

$$Oh = \frac{\mu_p}{\sqrt{\sigma \rho_p d_p}} \tag{4.4}$$

where σ is the liquid surface tension, ρ_p and μ_p are the liquid density and viscosity respectively, d_p is the parcel diameter and $\mathbf{u_p}$ is the parcel velocity.

4.3 Extended drag coefficient

The three forces controlling the deformation and breakup of droplets placed in a continuous fluid are the dynamic pressure, the viscous forces and the surface tension forces. The former two enhance the deformation, whereas the latter counteracts this effect. Since viscosity and surface tension are the most relevant factors to be accounted for, the Reynolds number and Weber number are the adequate dimensionless numbers

to define different flow conditions. In particular, the breakup Weber number is considered, defined as:

$$We_b = \frac{\rho_p(\mathbf{u_f} - \mathbf{u_p})^2 d_p}{\sigma} \tag{4.5}$$

This parameter governs the droplet deformation process from a sphere, through an oblate spheroid, to a final shape close to a disk, as it is shown in Fig. 4.5

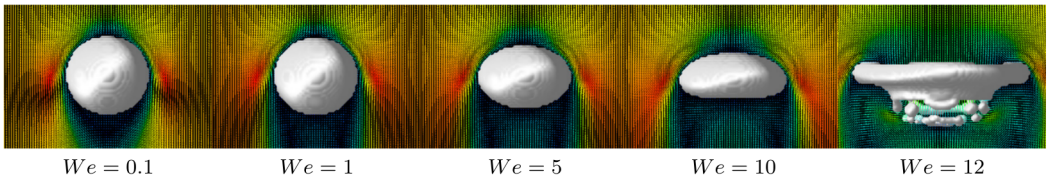

Figure 4.5: Droplet deformation process increasing the breakup Weber number We_b from left to right. Ref. [48].

If the droplet is considered as an oblate disk, its shape is determined by the droplet eccentricity function, which is defined by Eq. 4.6 as the ratio of the difference between equatorial and polar axis to the polar axis length:

$$f = \frac{c - a}{c} = 1 - \frac{a}{c} \tag{4.6}$$

where c is the polar axis and a is the equatorial axis (see Fig. 4.6). According to the definition, f is equal to zero for the sphere and equal to one for the flat disk.

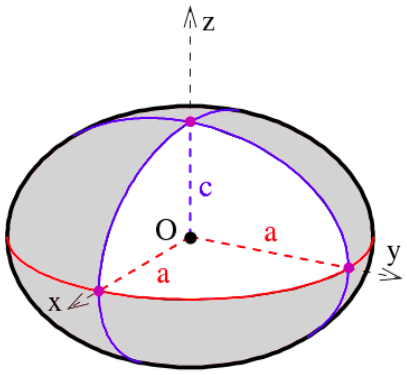

Figure 4.6: Oblate spheroid representation.

According to Honsek and Habashi [49], during the deformation process the droplet shape is described by the following law, giving the spheroid eccentricity as a function of the breakup Weber number:

$$f = 1 - (1 + 0.07\sqrt{We_b})^{-6} \tag{4.7}$$

Therefore, as it is shown in Fig. 4.7, the droplet initial shape is flattened as the breakup Weber number increases. When We_b is small the droplet is not deformed and the eccentricity function is close to zero. As the We_b increases the shape approaches to a disk and f approaches to unity.

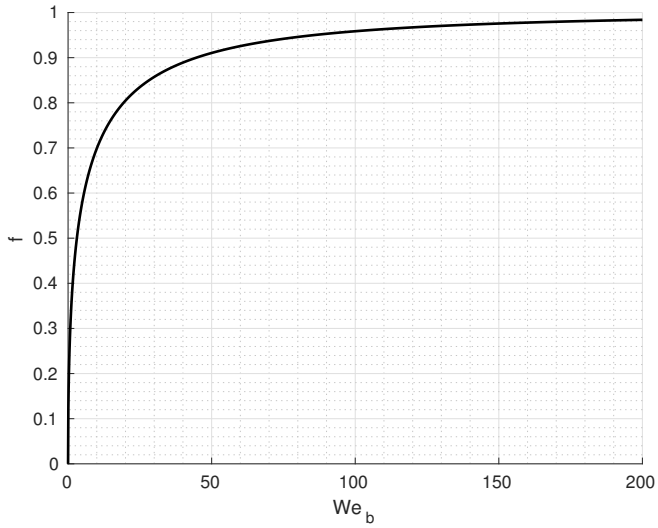

Figure 4.7: Eccentricity function varying the breakup Weber number.

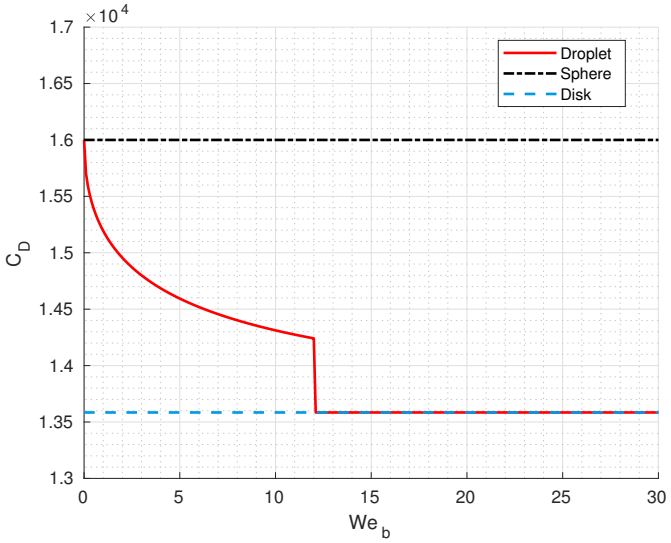

Figure 4.8: C_D-We_b curves for the sphere, the disk and the deformed droplet, for $Re = 0.0015$.

As it is reported in Fig. 4.8 and Eq. 4.8, the drag coefficient of the parcel is thus computed as the weighted mean between the C_D of a sphere and that of a disk, where the weights depend on the parcel eccentricity. This is true until the breakup Weber number of 12 is reached. After this value no steady deformation is obtained

and the droplet breaks up. In this regime, the drag coefficient is modelled as the C_D of a disk.

$$C_D = \begin{cases} (1-f)C_{Dsphere} + fC_{Ddisk} & We_b < 12, \\ C_{Ddisk} & We_b > 12 \end{cases} \tag{4.8}$$

For the sphere drag coefficient the model by Morris and Shankar Subramanian is used, where C_{DMSS} is given by Eq. 3.12:

$$C_{Dsphere} = C_{DMSS} \tag{4.9}$$

For the disk drag coefficient the following model proposed by Clift [35] is used:

$$C_{Ddisk} = \begin{cases} \dfrac{64}{\pi Re}\left(1 + \dfrac{Re}{2\pi}\right) & Re \leq 0.01, \\ \dfrac{64}{\pi Re}(1 + 10^x) & 0.01 \leq Re < 1.5, \\ \dfrac{64}{\pi Re}(1 + 0.138Re^{0.792}) & 1.5 \leq Re < 133, \\ 1.17 & Re \geq 133 \end{cases} \tag{4.10}$$

where $x = -0.883 + 0.906(log_{10}Re) - 0.025(log_{10}Re)^2$ and Re is the particle relative Reynolds number defined in Eq. 3.4.

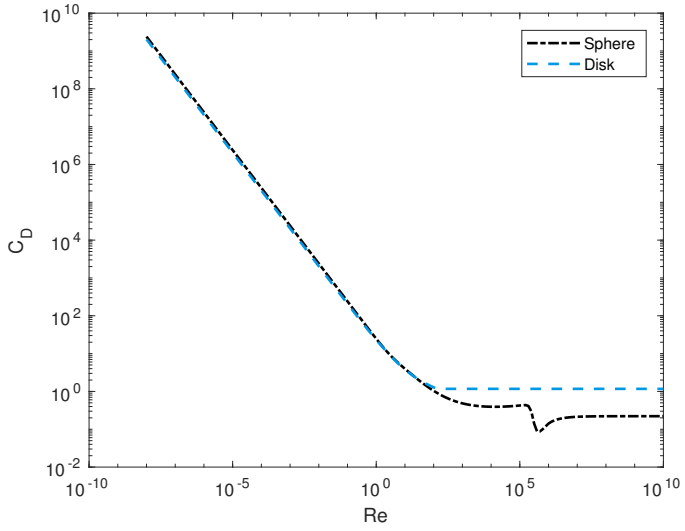

Figure 4.9: Logarithmic C_D-Re curves for the sphere and the disk.

As it is shown in Fig. 4.9 the two functions are nearly equal for low values of the Reynolds number, while they move away from each other at higher Reynolds. In particular, the sphere has slightly higher C_D at low Re and lower C_D at high Re. In all cases considered in Ch. 3, as the relative parcel Reynolds number is always very low, this new model does not introduce remarkable differences with respect to the sphere model. This is confirmed repeating computations for the NACA 65_2-415 airfoil at zero angle of attack using the extended C_D model. Results are shown in Fig. 4.10.

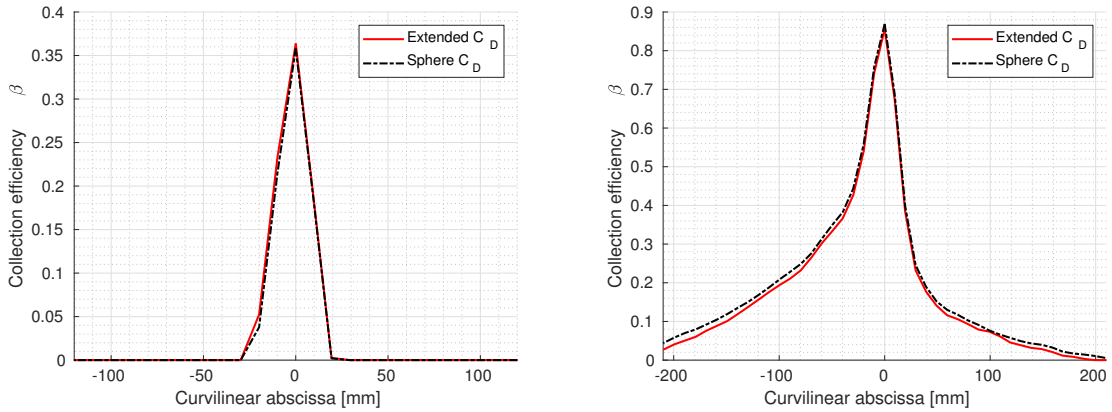

(a) $d_p = 11.5\ \mu m$ (b) $d_p = 92.0\ \mu m$

Figure 4.10: Comparison of the collection efficiency obtained with different C_D models changing the droplets diameter for a NACA 65_2-415 airfoil at $\alpha = 0$ deg.

Remarkable differences should be seen with big particles at high relative Reynolds numbers. Anyway, even increasing further the diameter of the particles and giving an initial velocity different from the flow velocity, the difference between the two models is not appreciable. Considering 100 μm parcels with initial velocity of 200 m/s and taking into account a single parcel trajectory the effect of the different C_D models can be analysed. The result is a slight variation of the time required for the droplets to impinge on the airfoil. The sphere has lower C_D than the real droplet and thus the sphere takes a little lower time than the real droplet to reach the same position on the airfoil. However, the trajectories of the two droplets are the same and therefore there is no difference in the impingement limits and in the value of the collection efficiency β. Even bigger parcels must be used to evaluate the effect of the introduction of a new model for the C_D. In this regard, the collection efficiencies computations for the cylinder case are repeated. Euler CFD simulations are performed so as to compare results with those in Sec. 3.2.1 and particles are tracked in the computed flow field using the extended C_D model. As it is shown in Fig. 4.11(b) the new model for the drag coefficient gives different C_D values in this case as the Reynolds number is sufficiently high. This is due to the fact that big parcels have been used, with an initial velocity different from the flow field

asymptotic velocity ($|\mathbf{u_{0p}}| = 51$ m/s, $V_{\infty f} = 33.5$ m/s). Thanks to their high inertia, droplets maintain a velocity which is considerably different from the flow velocity, in particular, in proximity of the cylinder surface. Here, since Euler equations have been solved, the fluid has a velocity different from zero and tangential to the surface, while parcels arrive with an impact velocity nearly perpendicular to the wall. The variation of the C_D influences particle trajectories and thus introduces an appreciable difference in both the collection efficiency peak value and impingement limits.

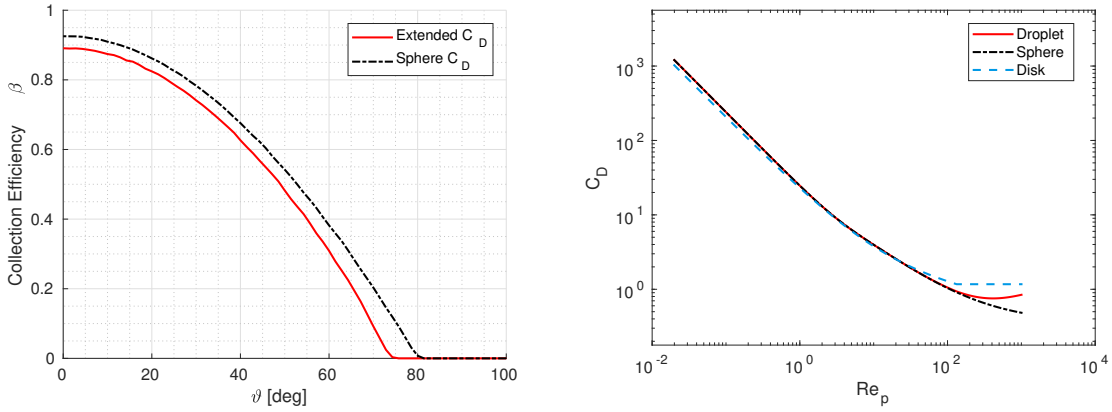

(a) (b)

Figure 4.11: Particle tracking with different C_D models for the cylinder case with $d_p = 10^{-3}$ m. (a) Collection efficiency (b) C_D-Re curves

For all the PoliDrop simulations carried out hereafter, the extended drag coefficient model is used, in order to obtain a better description of the droplet deformation process.

4.4 Droplet-wall interaction models

The drop impact on a solid surface has been studied for more than a century as it is the key element of a wide variety of phenomena encountered in technical applications, such as spray cooling, fuel injection in internal combustion engines, liquid atomisation and ice accumulation. Indeed, due to their big dimensions, SLD not only deform under the influence of aerodynamic forces, but also may have interesting interactions with the wall when they impact on the body surface. This process must be studied in detail to improve the computation of the collection efficiency and ice accretion in SLD atmospheric conditions, taking into account that the outcomes of a drop impact are extremely different depending on a huge set of parameters. The droplet may impinge on a dry solid surface, on a thin liquid film on a wall or on the free surface of a deep pool. The surface may be rough or smooth, hard or soft, flat or curved, hot or cold. The impact might be normal or oblique and the interaction

between the liquid of the drop and the material constituting the body surface can result in a myriad of possible configurations. The resulting interaction depends on the properties of the surface (roughness and wettability) and those of the liquid (density, viscosity, surface tension). Moreover, the drop size, the impact velocity and its direction relative to the surface are key parameters influencing the phenomena. Gravity effects are typically not important in the phenomena accompanying drop impact. Moreover, in very strong impacts, liquid-compressibility effects should also be considered [50], but this is out of the scope for the present work. Due to the complexity of the phenomenon, different dimensionless groups governing drop impact are used. The fundamental dimensionless numbers related to the droplet are the Weber number and the Ohnesorge number, already defined in Eq. 4.3 and 4.4, which gives a measure of the importance of surface tension forces with respect to the other forces involved in the process. Other two important parameters related to the surface are:

- dimensionless film thickness: $H = \frac{h}{d_p}$
- dimensionless surface roughness: $R = \frac{R_a}{d_p}$

where h is the thickness of the pre-existing liquid film and R_a is the surface roughness. Considering these quantities the drop-wall interaction can be classified as follows, depending on the surface on which the droplet impinges:

$$\begin{cases} \text{Dry surface, } H = 0 \\ \\ \text{Wet surface, } H \neq 0 \begin{cases} \text{Deep splash, } H \gg 1 \\ \\ \text{Liquid film, } H \sim 1 \begin{cases} \text{Very thin film, } H \sim R \\ \\ \text{Thin film, } H \gg R \end{cases} \end{cases} \end{cases}$$

These conditions lead to very different outcomes, which are now analysed in detail.

4.4.1 Dry surface

Rioboo et al. [51] conducted several experimental studies to explore the possible outcomes of the drop impact on a dry surface. The purpose of their work was to introduce a systematic classification and indicate qualitatively the influencing parameters. In [52] Rioboo et al. subdivided the impact process into four phases. The first phase is the *kinematic phase*. The liquid droplet, with the shape of a truncated sphere, is compressed and a shock wave is formed. Then the *spreading phase* begins, characterised by the formation of a radially expanding film, called lamella. The lamella is ejected from the base of the drop and forms a thin film bounded by a rim. Increasing the impact velocity or drop diameter leads to faster spreading, while

increasing the surface tension or viscosity leads to slower expansion. Wettability is influential throughout the entire spreading phase and, although the film is increasing in diameter, the receding contact angle determines the maximum spread diameter and the behaviour of the film afterwards, in the *relaxation phase*. This may have different outcomes, depending mainly on the magnitude of the receding contact angle and surface roughness. The final phase is called *equilibrium/wetting phase*, where the lamella decelerates strongly attaining some constant diameter or, for highly wettable surfaces, continues slowly to wet the surface.

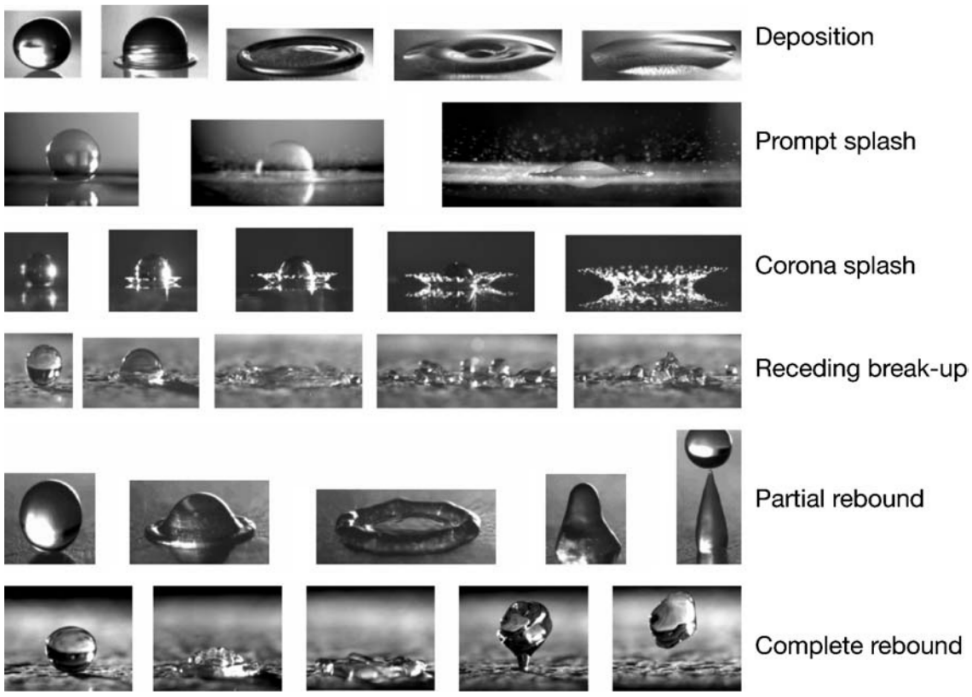

Figure 4.12: Morphology of drop impact on a dry surface: examples of the six kinds of outcomes obtained changing parameters. Ref. [51].

As it has been mentioned, the relaxation phase may have different outcomes, pictured in Fig. 4.12:

- **Deposition** is considered when the drop deforms and stays attached to the surface during the entire impacting process, without any breakup. Deposition usually occurs for small droplets on a smooth surface and it is enhanced by the fluid viscosity. Increasing the viscosity, in fact, reduces the probability of all breakup mechanisms.
- **Prompt splash** is characterised by the generation of droplets directly at the contact line at the beginning of the spreading phase, when the lamella has high radial velocity. It is influenced by the surface structure, in particular, it is observed only on rough surfaces. High roughness amplitude R_a and low roughness wavelength R_w favour its onset at lower impact velocities.

- **Corona splash** occurs when the lamella takes the shape of a crown, consisting of a thin liquid sheet with an unstable rim at the top, from which numerous small secondary droplets are ejected. The corona splash takes place only for the fairly restricted condition of a very smooth surface and it is enhanced by larger drops and lower surface tension. For rough surfaces the prompt splash sets in before a corona can be formed.
- **Receding breakup** occurs when, during the receding phase, some drops are left behind by the receding lamella. This is due to the fact that, as the liquid retracts from its maximum spreading radius, the dynamic contact angle decreases and, if θ_{rec} reaches the limiting value of zero, the surface becomes fully wettable. Receding breakup is promoted by high impact velocities $\mathbf{u_i}$, leading to a large spreading diameter and high receding velocity, which in turn results in a low dynamic receding angle.
- **Partial rebound** occurs during the receding phase if the receding contact angle is low. In this outcome part of the drop stays attached to the surface, while some part rebounds.
- **Complete rebound** occurs when the entire drop rebounds on the surface, when the receding contact angle is high and the receding phase is energetic enough.

	$\mathbf{u_i}$	$\mathbf{d_p}$	σ	$\mu_\mathbf{p}$	$\mathbf{R_a}$	$\mathbf{R_w}$	$\theta_\mathbf{rec}$
Deposition	↓	↓		↑	↓		
Prompt splash	↑	↑	↓	↓	↑	↓	
Corona splash	↑		↓	↓	↓		
Receding breakup	↑		↑	↓			↑
Partial rebound	↑		↑				↑
Complete rebound			↑				↑

Table 4.1: Summary of the influence of each parameter on each of the six outcomes. Arrows indicate the direction of the parameter variation required to obtain the considered outcome. Ref. [51].

Tab. 4.1 summarises the influence of each parameter on the drop-wall interaction. However, it is also important to underline the interdependency of some parameters and the fact that not all the six distinct outcomes are achievable given a droplet-surface combination. In this context, it is difficult to use few dimensionless impact parameters to define ranges for each outcome. The problem is instead simplified is the impact on a liquid film is considered.

4.4.2 Wet surface

If the wall is covered by a liquid film, the dynamics of the drop impact depends on the characteristics of the impinging drop (diameter and impact velocity), the physical

characteristics of the liquid (viscosity, surface tension, density) and on the film thickness. Bai and Gosman [53] identified four different mechanisms of droplet-wall interaction on liquid films, illustrated schematically in Fig. 4.13:

- **Stick:** At sufficiently low impact velocities and surface temperatures, the impinging droplet sticks to the impact surface in approximately spherical form.
- **Rebound:** At low impact velocities a film of air may be entrained between the impinging droplet and the liquid film, causing the droplet to rebound off the surface.
- **Spread:** At moderate impact velocities, the impinging droplet merges with the liquid film already existing on the surface.
- **Splash:** At sufficiently high impact velocities, the impinging droplet splashes. Upon impact a crater is formed with a crown at the periphery, where liquid jets become unstable and breaks up into a cloud of secondary droplets.

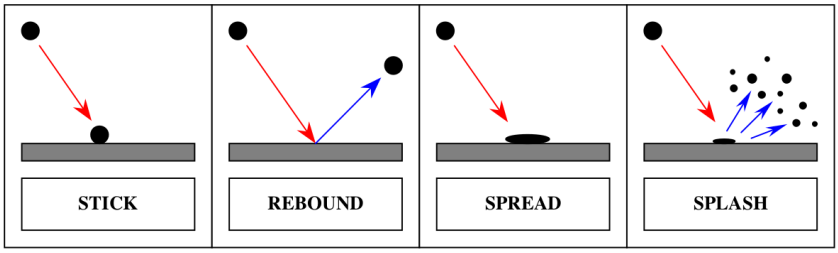

Figure 4.13: Schematic representation of droplet-wall interaction mechanisms from Ref. [49].

Due to the complexity of the phenomenon an analytical formulation of the droplet impingement on a liquid film is not possible. In order to study the different outcomes, two different approaches are possible: automatic tracking through complete three dimensional simulations [54] or experimental investigations [55]. Simulations require an adaptive grid scheme for two-phase flows to be used and the Navier-Stokes equations must be complemented with the Volume Of Fluid (VOF) method to model the gas-liquid interface. This procedure demands a significant computational effort, which may be avoided if a semi-empirical method is developed and calibrated through comparison with experimental evidence.

Thereby, for the introduction of droplet-wall interaction modelling in the PoliDrop software, semi-empirical descriptions are used for the rebound and splash mechanisms. As regards the stick and spread mechanisms only require the droplet to remain on the surface after the impact and therefore are already accounted for in the original PoliDrop algorithm. Semi-empirical models must first of all define ranges of applicability. To define whether or not the parcel impact conditions fall in the prescribed range, surface characteristics must be known and impinging parcel properties must be determined. The impingement point is computed by PoliDrop as

the point where the particle trajectory intersects the body surface and the normal direction to the considered panel is extracted from the mesh geometry. The impact angle φ_i is defined as the angle between the normal vector $\mathbf{n}$ and the velocity vector $\mathbf{u_i}$ and it is used to decompose the impact velocity in its normal and tangential components, $u_{n,i}$ and $u_{t,i}$.

$$\varphi_i = acos\left(\frac{\mathbf{u_i} \cdot \mathbf{n}}{|\mathbf{u_i}|}\right) \tag{4.11}$$

$$\begin{aligned} u_{n,i} &= |\mathbf{u_i}| cos\varphi_i \\ u_{t,i} &= |\mathbf{u_i}| sin\varphi_i \end{aligned} \tag{4.12}$$

Once these quantities have been calculated, relations to compute the properties of the rebounded and splashed parcels are needed. Different empirical models are available, which slightly differ from each other mainly in terms of the selected coefficients. Here the work from Honsek and Habashi [49] is followed, which embeds the model proposed by Bai and Gosman [53] for a representative description of the bouncing phenomena and the impingement model developed by Trujillo and Lee [56] for the description of the splashing process.

Rebound

According to Bai and Gosman [53], the distinction between bouncing and spreading regimes is based on a critical range of Weber numbers:

$$10 \leq We_s \leq 1320 Oh^{0.36} \tag{4.13}$$

where We_s is the impact Weber number defined as:

$$We_s = \frac{\rho_p u_{n,i}^2 d_i}{\sigma} \tag{4.14}$$

In Eq. 4.14, ρ_p is the parcel density, σ is the liquid surface tension, d_i is the diameter of the impinging parcel and $u_{n,i}$ is the normal impact velocity. Considering the liquid density and surface tension fixed and equal to the water values at 273 K, the dependency of condition Eq. 4.13 from the other parameters can be studied. As it is shown in Fig. 4.14, the lower limit is fixed ($We_s = 10$), while the upper limit is a function of the droplet diameter: as the diameter is increased, the upper limit is lowered. Thus, in general, small parcels are more likely to rebound upon impact, as the critical range of Weber numbers is wider. The Weber number trend as a function of the diameter and the velocity must also be considered. From its definition, We_s is a quadratic function of the impact velocity. This parabola steepens as the parcel

diameter increases and consequently the range of admissible velocities for rebound is narrower for bigger parcels.

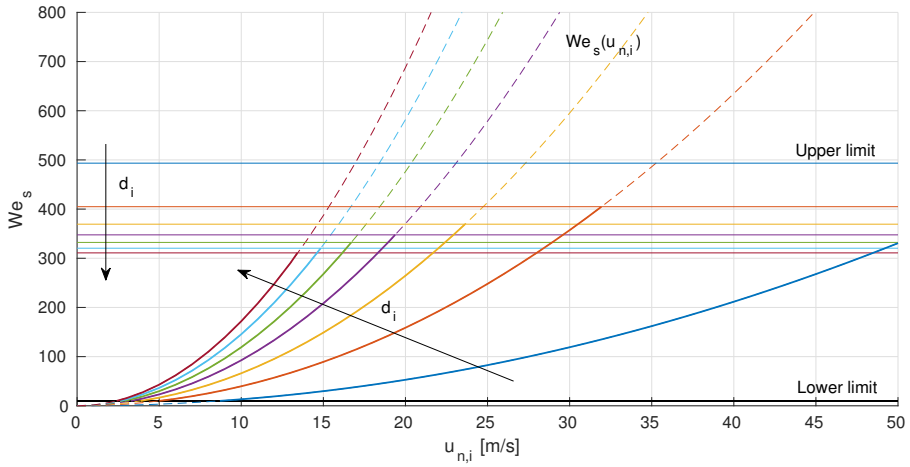

Figure 4.14: Representation of the Weber admissible region for rebound as a function of the normal impact velocity $u_{n,i}$ and impinging particle diameter d_i varying from 10 μm to 130 μm

When condition Eq. 4.13 is satisfied, after the impact on the wall the whole droplet is bounced and there is no water left on the surface. The parcel is reintroduced in the flow field with a new velocity vector, whose components can be computed as:

$$\begin{aligned} u_{t,r} &= +u_{t,i}\frac{5}{7} \\ u_{n,r} &= -u_{n,i}(a + b\xi + c\xi^2 + d\xi^3) \end{aligned} \tag{4.15}$$

where a, b, c, d are constants, whose values are adjusted on the basis of experimental data (according to Ref. [49] $a = +0.9930$, $b = -0.0307$, $c = +0.0272$ and $d = -0.0086$) and ξ is the parcel incidence angle defined as:

$$\xi = \frac{\pi}{2} - \varphi_i \tag{4.16}$$

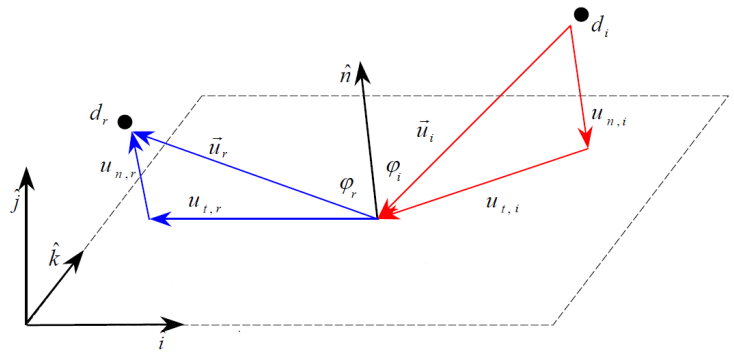

Figure 4.15: Schematic representation of pre-impact and post-impact angles and velocity vectors for the rebound case.

Splash

According to Trujillo and Lee [56], the occurrence of the splashing phenomenon depends on the value of the Cossali parameter K_c, considered by many authors [50, 55, 57] the best dimensionless number to identify the splashing/deposition limit and defined by Cossali as the product of the impact Weber number, defined by Eq. 4.14, and a negative power of the Ohnesorge number, defined by Eq. 4.4:

$$K_c = We_s Oh^{-2/5} = \left(\frac{\rho_p^6 u_{n,i}^{10} d_i^6}{\sigma^4 \mu_p^2} \right)^{1/5} \tag{4.17}$$

The transition from spreading and splashing regimes occurs when a critical value of the Cossali parameter is exceeded, namely:

$$K_c \geq 540 R^{-0.35} \tag{4.18}$$

where R is the dimensionless roughness parameter defined as the ratio between the surface roughness R_a and the impinging parcel diameter d_i (Eq. 4.19). The surface roughness depends on the material and on the technological process for its production. The minimum roughness amplitude obtainable is of the order of 0.1 μm and this is the value that will be set for simulations of drop impact over smooth surfaces.

$$R = \frac{R_a}{d_i} \tag{4.19}$$

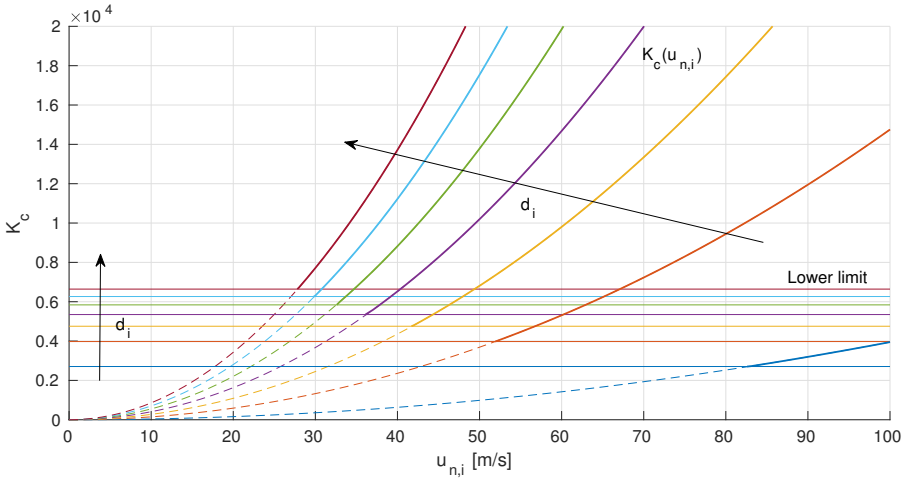

Figure 4.16: Representation of the Cossali parameter admissible region for splash as a function of the normal impact velocity $u_{n,i}$ and impinging particle diameter d_i varying from 10 μm to 130 μm

The Cossali parameter is a function of the parcel density ρ_p, the liquid surface tension σ, the diameter of the impinging parcel d_i and the normal impact velocity $u_{n,i}$. Taking once again fixed values for the liquid density and surface tension, the dependency of the splashing condition from the other parameters can be studied. Fig. 4.16 shows the quadratic dependency of the Cossali parameter from the impact velocity and the steepening of the curve due to an increase of the dimension of the impinging parcel. Moreover, the critical value defined in Eq. 4.18 as the lower limit for splashing raises as the dimensionless roughness decreases. This decrease is obtained increasing the parcel diameter or decreasing the surface roughness, which is here considered fixed and equal to 0.1 μm. Therefore, for bigger parcels the splashing condition is more restrictive, but at the same time the Cossali parameter results to be higher with respect to smaller parcels if the other parameters are kept fixed.

If the splashing condition is satisfied, when the drop impacts on the wall, part of its mass remains stuck on the surface while the remaining portion is splashed away in the form of a cloud of small secondary droplets. Defining the Yarin and Weiss splashing parameter K_y [58] as:

$$K_y = K_c^{5/16} \left[\frac{3}{2} \left(\frac{LWC}{\rho_p} \right)^{1/3} \right]^{-3/8} \tag{4.20}$$

the portion of splashed mass with respect to the impinging mass, called mass loss coefficient Φ, can be calculated [59]:

$$\Phi = \frac{m_s}{m_i} = \frac{3.8}{\sqrt{K_y}} \left[1 - e^{-0.85(K_y - 17)} \right] \tag{4.21}$$

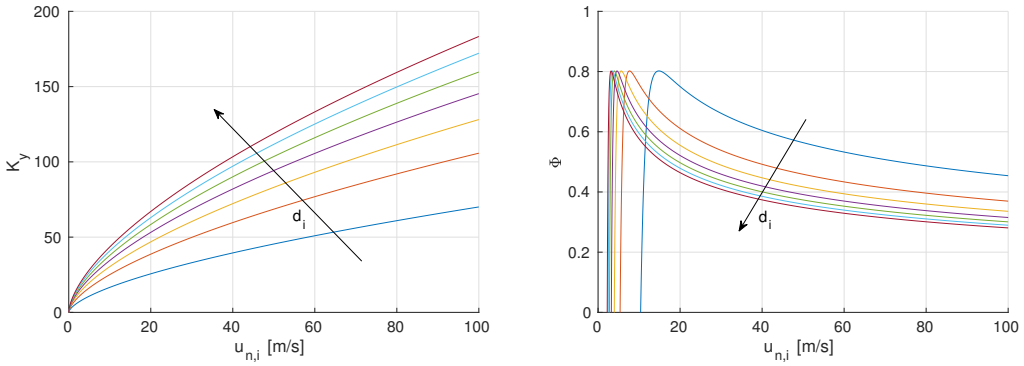

(a) (b)

Figure 4.17: Splashing parameters trend as a function of the normal impact velocity $u_{n,i}$ and impinging particle diameter d_i varying from 10 μm to 130 μm. (a) Yarin and Weiss splashing parameter K_y, (b) mass loss coefficient Φ.

In Fig. 4.17 the trend of Eq. 4.20 and 4.21 is shown. In this case all the parameters are fixed (LWC = 0.5 g/m^3, $|\mathbf{u_{rel}}| = 0.001$ m/s, $\rho_p = 1000$ kg/m^3, $\rho_f = 1$ kg/m^3, $\mu_f = 1.81 \cdot 10^{-5} kg/ms$), except for the impact velocity and the parcel diameter. The splashing parameters K_y is, by definition, always positive and it results to be proportional to $u_{n,i}^{5/8}$. For a given velocity its value is increased with the parcel diameter. The mass loss coefficient is bounded between 0 and 1 for physical reasons: the splashed mass must be a positive number but it cannot be greater than the impinging mass. By the way the formula may give negative values for low impact velocities. This occurs at higher velocities as the parcel diameter is decreased and therefore a lower limit on Φ must be set. As far as the number of secondary droplet fragments N_s is concerned, a linear relationship is found to exist between the total number of droplets resulting from a single splash and the square of the impact velocity, as shown in Fig. 4.18, where the ratio between the module of the impact velocity and its normal component is assumed to be unitary. According to experimental data reported by Stow and Steiner [60], the number of secondary droplet fragments N_s can be computed as:

$$N_s = \frac{1}{22}\left[0.00437\left(K_c\left(\frac{|\mathbf{u_i}|}{u_{n,i}}\right)^2 - K_{cdry}\right) - 44.92\right] \tag{4.22}$$

where $K_{cdry} = OhRe_r^{5/4}$ is the Cossali parameter for a dry surface, defined by Mundo et al. in Ref. [61] and Re_r is the particle relative Reynolds number defined in Eq. 3.4. In addition to the quadratic dependency on the impact velocity, the number of droplets results to increase with the impinging droplet diameter. Moreover, non physical negative values may be computed with Eq. 4.22 for low impact velocities. Physical boundaries can be attributed to Φ and N_s, as explained in detail in Sec. 4.5.2.

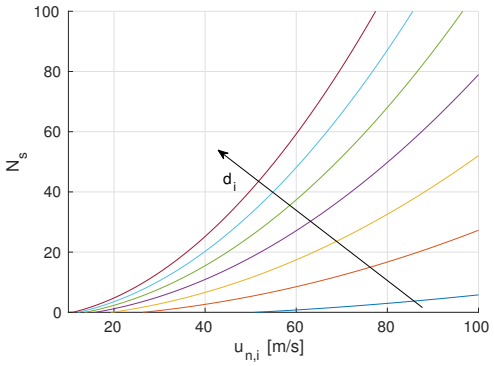

Figure 4.18: Number of secondary droplet fragments N_s as a function of the normal impact velocity $u_{n,i}$ and impinging particle diameter d_i varying from 10 μm to 130 μm.

Once the mass loss ratio Φ and the number of secondary droplets N_s are known, from the mass conservation law it is possible to obtain an expression for the diameter of the droplet fragments d_s. The mass conservation law reads:

$$m_s = \Phi m_i \tag{4.23}$$

Substituting $m_s = N_s \rho_p \frac{4}{3}\pi \left(\frac{d_s}{2}\right)^3$ and $m_i = \Phi \rho_p \frac{4}{3}\pi \left(\frac{d_i}{2}\right)^3$ into Eq. 4.23, algebraic simplification leads to:

$$d_s = d_i \left(\Phi \frac{1}{N_s}\right)^{1/3} \tag{4.24}$$

The resulting splashed droplets are then reintroduced in the flow field with a new velocity vector, which is assumed to be equal for all the droplets. The normal and tangential components of the velocity vector can be calculated from the impinging velocity using semi-empirical formulas by Trujillo and Lee [56]:

$$\begin{aligned} u_{t,s} &= +u_{t,i}(0.85 + 0.0025\varphi_i) \\ u_{n,s} &= -u_{n,i}(0.12 + 0.0020\varphi_i) \end{aligned} \tag{4.25}$$

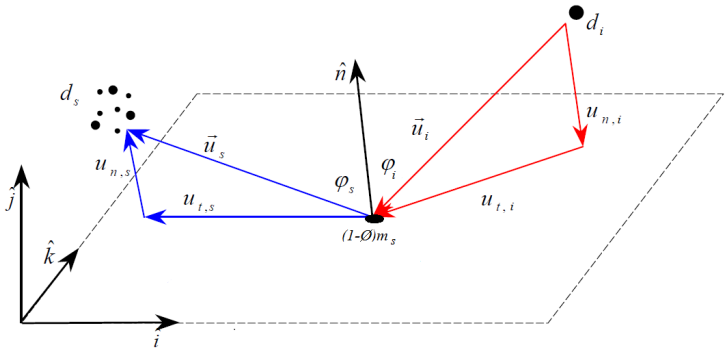

Figure 4.19: Schematic representation of pre-impact and post-impact angles and velocity vectors for the splash case.

Eventually, to compute the collection efficiency in the case of splashing droplets it is necessary to change its definition. In fact, the collection efficiency β is the ratio between the impinged parcels density and the cloud density. In Eq. 3.6 these densities are calculated as the number of parcels per unit area or volume. However, this density computation is exact only if all parcels in the cloud have the same mass. Instead, when a parcel splashes it is divided in many secondary droplet fragments with a different radius with respect to the impinging droplet, and therefore different mass. It is thus necessary to account for the actual mass of the droplets to compute

correctly the collection efficiency. Density is redefined as the mass per unit area or volume and the collection efficiency β becomes:

$$\beta = \frac{collected\ masses/panel\ area}{total\ mass/cloud\ volume} \tag{4.26}$$

This new definition does not introduce any difference when there are no splashing parcels, but the difference is remarkable when splashing occurs.

Test Case

The presented models is implemented in PoliDrop and then tested on a simple problem: parcels impingement on an oblique wall. The flow field is air confined by three straight walls and an oblique wall inclined by 30 degrees with respect to the vertical direction. Air is still while ten water droplets with a diameter of 1 mm are shot with an initial velocity of 200 m/s. All the four types of droplet-wall interaction identified by Bai and Gosman [53] are enabled and the wall roughness is set to be equal to $R_a = 0.1\mu m$. The results obtained with PoliDrop are shown in Fig. 4.20, where we can see three parcels are seen to splash, three parcels are seen to stick/spread and four parcels are seen to rebound.

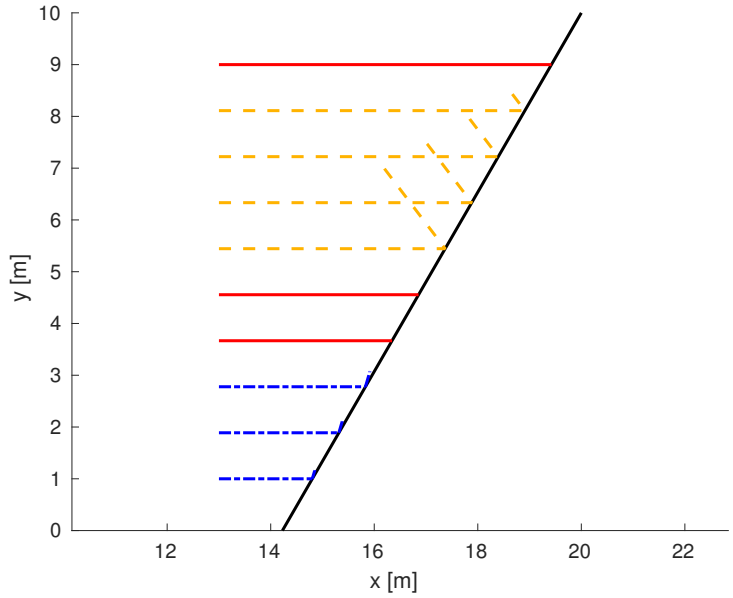

Figure 4.20: Impinging parcels on a wall inclined by 30 degrees with respect to the vertical direction. All types of wall interaction are shown: sticking/spreading (red), splashing (blue) and bouncing (yellow).

Tab. 4.2 summarises the main results from the PoliDrop simulation. Splashing parcels are the first ones impinging on the wall. Due to their high impact velocity and high

energy the droplets break up: one part of the original droplet remains stuck to the wall while the other originates a huge number of droplet fragments with small radius which are reintroduced in the flow field with a new initial velocity. The splashing phenomenon is highly dissipative, hence the post impact velocity is much lower than the impinging velocity. As these fragments have small inertia they are soon arrested by the air viscosity. Consistently with Fig. 4.17 and 4.18, as the impact velocity is lowered the mass loss ratio is enhanced and the number of secondary fragments decreases. Consequently the secondary droplet diameter is increased.

ID	$u_{n,impact}$	Wall Interaction	$\|u\|_{pre-impact}$	$\|u\|_{post-impact}$	N_s	Φ
0	24.60	Splash	28.41	12.45	156	0.196
1	15.73	Splash	18.16	7.96	62	0.225
2	10.56	Splash	12.19	5.34	27	0.255
3	7.28	Spread	8.41	0	0	0
4	5.09	Spread	5.88	0	0	0
5	3.55	Rebound	4.11	3.78	1	1
6	2.44	Rebound	2.81	2.59	1	1
7	1.60	Rebound	1.85	1.70	1	1
8	0.97	Rebound	1.11	1.03	1	1
9	0.49	Stick	0.57	0	0	0

Table 4.2: Summary of results and significant parameters extracted from the PoliDrop simulation with droplet-wall interaction modelling.

Then, parcels with slightly lower impact velocity, have not enough energy to produce secondary droplets. Thus, they remain completely stuck to the wall and spread there. The next parcels impacting have lower impact energy and the film of air trapped between the droplets and the surface causes them to rebound off the wall after the impact. The impinging parcel is reintroduced in the flow with a new value of velocity, which has a different direction but similar module with respect to the impinging velocity. Thanks to their high inertia these droplets rapidly move away from the wall before being slowed down by the shear stresses. The last impinging parcel has an impact energy so low that it just stick to the wall. This test case is instructive as it shows the behaviour of parcels in the four droplet-wall interaction regimes all at once. However, it is of major interest to consider cases of practical relevance, such as droplets impingement on airfoils.

4.5 In-flight wall interaction

In this section the droplet-wall interaction model proposed by Honsek and Habashi [49] and analysed in Sec. 4.4.2 is tested on airfoils, to assess its accuracy for in-flight ice accretion simulations. Results from the new model are compared with those from

the basic stick model and experimental data. Advantages and disadvantages of the considered model are pointed out and a modified model is proposed.

4.5.1 Honsek-Habashi model

PoliDrop simulations are carried out on the NACA 65_2-415 airfoil at zero angle of attack changing the droplets dimension. Simulation parameters are the same of Sec. 3.3. The comparison with experimental data is performed plotting on the same graph the collection efficiency values as functions of the curvilinear abscissa. Rebound and splashing models are activated one at a time to analyse their effects separately.

Rebound

The first model to be considered is the rebound model. In Sec. 4.4.2 it has been said that, when the rebound condition Eq. 4.13 is satisfied, the impinging droplet is bounced away from the surface and no water is left behind on the wall. Instead, if the condition is not satisfied the stick model is recovered. The analysis of the rebound condition performed in Fig. 4.14 revealed that small parcels are more likely to rebound upon impact and this is reflected in the results of simulations on airfoils. Indeed, comparing Fig. 4.21 (a) and (b) it is evident that small parcels rebound more than big parcels.

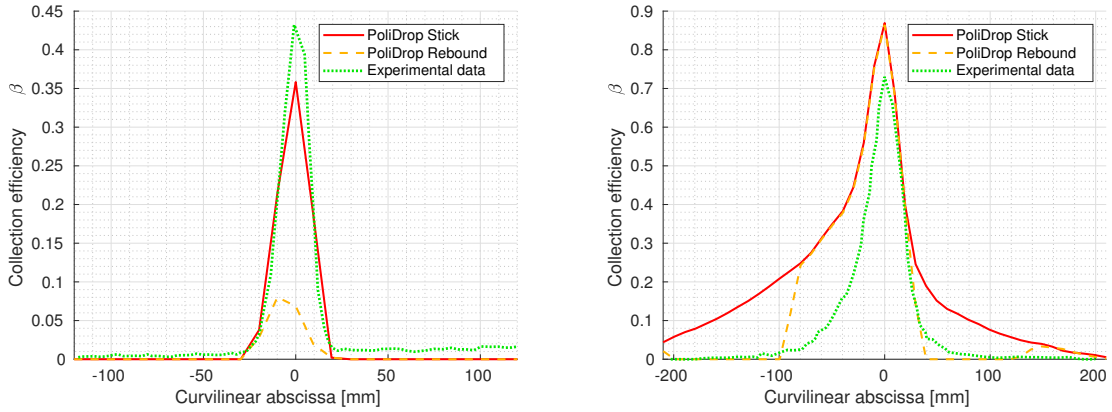

(a) NACA 65_2-415, MVD = 11.5 μm

(b) NACA 65_2-415, MVD = 92.0 μm

Figure 4.21: Collection efficiency as a function of the curvilinear abscissa: comparison between rebound model, stick model and experimental data for $\alpha = 0$ deg and different particles dimension.

In particular, Fig. 4.21(b) shows that parcels with a diameter of 92.0 μm rebound only close to the impingement limits. In fact, due to the relative direction of impact

velocity and surface normal, in these regions droplets impinge on the body wall with a low normal component of the impact velocity, and thus the rebound condition is satisfied. Close to the stagnation point, instead, the impinging velocity is nearly parallel to the panel normal and, together with the big parcels dimension, it results in a high impact energy. Hence, the higher limit for rebound is exceeded and the droplets spread on the wall. The result is a collection efficiency with a peak coincident with the stick model and lower values in proximity of the impingement limits, which make the trend closer to experimental data. If smaller parcels are considered, the yellow curve in Fig. 4.21(a) shows a trend of the collection efficiency which is completely wrong if compared with the green curve of experimental results. This error is due to the fact that all impinging parcels satisfy the rebound condition and therefore are bounced away from the surface and reintroduced on the flow field, as it is shown in Fig. 4.22. Note that post impact droplets are the same droplet that have impinged on the surface (they have the same diameter) but with a different velocity. Some of these parcels re-impinge upon second impact, while others are just carried away by the flow.

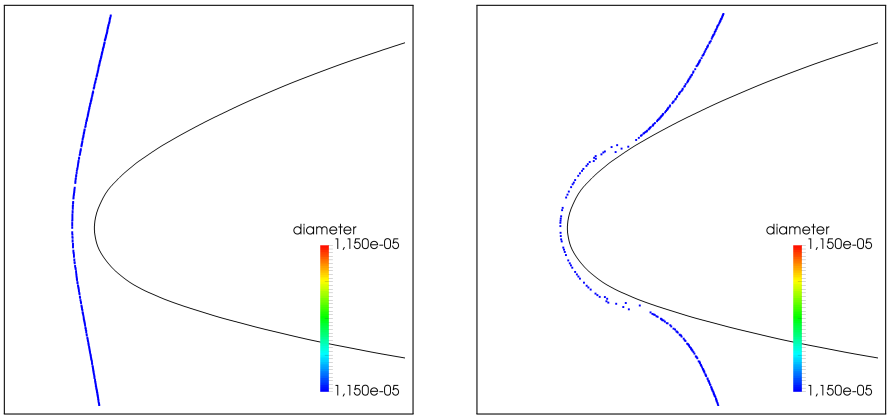

Figure 4.22: Visualisation of rebounding parcels with $d_p = 11.5\ \mu m$ on the leading edge of a NACA 65_2-415 airfoil. Colours represent the diameter of the parcels: all parcels are blue as they all have the same diameter.

By shooting a few number of parcels on the airfoil, their trajectories can be easily followed to check which parcels are rebounding. As it can be seen in Fig. 4.23 all impinging parcels, whose trajectories are drawn in yellow, are bounced away from the surface. The droplet impacting close to the stagnation point re-impinges right away and there it sticks. Some other droplets rebound and are taken away by the flow, while the great majority of them, with black trajectories, do not even impact. In conclusion, if clouds with low MVD are considered for simulations, the percentage of rebounding parcels is too hight with respect to the reality, thus results obtained enabling the droplet rebound model are very different from those obtained with the basic stick model and from the experimental data. This aspect will be further

investigated in Sec. 4.5.2.

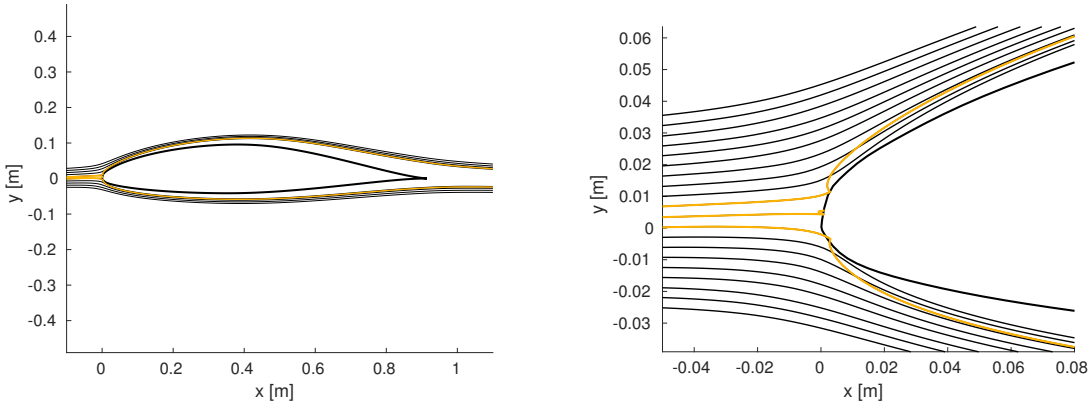

(a) (b)

Figure 4.23: Parcel trajectories for the NACA 65_2-415 case with $d_p = 11.5\ \mu m$. In black non-impinging parcels, in yellow bouncing parcels.

Splash

As regards the splashing model, its effect can be seen only for parcels with an impact energy above a certain threshold, depending on both the surface roughness and the parcel diameter as it has been illustrated in Fig. 4.16. Moreover, the fulfilment of the splashing condition Eq. 4.18 occurs at higher impact velocities as the parcel diameter is decreased. Thus, for a small parcel it is more difficult to splash compared to a big parcel, as it is shown by the obtained results in Fig. 4.24.

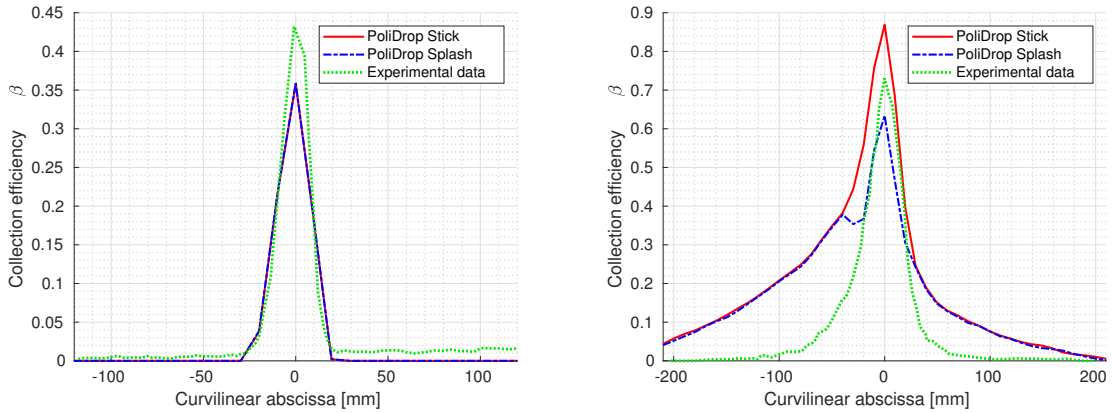

(a) NACA 65_2-415, MVD = 11.5 μm (b) NACA 65_2-415, MVD = 92.0 μm

Figure 4.24: Collection efficiency as a function of the curvilinear abscissa: comparison between splash model, stick model and experimental data for $\alpha = 0$ and different particles dimension.

In this case small parcels never splash and thus the results obtained enabling the splashing model are perfectly superimposed to those obtained with the stick model only (Fig. 4.24(a)). The influence of the new model introduced can be seen with parcels with a diameter of 92 μm (Fig. 4.24(b)). In this case, the effect is that of reducing the collection efficiency peak with respect to the stick model. This reduction is in accordance with experimental data.

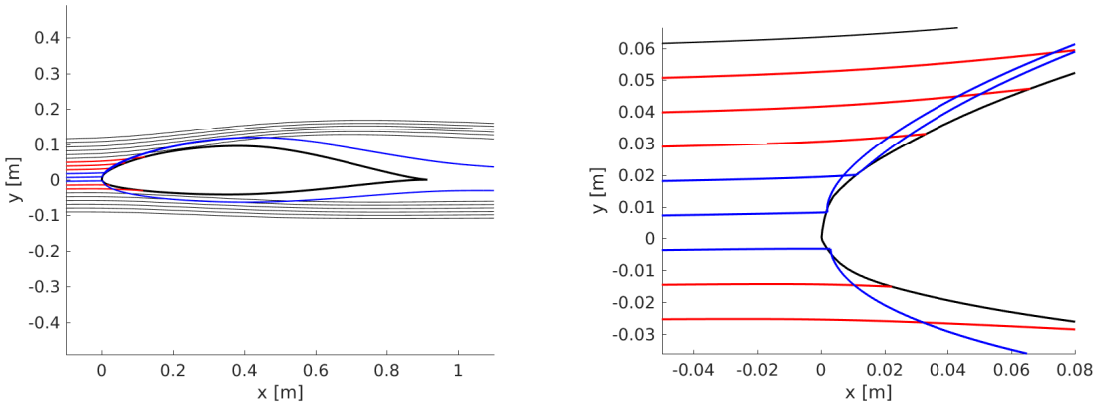

Figure 4.25: Parcel trajectories for the NACA 65_2-415 case with $d_p = 92.0\ \mu m$. In black non-impinging parcels, in red sticking parcel and in blue splashing parcels.

In Fig. 4.25 particle trajectories are represented. Black trajectories are related to non impinging parcels, red ones to sticking parcels and blue ones to splashing parcels (and their relative secondary fragments). As regards these fragments it must be underlined that they are much smaller than the original droplets as it is displayed in Fig. 4.26, where red parcels are the original cloud parcels with $d_p = 92.0\ \mu m$, orange represents the mass that remains on the surface with an equivalent diameter of 81.4 - 83.6 μm and blue particles are small secondary splashed fragments with d_p = 15.4 - 16.6 μm, as there are nearly 50 fragments for each impinging droplet. The small droplet fragments generated by the splashing process have low inertia and for them it is easier to follow streamlines. Therefore, it is unlikely that they re-impinge on the surface after the first impact and they are carried away by the flow. In particular, Fig. 4.25(a) shows how blue trajectories, which follow flow streamlines, close behind the airfoil trailing edge. This effect must be taken into account if another body is placed downstream of the airfoil. For example, splashed droplet fragments generated by the impact on the leading edge of the wing may potentially result in re-impingement on aircraft lift and control surfaces located downstream of actively protected regions [49], leading to an unexpected ice accretion.

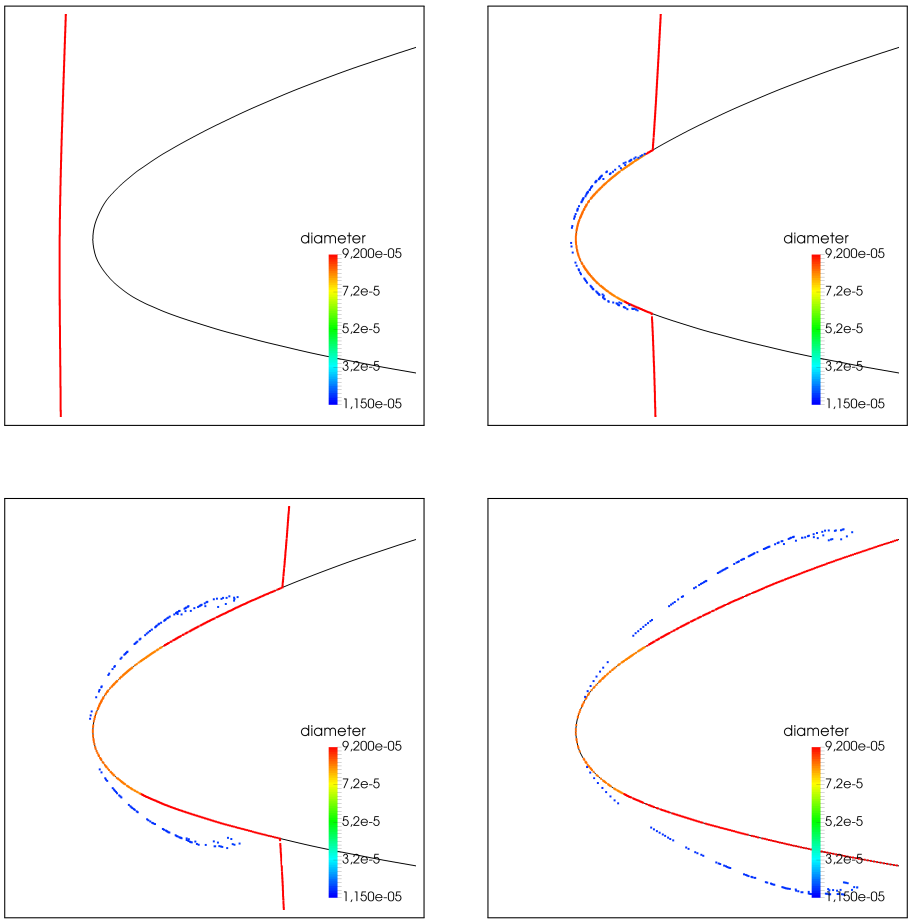

Figure 4.26: Visualisation of splashing parcels with $d_p = 92.0\ \mu m$ on the leading edge of a NACA 65_2-415 airfoil. Colours represent the diameter of the parcels. Red: original cloud parcels, $d_p = 92.0\ \mu m$. Orange: mass stuck on the surface, $d_p = 81.4$ - $83.6\ \mu m$. Blue: secondary fragments $d_p = 15.4$ - $16.6\ \mu m$.

Another aspect to be considered when dealing with splashing is the effect of the wall roughness. In fact, a variation of the roughness amplitude changes the lower threshold for splashing, affecting the parcel behaviour. The value of surface roughness is thus modified to study the effect of surface roughness on the collection efficiency (Fig. 4.27). For $R_a = 0$ there are no splashing parcels as the condition $Kc > \infty$ is never satisfied and the solution computed with the stick model is recovered. Then, as R_a is increased, the number of splashing droplets increases since the condition to be satisfied is less restrictive. For parcels with $d_i = 11.5\ \mu m$ there is no effect of the surface roughness as the splashing condition is never satisfied, even considerably increasing R_a. As expected, an increase of R_a, results instead in a greater number of splashing droplets in the case of bigger parcels.

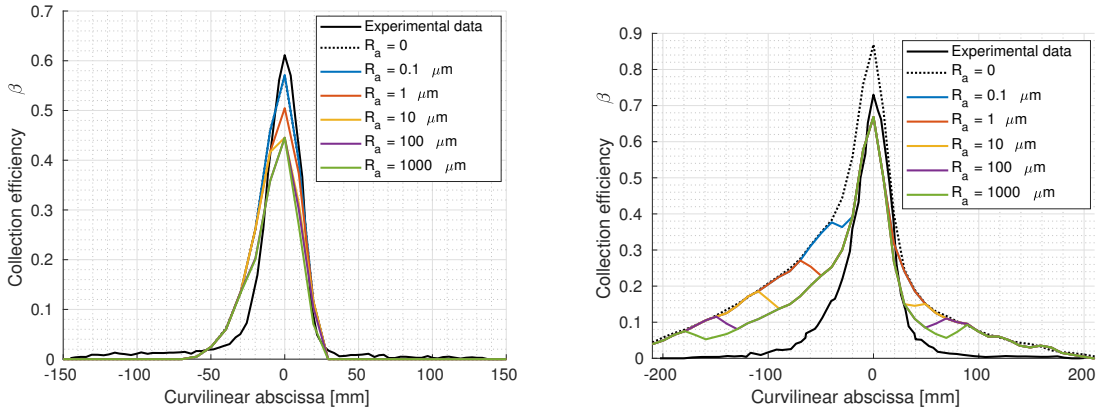

(a) NACA 65_2-415, MVD = 21.0 μm

(b) NACA 65_2-415, MVD = 92.0 μm

Figure 4.27: Effect of the surface roughness amplitude R_a on the collection efficiency for a NACA 65_2-415 airfoil with (a) $d_p = 21.0\ \mu m$, (b) $d_p = 92.0\ \mu m$.

For parcels with $d_i = 21.0\ \mu m$ the number of droplets splashing close to the stagnation point increases as the the surface roughness increases, leading to a reduction of the collection efficiency peak, which moves away from experimental data (Fig. 4.27(a)). In Fig. 4.27(b) the same study is performed for parcels with $d_i = 92.0\ \mu m$. In this case, the number of splashing droplets in proximity of the peak is not modified, as the splashing condition is always satisfied. However, droplets close to the impingement limits are more likely to splash. The collection efficiency is lowered and it approaches the experimental data. This effect is enhanced increasing the surface roughness, with the green curve in Fig. 4.27(b) showing a closer match with the experimental data with respect to the original black dotted one. However, it has to be taken into account that the green curve is obtained with a roughness value of 1 mm which is not acceptable if a traditional aeronautical surface is considered (i.e. aluminium alloy).

Complete model

The complete model is finally analysed and simulations are carried out enabling both the rebound and the splashing models, together with the basic stick condition. In this approach, when a droplet impinges on the surface its Weber number and Cossali parameter are both computed and compared with conditions 4.13 and 4.18. If the first one is satisfied, then the parcel is rebounded off the surface, otherwise if the second one is satisfied the parcel is splashed. If none of them is satisfied, the parcel is considered to stick on the wall. Based on this model, the collection efficiency distribution is computed over a NACA 65_2 - 415 airfoil at $\alpha = 0$ deg and $\alpha = 4$ deg and for a MS(1)-317 airfoil at $\alpha = 0$ deg with droplets of different dimensions and results are compared with experimental data and against LEWICE results from Ref. [38] and [62].

Fig. 4.28 represents the collection efficiency obtained with the complete model by Honsek and Habashi [49]. The blue curve in the two pictures may be compared with Fig. 4.21 where only the rebound model is activated and with Fig. 4.24 where only the splash model is activated in order to understand how the two models contribute to the complete model. It is evident that splashing does not affect the collection efficiency for small droplets and the peak reduction is completely due to the rebound model. As far as big droplets are concerned, the two models combine to give the peak reduction due to splash, and the zero collection efficiency close to the impinging limits due to rebound.

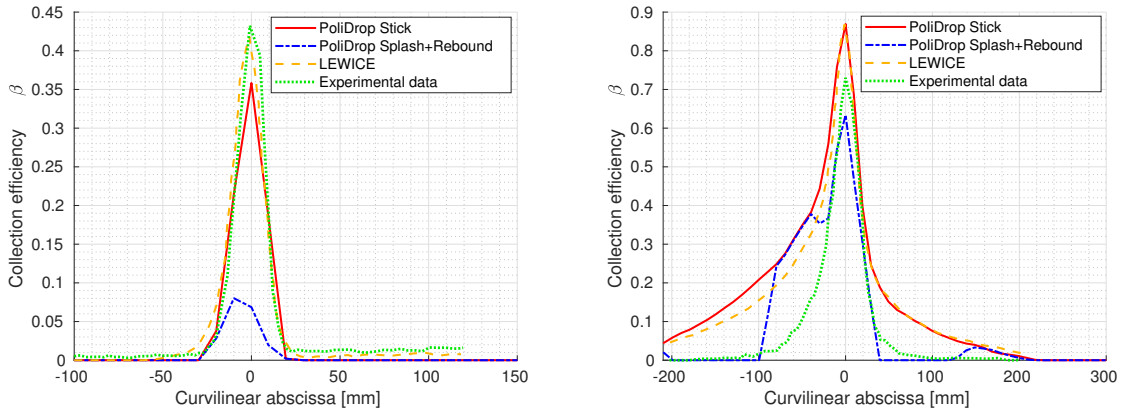

(a) NACA 65_2-415, MVD = 11.5 μm

(b) NACA 65_2-415, MVD = 92.0 μm

Figure 4.28: Collection efficiency as a function of the curvilinear abscissa: comparison of the complete rebound+splash model with experimental data for a NACA 65_2-415 airfoil at $\alpha = 0$ deg.

The same kind of comparisons and considerations can be done increasing the angle of attack from 0 deg to 4 deg. With a positive incidence, a greater number of parcels impinges on the lower side of the airfoil with respect to the upper side and the collection efficiency takes an asymmetric trend. Consequently, impingement limits are much wider on the lower side (positive curvilinear abscissa), in particular, for big droplets with $d_i = 79$ and 137 μm. Looking at results in Fig. 4.29, the same considerations made before may be repeated. Bouncing parcels lead to an abrupt reduction of the collection efficiency near impingement limits for big parcels, while rebound has a detrimental effect on the computed results for small parcels. Splashing instead has no effect on small parcels, but it reduces the peak for big parcels.

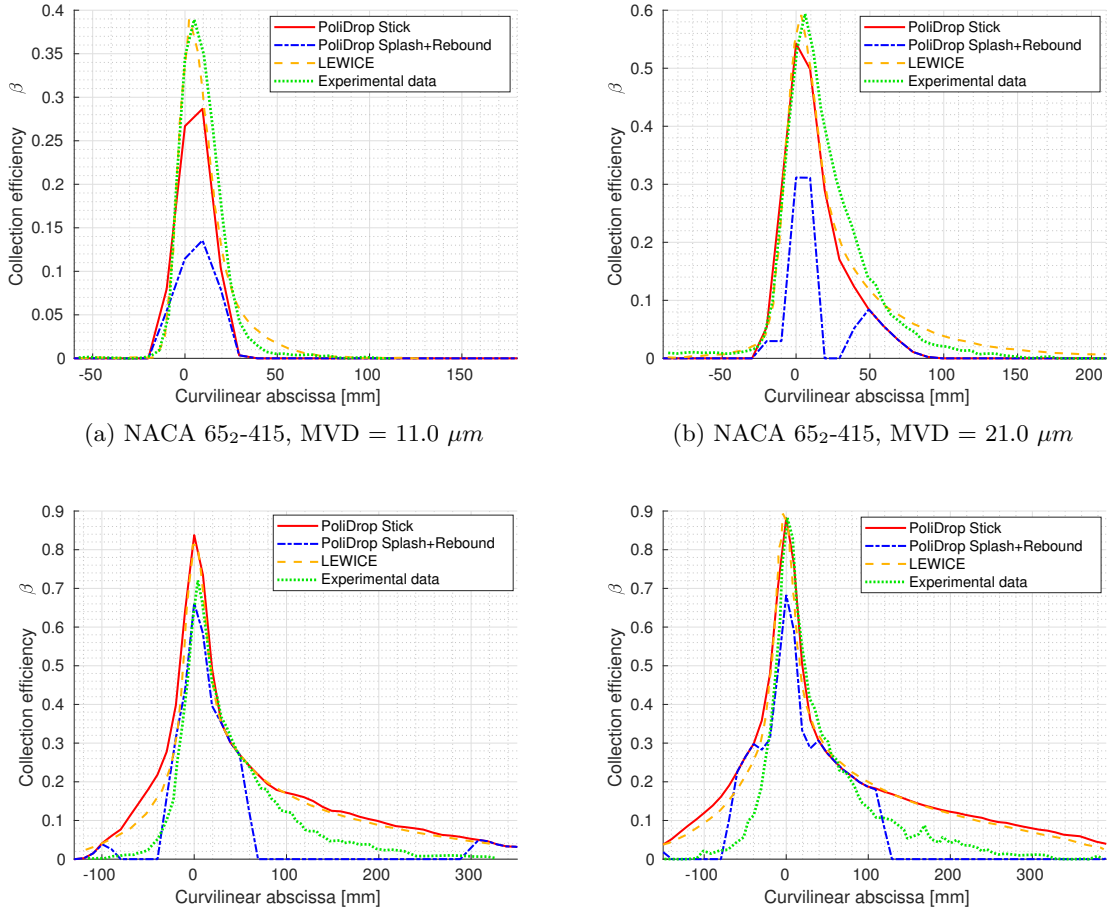

(a) NACA 65_2-415, MVD = 11.0 μm

(b) NACA 65_2-415, MVD = 21.0 μm

(c) NACA 65_2-415, MVD = 79.0 μm

(d) NACA 65_2-415, MVD = 137.0 μm

Figure 4.29: Collection efficiency as a function of the curvilinear abscissa: comparison of the complete rebound+splash model with experimental data for a NACA 65_2-415 airfoil at $\alpha = 4$ deg.

To better understand the model behaviour it is worthwhile to perform a further comparison on a MS(1)-317 airfoil, for which experimental data are available for a more complete range of parcels diameters. Besides, this case allows to clearly identify the different regions corresponding to the four droplet-wall interaction types. Fig. 4.30 shows the obtained results for the MS(1)-317 airfoil. Looking at the blue curve in pictures (c), (d), (e) and (f) it is evident that the splash model lowers the collection efficiency peak in proximity of the stagnation point, especially for $d_i = 79, 94, 137\ \mu m$. For $d_i = 168\ \mu m$ instead the peak computed with the new model is too low. Away from the peak region, moving towards the impingement limits, there are two regions where the blue curve joins the red curve. These are the regions where impinging parcels spread on the surface, because their energy is too low to splash and too high to rebound.

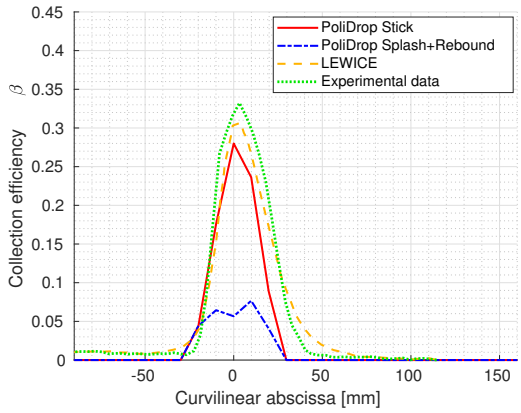

(a) MS(1)-317, MVD = 11.5 μm

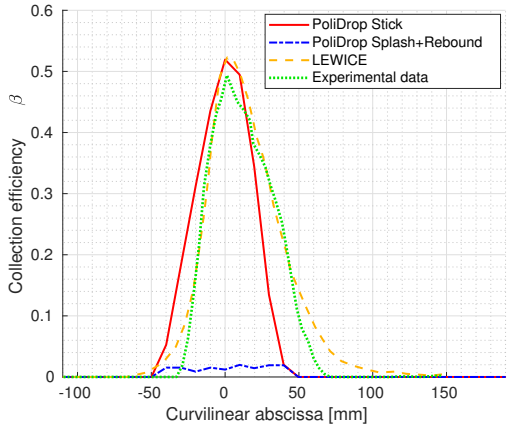

(b) MS(1)-317, MVD = 21.0 μm

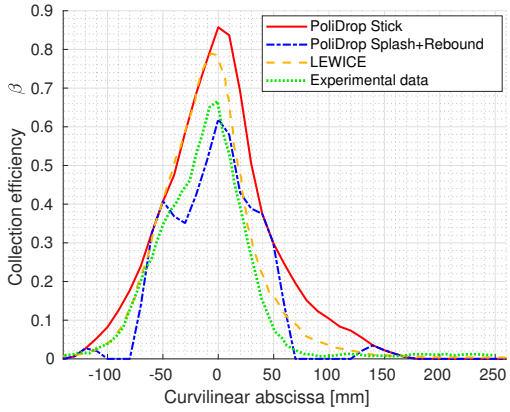

(c) MS(1)-317, MVD = 79.0 μm

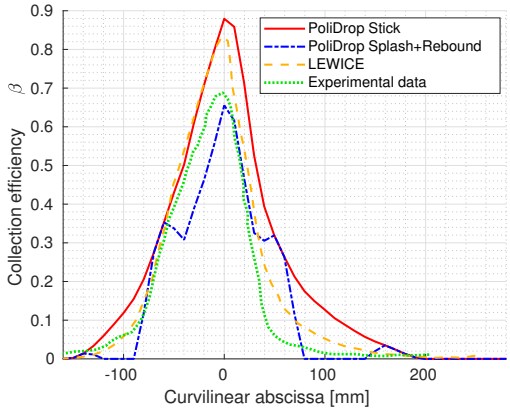

(d) MS(1)-317, MVD = 94.0 μm

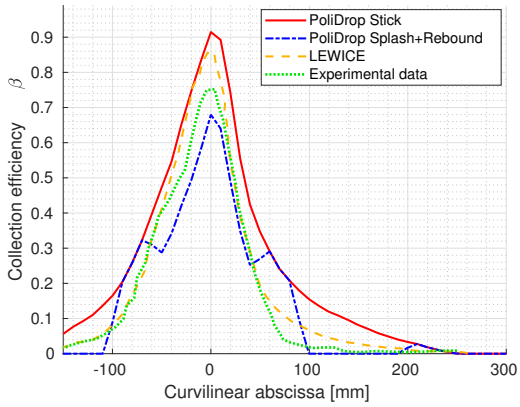

(e) MS(1)-317, MVD = 137.0 μm

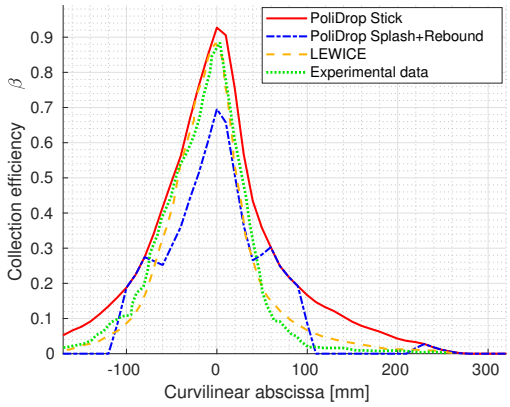

(f) MS(1)-317, MVD = 168.0 μm

Figure 4.30: Collection efficiency as a function of the curvilinear abscissa: comparison of the complete rebound+splash model with experimental data for a MS(1)-317 airfoil at $\alpha = 0$ deg.

Then, moving further away from the stagnation point the impact energy is even decreased, as the angle between the impact velocity and the normal to the panel increases. In this region the impact Weber number takes a range of values which satisfies the rebound condition and therefore parcels are bounced off the surface. Accordingly, the collection efficiency drops to zero. Downstream of this area where no water is collected on the surface, there are few parcels sticking as their impact energy is very low. The collection efficiency distribution obtained with the complete model in case of big droplets shows a good agreement with experimental data. Both the peak and impingement limits are estimated with good precision, but the collection efficiency curve is highly irregular due to the sharp transition between different models. Fig. 4.30(a) and (b) instead show a huge discrepancy between numerical results and experimental data, which requires a deeper analysis of the rebound model. The rebound condition is based on a critical range of the Weber number We_s, which depends on both the parcel diameter and the impinging velocity normal to the panel. Hence, rebound can occur in two different conditions: huge droplets with low impact velocity and small droplets with high impact velocity. These two cases have been already analysed in Fig. 4.22. If big parcels are considered, rebound leads to a reduction of the collection efficiency in proximity of the impingement limits which brings numerical and experimental results closer. In the case of small diameter, instead, all the droplets impinging near to the leading edge bounce away from the surface, causing an important reduction of the collection efficiency which is not physical. For these reasons an improvement of the current wall-interaction model proposed in [49] is deemed necessary.

4.5.2 Modified splashing model

The first issue to deal with is the behaviour of the rebound model when a cloud of small droplets is considered. In this respect, it is of fundamental importance to discern between deep pool and shallow pool impact, on the basis of the value of the value of the dimensionless water film thickness $H = h/d_p$. If $H \gg 1$ it means that the water layer thickness is much greater than the droplet diameter and the impact is considered a deep pool impact. The drop triggers an unconstrained liquid motion and it is capable of pushing apart a significant liquid mass under the impact site. As a result, an almost hemispherical crater appears initially below the unperturbed surface. This crater is usually surrounded by a rather thick rim of liquid, referred to as a corona or crown, characterised by a transitory expansion. Indeed, at a certain crater size, the surface tension arrests the downward motion of the liquid and both the crater and the crown collapse. Depending on the impact energy, the collapse may induce ejection of a Worthington jet in the middle of the crater or restore the plane free surface after several oscillations due to the competition of the surface tension and inertia (Fig. 4.31). If instead the water layer thickness is comparable to the droplet diameter ($H \sim 1$) a shallow pool impact occurs. When the droplet impinges on the liquid, the water displacement below the impact position is constrained by the

wall. Thus, if the impact has enough energy, the displaced water rises above the free surface forming a crown and in practice the droplet impacts on a dry surface.

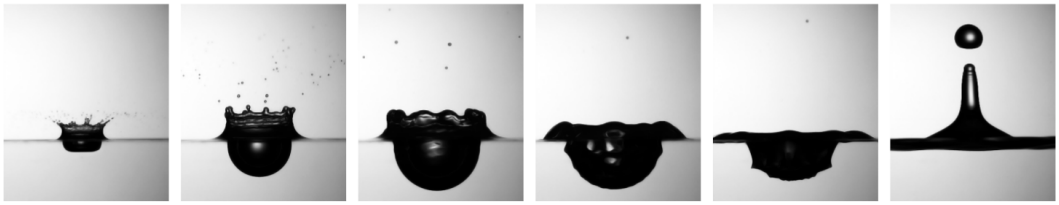

Figure 4.31: Water drop impact on a deep pool, from crater and corona formation to the ejection of a Worthington jet. Ref. [63].

In the PoliMIce framework the water film thickness is assumed to be constant and equal to 100 μm. Therefore the impact on the liquid film is a deep pool impact for small parcels ($H > 5$ according to Macklin and Metaxas [64]) and a shallow pool impact for big parcels ($H < 2$). However, the rebound model by Bai and Gosman [53] is based on equations for impact on a solid surface. This model is indeed acceptable for the shallow pool impact of big droplets, as they move away the water below them before impinging on the surface, but it is not suitable for modelling deep pool impacts. In practice, small parcels impinging on the film cannot bounce off the surface as they merge with the surrounding water. For this reason results obtained with the implemented rebound model are considerably different from experimental data. In order to fix this issue an additional rebound condition should be added, to set the lower limit diameter for bouncing. For example, rebound may be allowed only for SLD with a diameter greater then 50 μm, so that $H < 2$. However, this is not the chosen solution. The strategy adopted in this work is that of completely switching off the rebound model and considering bouncing as a special case of splashing, when only one secondary droplet is formed and no water is left on the wall. This choice is consistent with the scientific literature concerning the wall interaction problem. Indeed, most authors [50, 55, 57] identify only two characteristics flow patterns on the surface: deposition and splashing. Upon impact the drop spreads over the surface taking the shape of a lamella and at sufficiently low impact velocity it is deposited on the wall. By contrast, at higher impact velocities the lamella takes the shape of a crown with an unstable rim from which small secondary droplet fragments are ejected (splashing process). This classification is valid if the film thickness is sufficiently large with respect to the mean surface roughness and indeed this is the case. In fact, the water layer thickness is equal to 100 μm, while the roughness amplitude is in the range 0.1-1 μm for a smooth surface. In this thin liquid film regime characterised by $H \gg R$ the surface morphology is not expected to influence significantly the splash. Therefore, according to Cossali [57], the splashing condition in Eq. 4.18 may be replaced with the following one:

$$K_c \geq 2100 + 5880 H^{1.44} \tag{4.27}$$

where K_c is once again the Cossali parameter and H the dimensionless film thickness. In this way, the dependency on the surface roughness is overcome. Moreover, a splashing conditions for impacts on dry surfaces can be recovered setting $H = 0$. Therefore, when running ice accretion simulations it is necessary first to evaluate which one between rime ice or glaze ice mostly accretes over the surface and then to set the proper splashing condition imposing the correct value of H manually. In order to automate this process, it would be necessary to couple PoliDrop with PoliMIce so as to have the correct value of the dimensionless film thickness for each cell. This coupling, together with the computation of the actual value of the liquid layer thickness h and with the evaluation of the ice roughness, would allow a better modelling of the splashing threshold for different conditions. By the way, this coupling is out of the scope of the present thesis, as condition 4.27 already allows to obtain a good accordance with experimental data.

This new condition lowers the threshold for splashing but it does not fix the collection efficiency curve irregularity due to the sharp transition between splashing and deposition. Moreover, the computed curve remains much higher than experimental data close to the impingement limits, as it was shown in Fig. 4.24 (b). In this regard, a further modification of the splashing condition is proposed, in the light of physical considerations made by Trontin and Villedieu [65]. According to them, two splashing regimes may be clearly distinguished as far as SLD are concerned. These regimes are identified by a critical value of the incidence angle ξ, defined as the complimentary to the impact angle φ_i (Eq. 4.16). If the droplet speed is fixed, an increase of ξ, corresponding to a decrease of φ_i, leads to a higher normal component of the impact velocity. Hence, for high values of ξ the splashing outcome does not strongly depend on the absolute value of the impact angle. Instead, in this case the fundamental parameter governing the splash phenomenon is the Cossali parameter K_c, as a measure of the impact energy. The higher is K_c, the more droplets splash, the lower is the collection efficiency. Thus, since for small angles of incidence the normal component of the impinging velocity is low, splashing cannot be triggered by the impact energy. In the model proposed in Sec. 4.4.2 these droplets with low normal impact velocity are considered to stick on the surface and this leads to high values of the collection efficiency close to the impingement limits. What actually occurs in this case is that the droplet does not spread much on the surface and a part of the parcel results not to be attached to the wall during the impact process. Hence, the tangential kinetic energy is not efficiently dissipated by the viscous forces and the liquid droplet may partially or completely bounce off the wall. For this reason in this regime the governing splashing parameter is the incidence angle ξ. Therefore, splashing occurs if at least one of the following conditions is satisfied:

$$K_c \geq 2100 + 5880H^{1.44} \text{ or } \xi \leq \xi_c \tag{4.28}$$

where ξ_c is the critical angle of incidence which must be defined. It is experimental

evidence that the smallest droplets always stick to the wall after impact, even for small angles of incidence. To account for that, ξ_c cannot assume a constant value but it must decrease as the droplet diameter decreases, so as to lower the upper threshold for splashing. Since the impact velocity is found to be smaller for small droplets than for large droplets, the capillary number Ca

$$Ca = \frac{\mu_d u_{n,i}}{\sigma} \tag{4.29}$$

is used to model ξ_c as:

$$\xi_c = \xi_0 tanh\left(\frac{Ca}{Ca_0}\right) \tag{4.30}$$

In this way, for very small capillary numbers, ξ_c tends to zero and splashing is inhibited, while for large capillary number it reaches the asymptotic value denoted by ξ_0, as it is shown in Fig. 4.32. Note that ξ_0 and Ca_0 are two adjustable parameters to be identified on the basis of experimental data and here set respectively to $\frac{\pi}{4}$ and 0.2 (Ref. [65]).

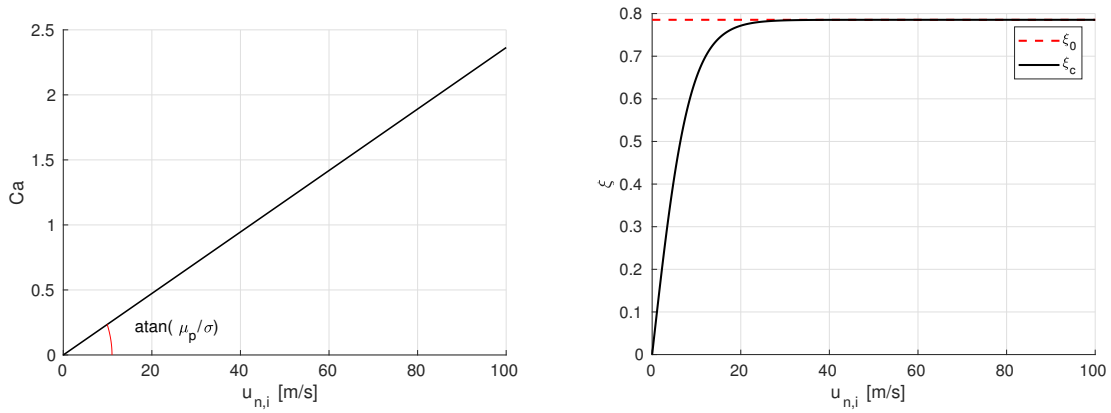

(a) (b)

Figure 4.32: Splashing parameters trend as a function of the normal impact velocity $u_{n,i}$. (a) Capillary number Ca, (b) critical incidence angle ξ_c.

Eventually, another aspect has to be considered. In Sec. 4.4.2, the splashing model was introduced and its parameters were analysed. In particular, in Fig. 4.17(b) and 4.18, the mass loss coefficient Φ and the number of secondary droplets N_s have been represented as functions of the normal impact velocity varying the droplet diameter. It has also been said that for physical reasons their values are bounded:

$$0 \leq \Phi \leq 1 \tag{4.31}$$

$$N_s \geq 0 \tag{4.32}$$

but Eq. 4.21 and 4.22 may give values out of these boundaries. This occurrence is avoided if the original splashing condition Eq. 4.18 is retained. However, as it has been replaced with 4.28, the limits 4.31 and 4.32 must be imposed on the values of Φ and N_s as it is shown in Fig. 4.33.

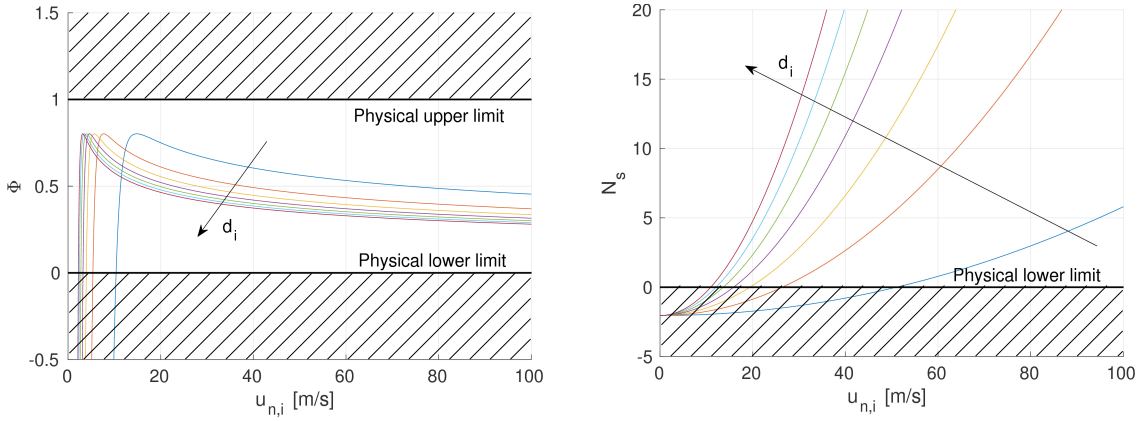

(a) (b)

Figure 4.33: Splashing parameters trend as a function of the normal impact velocity $u_{n,i}$ and impinging particle diameter d_i varying from 10 μm to 130 μm. Representation of the physical limits. (a) Mass loss coefficient Φ, (b) number of secondary droplet fragments N_s.

This modified splashing model is implemented in PoliDrop and tested on different cases and results are presented in Sec. 4.5.3.

4.5.3 Results and discussion

PoliDrop simulations with the modified splashing are carried out on a NACA 65_2-415 airfoil at $\alpha = 0$ deg and $\alpha = 4$ deg and for a MS(1)-317 airfoil at $\alpha = 0$ deg changing the dimension of the droplets. The same cases considered for the complete Honsek-Habashi model presented in Sec. 4.5.1 are analysed, in order to assess the improvement of the modified splashing model through comparison both with experimental data and results obtained with the original model.

Fig. 4.34 and 4.35 show the results obtained with the modified splashing model for the NACA 65_2-415 airfoil. Comparing them with Fig. 4.28 and 4.29 it leaps out that the achieved improvement is remarkable. Collection efficiency peak and impingement limits are more accurately identified, both in the $\alpha = 0$ and $\alpha = 4$ deg cases. Moreover, the collection efficiency curves show a smooth trend.

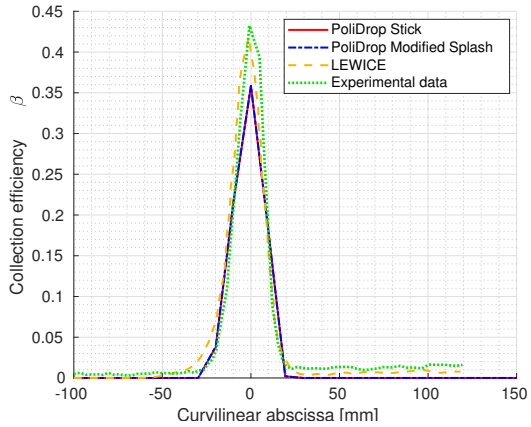

(a) NACA 65_2-415, MVD = 11.5 μm

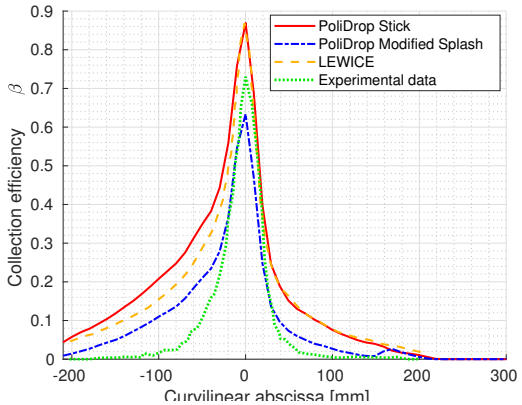

(b) NACA 65_2-415, MVD = 92.0 μm

Figure 4.34: Collection efficiency as a function of the curvilinear abscissa: comparison of the modified splashing model with experimental data for a NACA 65_2-415 airfoil at $\alpha = 0$ deg.

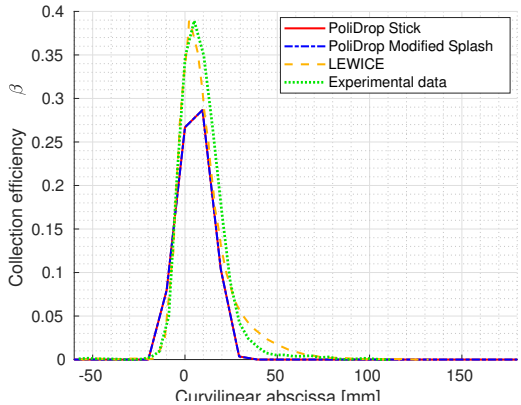

(a) NACA 65_2-415, MVD = 11.0 μm

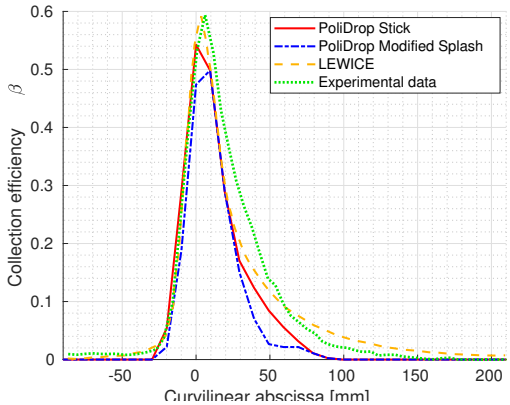

(b) NACA 65_2-415, MVD = 21.0 μm

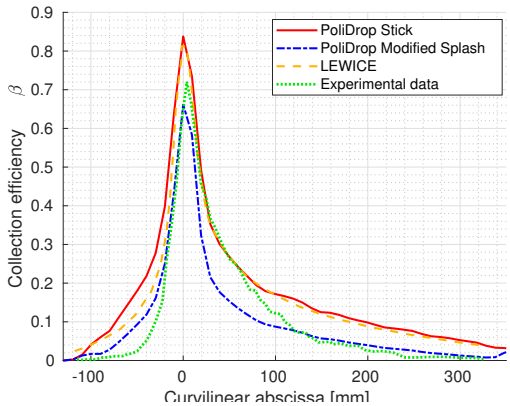

(c) NACA 65_2-415, MVD = 79.0 μm

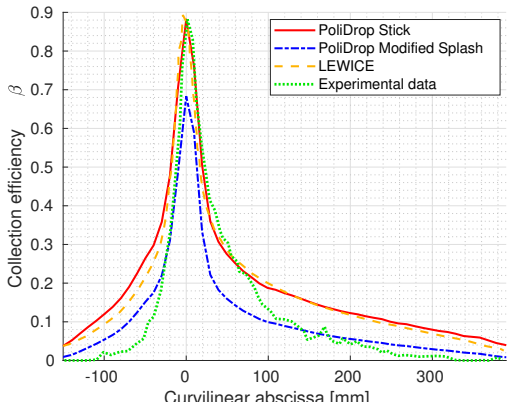

(d) NACA 65_2-415, MVD = 137.0 μm

Figure 4.35: Collection efficiency as a function of the curvilinear abscissa: comparison of the modified splashing model with experimental data for a NACA 65_2-415 airfoil at $\alpha = 4$ deg.

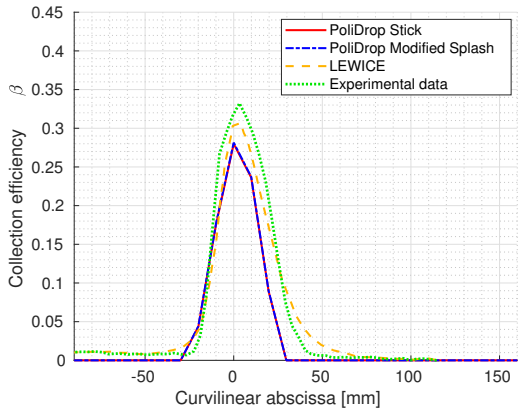

(a) MS(1)-317, MVD = 11.5 μm

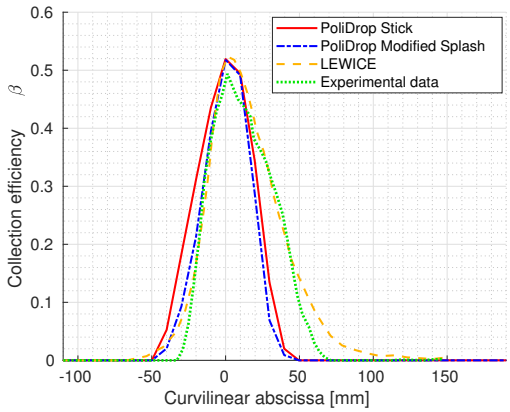

(b) MS(1)-317, MVD = 21.0 μm

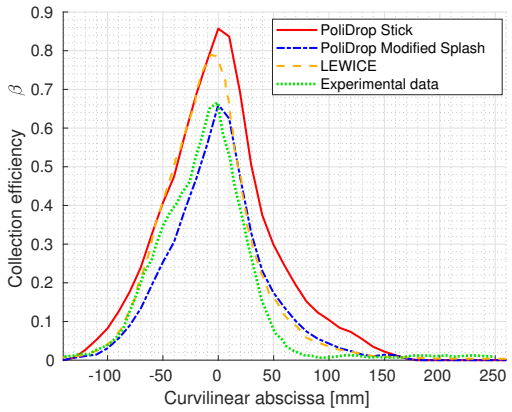

(c) MS(1)-317, MVD = 79.0 μm

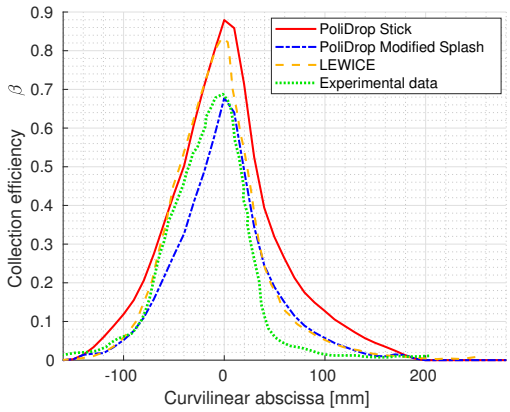

(d) MS(1)-317, MVD = 94.0 μm

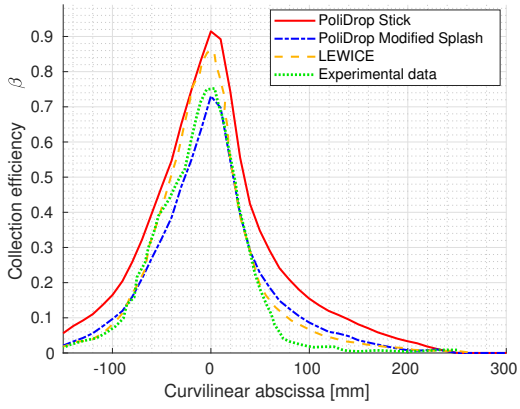

(e) MS(1)-317, MVD = 137.0 μm

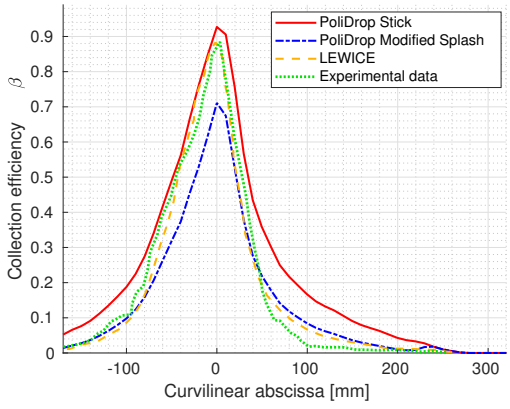

(f) MS(1)-317, MVD = 168.0 μm

Figure 4.36: Collection efficiency as a function of the curvilinear abscissa: comparison of the modified splashing model with experimental data for a MS(1)-317 airfoil at $\alpha = 0$ deg.

The same improvement is observed for the MS(1)-317 airfoil at zero angle of attack. Results obtained with the modified splashing model are shown in Fig. 4.36. and the new collection efficiency curve should be compared with Fig. 4.30 to perceive the enhanced accuracy introduced by the modified splashing model with respect to the complete Honsek-Habashi model. The first thing that stands out is the accuracy of the model as far as small droplets are concerned in (a) and (b). In this case the collection efficiency is practically unaffected with respect to the basic stick model and the accordance with experimental data is preserved. As regards bigger droplets the modified splashing model smooths the collection efficiency curve obtained with the complete Honsek-Habashi model. Indeed, the sharp transition between different types of droplet-wall interactions is overcome by switching off the rebound model and modifying the splashing condition. The new splashing condition also brings the computed collection efficiency closer to experimental data in proximity of the impingement limits and lowers the peak. As it is shown in Fig. 4.30(f), for MVD = 168.0 μm the collection efficiency is underestimated in proximity of the stagnation point as the computed value of the peak is too low. In conclusion it can be stated that the introduced splashing model leads to a significant improvement in the collection efficiency computations for SLD with diameters in the range between 50 and 150 μm, which was the purpose of the present work.

For the sake of completeness, ice shapes are computed for three exemplary test cases chosen among the ones examined for the computation of the collection efficiency. Since no experimental ice shapes are available for the considered test cases, the accuracy of the splashing model cannot be evaluated on the resulting ice shapes. By the way, the model accuracy has already been evaluated in terms of collection efficiency in Fig. 4.34, 4.35 and 4.36 and it may be expected that the introduced improvements for the impingement computation reflect also on the corresponding ice shape. Hence, the purpose of the following simulations is to evaluate the effect of the modified collection efficiency on ice accretion. For ice accretion simulations the computational grids are refined in order to have a better resolution of the body surface which allows a more accurate estimation of the ice shape. Simulations are carried out on meshes made of 205734 elements and 132076 nodes for the NACA airfoil and 215622 elements and 137361 nodes for the MS airfoil. Complete PoliMIce simulations are performed updating the CFD and the particle trajectories every 10 s until the total exposure time (t_{exp} = 300 s) is reached. Both the original stick model and the modified splashing model are used and results are compared in Fig. 4.37, 4.38 and 4.39. Simulations parameters for the three different test case are summarised in Tab. 4.3. Flight conditions are unchanged with respect to the performed PoliDrop simulations (see Sec. 3.3), while atmospheric conditions are selected on the basis of Fig. 4.1(a), where environmental conditions for freezing drizzle are showed in terms of temperature and LWC. These low values of the LWC lead to a small maximum thickness of the ice layer (5-20 mm). Moreover, the resulting ice shapes are smooth and streamlined. This is due to fact that, even if big droplets are

used for the simulations, the LWC and airspeed are low and thus rime ice accretes on the surface. This is already evident from PoliMIce simulations with the stick model. Consequently, simulations with the modified droplet-wall interaction model are performed using the splashing condition Eq. 4.27 with a null value of the liquid layer thickness ($H = 0$).

	Case 1	**Case 2**	**Case 3**
Airfoil	NACA 65_2-415	NACA 65_2-415	MS(1)-317
Chord	0.9144 m	0.9144 m	0.9144 m
$\mathbf{V_\infty}$	78.68 m/s	78.68 m/s	78.68 m/s
α	0 deg	4 deg	0 deg
$\mathbf{d_p}$	92 μm	$d_p = 79$ μm	137 μm
$\mathbf{T_\infty}$	265 K	260 K	255 K
$\mathbf{P_\infty}$	10^5 Pa	10^5 Pa	10^5 Pa
LWC	0.25 g/m^3	0.20 g/m^3	0.15 g/m^3
$\mathbf{t_{exp}}$	300 s	300 s	300 s
$\mathbf{\Delta t}$	10 s	10 s	10 s
Model	Ref. [22]	Ref. [22]	Ref. [22]
Type of ice	Rime	Rime	Rime
β **ref.**	Fig. 4.34(b)	Fig. 4.35(c)	Fig. 4.36(e)

Table 4.3: Ice accretion parameters for the assessment of the wall interaction model (Cases 1-2-3).

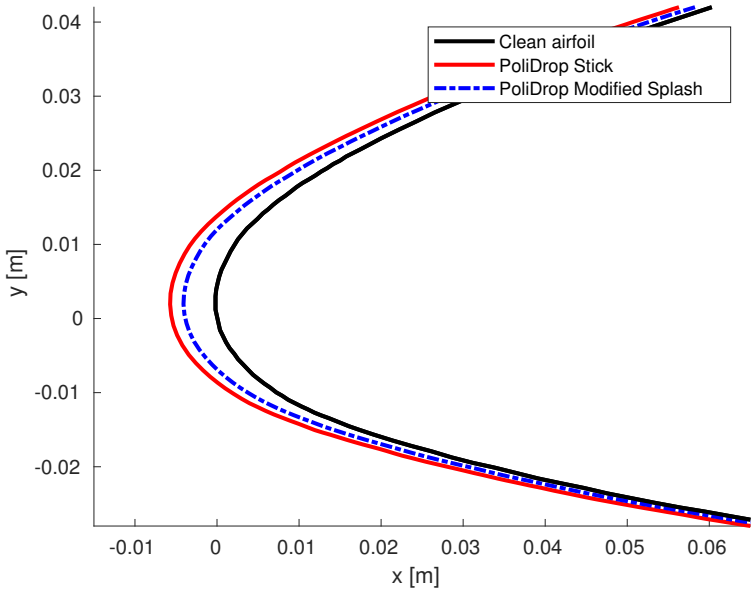

Figure 4.37: Ice accretion over a NACA 65_2-415 airfoil at $\alpha = 0$ deg with cloud MVD = 92 μm. Comparison between stick and modified splashing models for $t = 300$ s (Case 1).

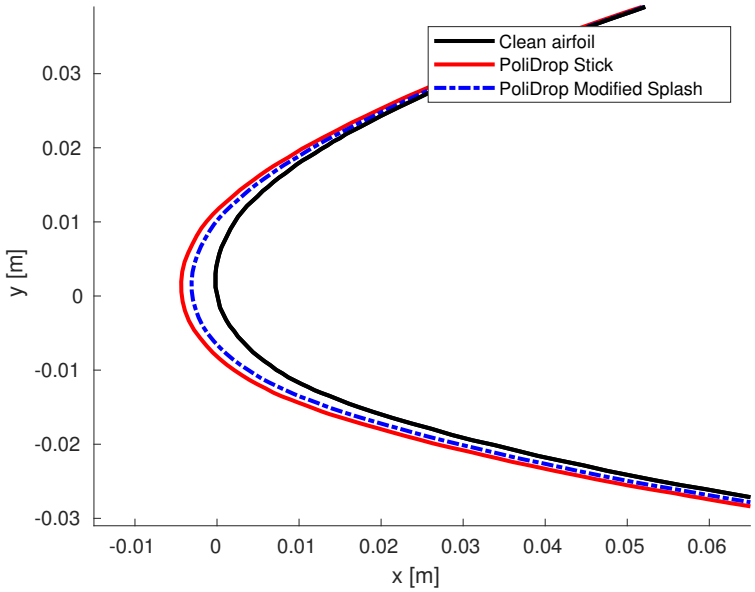

Figure 4.38: Ice accretion over a NACA 65_2-415 airfoil at $\alpha = 4$ deg with cloud MVD = 79 μm. Comparison between stick and modified splashing models for $t = 300$ s (Case 2).

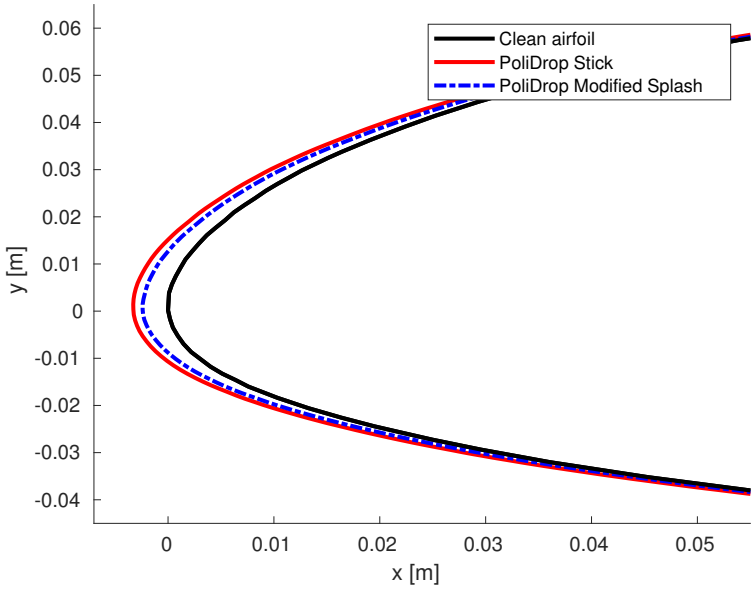

Figure 4.39: Ice accretion over a MS(1)-317 airfoil at $\alpha = 0$ deg with cloud MVD = 137 μm. Comparison between stick and modified splashing models for $t = 300$ s (Case 3).

It can also be observed that for $\alpha = 0$ deg (Fig. 4.37 and 4.39) the computed ice thickness shows a nearly symmetric shape. The slight skewness is due to the fact that the airfoils are non-symmetric, which makes a greater number of particles impinge on the upper surface, as it is shown by the collection efficiency curves. On the contrary, when the angle of attack is increased to $\alpha = 4$ deg, the flow field asymmetry, makes a higher number of parcels impinge on the lower surface of the airfoil, resulting in higher impingement limits on the lower side and lower impingement limits on the upper side. Therefore, the obtained ice shape (Fig. 4.38) is characterised by higher thickness and higher extension on the lower side with respect to the upper surface.

As far as the comparison between the two different droplet-wall interaction models employed is concerned, it can be stated that the difference between ice shapes is in accordance with the collection efficiency results. It was said that, for big droplets, the modified splashing model brings the computed collection efficiency closer to experimental data in proximity of the impingement limits and lowers the peak. Hence, the collection efficiency curves obtained with the splashing model are lower than those obtained with the stick model, as it is shown in Fig. 4.34(b), 4.35(c) and 4.36(e). This fact reflects on the computed ice shapes. Indeed, the ice layer thickness computed with the splashing model (blue curves) is smaller than the ice shape obtained with the stick model (red curves). Another aspect to be considered is that the ice shape computed with the modified splashing model remains smooth and streamlined for the whole exposure time. Consequently, small secondary droplet fragments manage to follow streamlines and no re-impingements of splashed droplets occur.

Chapter 5

Super Hydrophobic Surfaces

Super Hydrophobic Surfaces (SHS) are solid surfaces characterised by particular chemical and structural properties which makes them highly hydrophobic. The interest towards these super hydrophobic surfaces have earned rapidly increasing interest since the discovery of the "lotus leaf effect" [66]. Indeed, in nature various plants and animals exhibit extreme hydrophobicity, making the deposition of water drops on their surface almost impossible. All these super hydrophobic biosurfaces share two common features: they are made of hydrophobic materials and they are characterised by various periodically or randomly distributed micro/nanostructures. During the last decade much effort has been devoted to design artificial solid surfaces with comparable water-repellent properties. The actual strategy consists in mimicking super hydrophobic biosurfaces by designing a rough substrate out of a hydrophobic material. Moreover, Zhang et al. [67] found that, in addition to the super hydrophobicity derived from special surface structure and chemical composition, these surfaces exhibit further structurally defined functionalities, such as self-cleaning properties and icephobicity.

These properties may be exploited to design passive anti-icing systems, taking advantage of the surface super hydrophobicity and icephobicity. Thanks to water repellency and high droplet mobility, liquid drops exhibit low adhesion on the super hydrophobic coatings. Thereby, a low amount of water is deposited on the body surface and water accumulation is eliminated before water can freeze. Antonini et al. [68] proved that this leads to a huge reduction of the energy needed to fully evaporate water deposited on the surface. The energy required to avoid ice accretion over the wing, not only in the heated area but also in the downstream region, can be reduced by up to 80%. Moreover, if ice manages to accrete on the SHS, ice adhesion forces are considerably lower than the corresponding forces on a smooth surface. Shear forces needed to remove ice from the structure are reduced, but this reduction is proved not to be sufficient to allow for natural ice release under the effect of gravity and aerodynamic forces (at least for non-rotating surfaces).

In this chapter the properties and the physical behaviour of SHS are described (Sec. 5.1) and the droplet impingement phenomenon on SHS is analysed and modelled based on experimental results (Sec. 5.2). Two SHS anti-icing systems are then implemented and simulations are carried out to study their effectiveness in different flight and atmospheric conditions (Sec. 5.3).

5.1 SHS physics

Wettability properties of a solid surface has been briefly described in Sec. 4.2. The contact angle θ has been defined as the angle between the liquid-solid interface and the line tangent to the liquid-vapour interface from the contact point. It can be derived balancing surface tensions acting at each interface:

$$cos\theta = \frac{\sigma_{sv} - \sigma_{sl}}{\sigma_{lv}} \tag{5.1}$$

where subscripts indicate the corresponding interfaces (solid-vapour, solid-liquid and liquid-vapour). The contact angle has been identified as the fundamental parameter determining the surface wettability, together with the advancing and receding contact angles, defined as the contact angles generated by the expansion and the contraction of the liquid drop. On the basis of the values assumed by the contact angles, multiple types of surfaces may be identified with different wettability properties. With reference to Fig. 4.3, if the contact angle θ assumes a value lower than 90 deg the surface is said to be hydrophilic, while if θ is higher than 90 deg the surface is said to be hydrophobic. Super hydrophobic surfaces, instead, are defined as surfaces with very high contact angles and low contact angle hysteresis $\Delta\theta$, defined as the difference between the advancing and the receding contact angle:

$$\begin{aligned} \theta_{adv} &> 150\ deg \\ \theta_{rec} &> 150\ deg \\ \Delta\theta &< 10\ deg \end{aligned} \tag{5.2}$$

Contact angle hysteresis provides an indication of drop mobility [69]: the lower is $\Delta\theta$, the easier is for the droplet to be displaced on the surface. Instead, a high contact angle means high hydrophobicity (i.e. water repellency), but contact angles greater than 120 deg cannot be obtained for a smooth surface [70]. In order to further increase the contact angles, the surface must have a suitable roughness, thus super hydrophobic surfaces are made of hydrophobic materials with and increased surface roughness. The topography of such surfaces can be defined by different roughness parameters but the commonly accepted roughness parameter when dealing with static and dynamic wetting properties is the Wenzel roughness r. It is defined as the ratio between the real surface area of the solid and its planar projected surface area

and so, by definition, $r > 1$. If the Wenzel roughness of a hydrophobic material is high enough, super hydrophobicity is expected. In practice, the detailed topography of the surface and the intrinsic wettability properties of the smooth material also play an important role. Depending on these parameters, a sessile drop statically deposited on a super hydrophobic surface may experience two different states: the Cassie-Baxter state and the Wenzel state (Fig. 5.1).

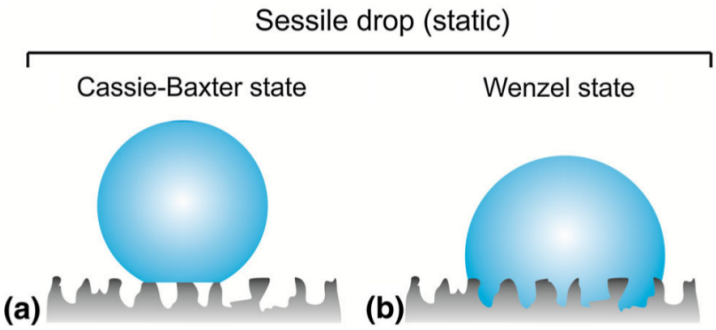

Figure 5.1: Cassie-Baxter and Wenzel states for a sessile droplet statically deposited on a SHS. Ref. [71].

In the Cassie-Baxter regime [72] the liquid droplet bridges across the tops of the roughness elements and it stays on a composite surface made of solid and vapour pockets. The presence of these pockets of gas trapped at the solid-liquid interface reduces the contact between the liquid and the solid substrate and leads to high repellency and high mobility of the water drop on the super hydrophobic surface. On the contrary, in the Wenzel regime [73] the liquid penetrates the surface grooves and wets the surface completely. The contact angles observed in these conditions are given respectively by Eq. 5.3 and Eq. 5.4.

$$cos\theta^{CB} = fcos\theta - (1 - f) \tag{5.3}$$

$$cos\theta^{W} = rcos\theta \tag{5.4}$$

where θ is the contact angle on the smooth surface, f is the fraction of area where the liquid is in direct contact with the surface and r is the Wenzel roughness parameter. The Cassie-Baxter and Wenzel equations are useful to predict the equilibrium contact angle on a rough surface, but multiple values of the contact angle may be observed when a drop is placed on a surface. The range of observable contact angles between θ_{adv} and θ_{rec} must be considered. In both cases the advancing contact angle is increased compared to the corresponding angle on the smooth surface, while only the Cassie-Baxter state allows very high receding contact angles which might induce droplet rebound. Antonini et al. [69] found that the receding contact angle is the key

wetting parameter controlling droplet rebound upon impact. On hydrophilic surfaces, which are characterised by receding contact angles lower than 90 deg, rebound does not occur and the drop remains stuck on the surface, on hydrophobic and super hydrophobic surfaces, instead, rebound is observed only on surfaces with a receding contact angle higher than 100 deg.

5.2 Droplet impingement on SHS

The dynamics of the impact phenomenon may alter surface wetting properties close to the impact point affecting drop rebound. Hence, care must be taken when using statically defined wetting parameters, such as advancing and receding contact angles, to predict the dynamic behaviour of a liquid drop on a solid surface. Indeed, the value of the measured contact angle strongly depends on the way the droplet is deposited on the surface [74]. When gently deposited on the patterned surfaces, the measured contact angles of the water drop agree with the value expected from the Cassie-Baxter relation. Impacting instead of depositing the drop could result in the transition from the Cassie-Baxter to the Wenzel regime, also referred to as impalement transition (Fig. 5.2).

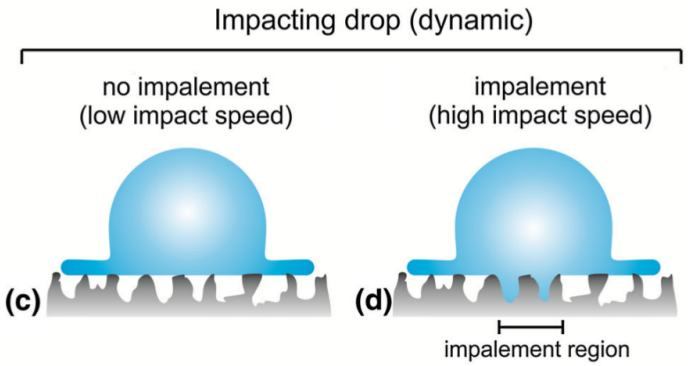

Figure 5.2: Impalement transition from Cassie-Baxter to Wenzel regime for a sessile droplet dynamically deposited on a SHS. Ref. [71].

Indeed, for low impact velocities the Cassie-Baxter state can be preserved, while for velocities higher than a critical value the liquid is forced to penetrate into the surface cavities in a region close to the impact zone, gas pockets are displaced and water fully wets the surface. As a result, the contact angle hysteresis increases and the receding contact angles might decrease to values lower than 90 deg. If this occurs, rebound is inhibited since water adhesion increases and the droplet remains stuck on the surface and cannot lift off (Fig. 5.2(d)).

Another aspect to be considered is the deposition-rebound limit. In fact, at very low Weber numbers, the parcel kinetic energy is not high enough to overcome the

dissipation energy during impact and the drop does not rebound. The minimum velocity V_{DR} allowing rebound to be observed is found to scale with the inverse of the square root of the droplet diameter [75]. The smaller the drop, the more it is likely to deposit on the surface.

$$V_{DR} = \sqrt{\frac{2\sigma}{\rho_p d_p}} \tag{5.5}$$

When a water droplet impinges on a super hydrophobic surface, three outcomes may be identified in dependency of the impact velocity and drop size:

- **Deposition** occurs at low impact velocities when the energy of the droplet is not sufficient for the droplet to rebound. In this case, after touching the surface, the drop may present some oscillations but eventually remains stuck on the wall. No modification of the wettability of the system occurs. The drop still exhibits a Cassie-Baxter state and it can be easily removed from the solid surface by shedding.
- **Rebound** occurs when the drop is completely bounced off the wall and no water is left stuck on the surface. The SHS remains completely clean.
- **Sticking** occurs when the impact velocity triggers the transition from Cassie-Baxter to Wenzel state. Since the drop has impaled on the rough surface either it remains completely stuck on the wall or it partially rebounds. In both cases the part of the drop sticking to the surface is in a Wenzel regime.

Other known phenomena such as prompt splash or drop break up can be observed in combination with the above described outcomes. In particular, due to the effect of the impact pressure, fragmentation may occur with the formation of various secondary droplets, the behaviour of which corresponds to a Cassie-Baxter state. However, since no strong breakup is observed, it is always possible to focus on the evolution of the liquid bulk, neglecting the possible presence of secondary droplets.

Focusing on the behaviour of the main liquid droplet, drop-wall interaction can be modelled based on experimental evidence by Antonini et al. [71], who conducted a test campaign to explore the phenomenon of water drop impact on super hydrophobic surfaces. Both normal ($\varphi_i = 0$) and oblique impacts ($\varphi_i > 0$) were analysed on different surfaces and with different droplet diameters and impact velocities. The impact Weber number We_s (Eq. 4.14) was found to be the fundamental parameter influencing droplet behaviour upon impact. It was observed that for oblique impacts, if $We_s < 200$ the drop spreads on the surface and complete rebound occurs without impalement transition. For $We_s > 200$, instead, drop impalement occurs and the dynamic receding contact angle reaches values lower than 90 deg. Nevertheless, complete rebound occurs anyway, since the surface tilt has a positive effect on drop shedding, allowing the drop to rebound from the surface. Indeed, even for low tilt angles the water drops rebound completely from the surface and no secondary

drops remain attached to the substrate. As far as normal impacts are concerned, complete rebound occurs only for Weber numbers lower than the critical value of $We_s < 200$. For higher Weber numbers, instead, impalement transition occurs and only a partial rebound is observed. Most of the liquid bounces off the wall, but a small water portion remains attached to the surface in the area around the impact point. However, the occurrence of perfectly normal impacts on the airfoil in flight conditions can be reasonably neglected. Moreover, in case of oblique impacts, if deposition occurs, shedding by aerodynamic forces is sufficient to remove all water from the surface thanks to the positive effect of the tilt angle. Under these assumptions the interaction of a droplet with a SHS can be always modelled as full rebound. The droplet is completely bounced off the surface upon impact and it is reintroduced in the flow field with a new velocity given by Eq. 4.15. Hence, the rebound model by Bai and Gosman [53], which was discarded for wall interaction modelling on smooth surfaces, is recovered in order to model the droplet behaviour upon impact on super hydrophobic surfaces. The model already implemented in the PoliDrop software is thus adjusted for the considered case and simulations are carried out to evaluate the collection efficiency and the impingement limits.

5.3 Simulations and results

The possibility of applying super hydrophobic surfaces as anti-icing systems is studied on a practical case. Multiple CFD and particle tracking simulations are performed on a NACA 0012 airfoil flying at 102.8 m/s with an ambient temperature of 262.04 K and atmospheric pressure of 10^5 Pa. The airfoil has a 0.533 m chord and the computational grid is made of 149586 elements and 91843 nodes. The computation of the collection efficiency is repeated on the standard surfaces changing the angle of attack and the droplets diameter in order to evaluate the impingement limits. Two different extensions for the SHS are chosen and further simulations are performed to evaluate their effect. In order to simulate the SHS it has been necessary to create new meshes defining the airfoil boundary divided in three different parts: the upper side, the lower side and the SHS region in proximity of the leading edge of the airfoil. In this way it is possible to define different surface properties for the droplet-wall interaction and rebound is activated only for the SHS.

The first case taken into account is the airfoil at zero angle of attack with a cloud MVD of 20 μm. As the angle of attack is null, the flow field is symmetric, leading to symmetric impingement limits on the upper and lower side of the airfoil. The peak of the collection efficiency is centred in correspondence of the leading edge. Impingement limits are measured as the values of the curvilinear abscissa where the collection efficiency becomes null and they are found to be equal to $\pm$ 33.96 mm (Fig. 5.4).

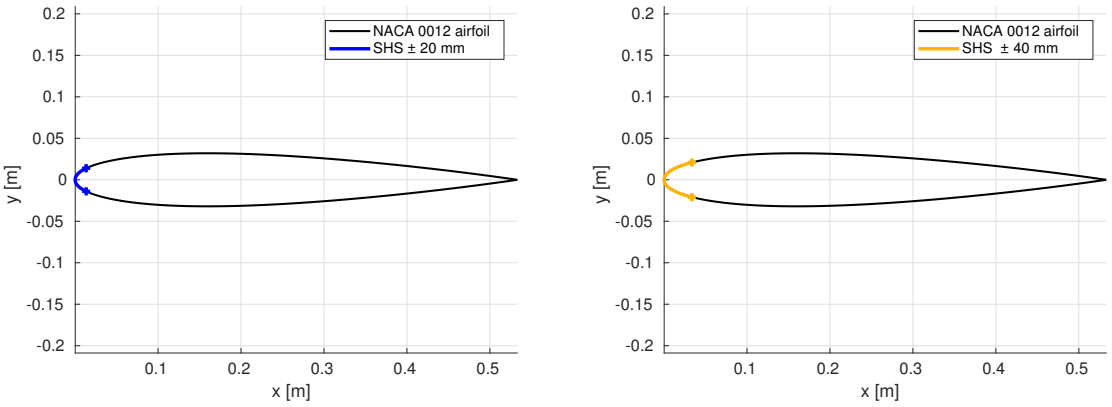

(a) (b)

Figure 5.3: NACA 0012 airfoil with different SHS extensions.

Therefore, if a super hydrophobic surface is used as an anti-icing system, it should be placed centred on the leading edge region with an extension at least equal to the impingement limits. Two different extensions of the SHS (Fig. 5.3) are implemented to study the effect of droplets rebound: the first SHS has a total extension lower than impingement limits (± 20 mm), while the second one is chosen to have a total extension higher than impingement limits (± 40 mm). Results are shown in Fig. 5.4 where the collection efficiencies for the three different cases are represented as functions of the curvilinear abscissa.

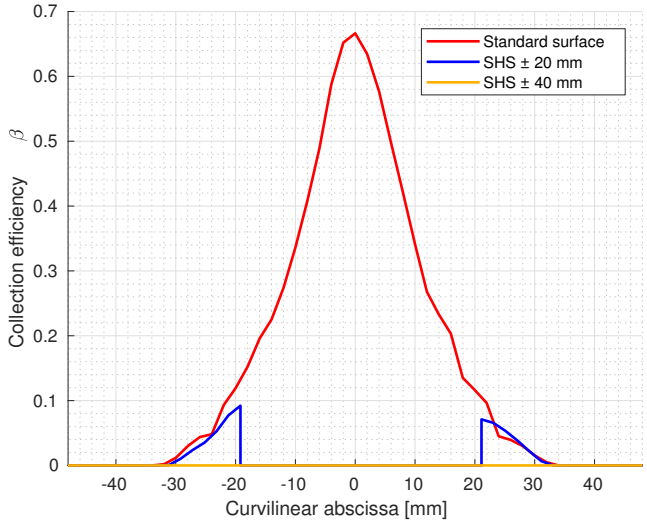

Figure 5.4: Collection efficiency as a function of the curvilinear abscissa: comparison between different extensions of the SHS for a NACA 0012 airfoil at $\alpha = 0$ deg with a cloud MVD of 20 μm.

The red curve is obtained for the standard aluminium alloy surface where only the stick and splashing interactions are allowed. Impingement limits can be identified to be equal to ± 33.96 mm, as it has been mentioned before. The yellow curve is obtained for the SHS with ± 40 mm extension, which is greater than the impingement limits and thus the collection efficiency results to be null on the whole surface, as each impacting droplet is bounced away and it does not re-impinge downstream. The blue curve instead is obtained with an intermediate extension of ± 20 mm. In this case, the collection efficiency peak is reduced to zero but two regions with non-null collection efficiency remain close to the impingement limits. This is due to the fact that close to the leading edge droplets are rebounded, but when they reach the standard aluminium surface they stick, as it is shown in Fig. 5.5. In these regions ice accretes on the surface forming two horns where bounced droplets may re-impinge, leading to an ice shape with a hole in the middle, but with two greater horns.

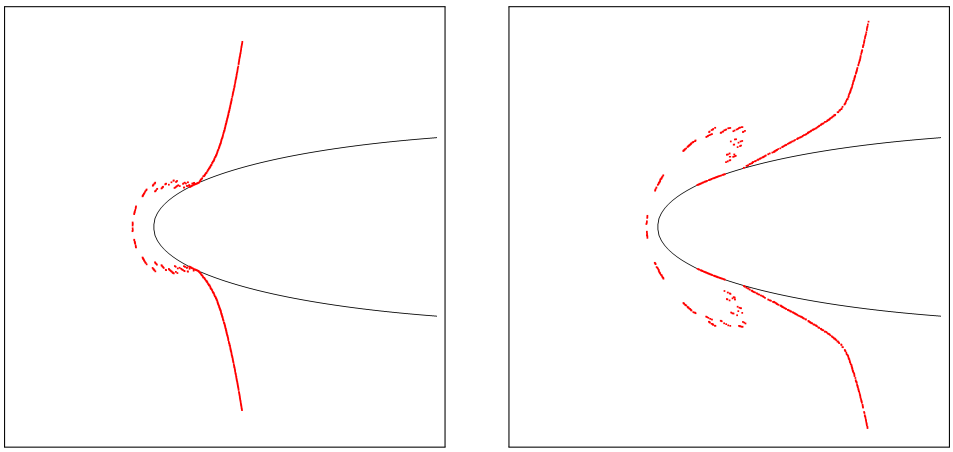

Figure 5.5: Visualisation of rebounding parcels with $d_p = 20\ \mu m$ on the leading edge of a NACA 0012 airfoil with a SHS with ± 20 mm extension.

Computed ice shapes are shown in Fig. 5.6 where comparison between the standard surface and the two SHS is performed for an exposure time of 420 s. A large amount of ice accretes on the standard surface with a maximum thickness of 13.60 mm and an irregular shape which may significantly alter the flow field. As far as the SHS are concerned, it is evident that the wider SHS manages to completely prevent ice accretion, thus fully accomplishing its scope. As regards the ± 20 mm SHS, the non-null collection efficiency results in two little horns located at the end of the SHS. As it was predicted, these two horns have a thickness which is higher than that obtained for the standard surface at the same location because of re-impingements of bounced droplets. This effect is expected to be amplified if the exposure time is increased. Indeed, as time increases, the two horns accretes and it is more likely that droplets impacts on them after rebound.

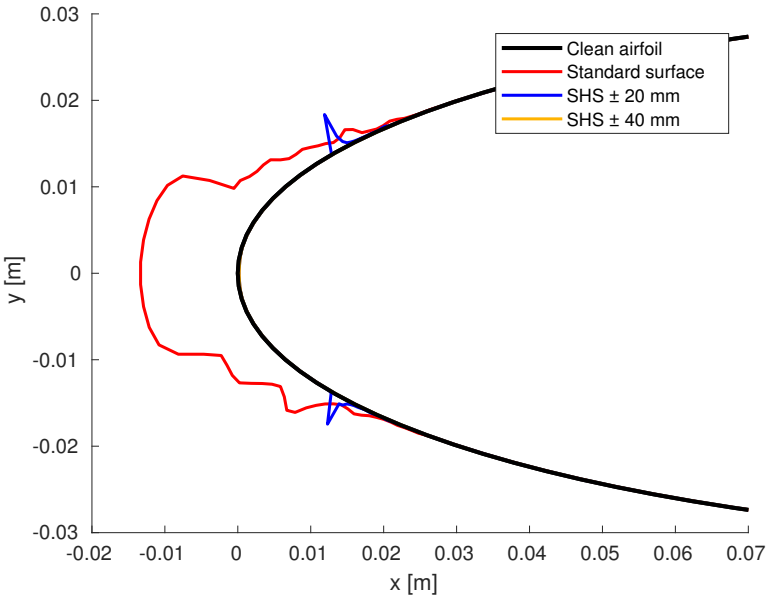

Figure 5.6: Ice shapes comparison between different extensions of the SHS for a NACA 0012 airfoil at $\alpha = 0$ deg with a cloud MVD of 20 μm.

The amount of ice accreted on the airfoil can be computed by integrating the final ice thickness along the curvilinear abscissa and multiplying this value by the ice density. A mean value between rime ice and glaze ice density is used (900 kg/m^3) and the total mass of ice per unit length is obtained for the different surfaces. Moreover, the maximum ice thickness value and its location are identified and summarised in Tab. 5.1.

	Standard surface	SHS ± 20 mm	SHS ± 40 mm
Mass $[g/m]$	247.8	8.8	0
Δ mass % $[-]$	-	-96.45	-100
Max Thickness value $[mm]$	13.60	4.56	-
Distance from leading edge s $[mm]$	0	-19.18	-

Table 5.1: Total mass of ice accreted on the airfoil and maximum thickness. Comparison between different SHS extensions at $\alpha = 0$ deg.

Airfoil performances can be compared between the three different obtained ice-shapes and results for the lift coefficient C_L and the drag coefficient C_D are reported in Tab. 5.2. Note that the ± 40 mm SHS gives the same results of the clean airfoil, since no ice accretes on the airfoil in this case. As far as the clean airfoil is concerned, the lift coefficient is nearly null as the NACA 0012 airfoil is symmetric and it is flying at zero angle of attack. However, slight asymmetries in the CFD computation are observed which lead to a non-exactly null C_L. These slight asymmetries lead also to non-perfectly symmetric ice shapes. The ice shape accreted on the standard surface

gives rise to a slightly positive lift, while the ice shape originating in the ± 20 mm SHS case leads to a slightly negative lift.

	Clean airfoil	Standard surface	SHS ± 20 mm	SHS ± 40 mm
C_L	0.000032	0.003887	-0.005134	0.000032
C_D	0.004448	0.005164	0.005421	0.004448
$\Delta\ C_D$ % [–]	-	+16.10	+21.87	0

Table 5.2: Performance degradation due to ice accretion. Comparison between different SHS extensions at $\alpha = 0$ deg.

Nevertheless, the drag coefficient C_D is the most important parameter to be considered for performance degradation in this case. It is observed in Tab. 5.2 that ice accretion increases the airfoil drag. Moreover, the two little horns formed in the ± 20 mm SHS case lead to a drag increase which is higher than that due to the consistent amount of ice accreted on the standard surface (+21.87% instead of +16.10%). Hence, the accretion of these two horns should be avoided. In order to avoid the accretion of these horns it is important that the extension of the SHS is greater than the impingement limits. However, it must be also taken into account that impingement limits change as the droplets diameter and/or the angle of attack are changed. Hence, different flight and atmospheric conditions are analysed to understand their effect on impingement limits and how they may affect the design of a proper SHS.

The first parameter to be considered is the cloud MVD. The droplets diameter is changed and simulations are repeated on the same clean airfoil and two SHS.

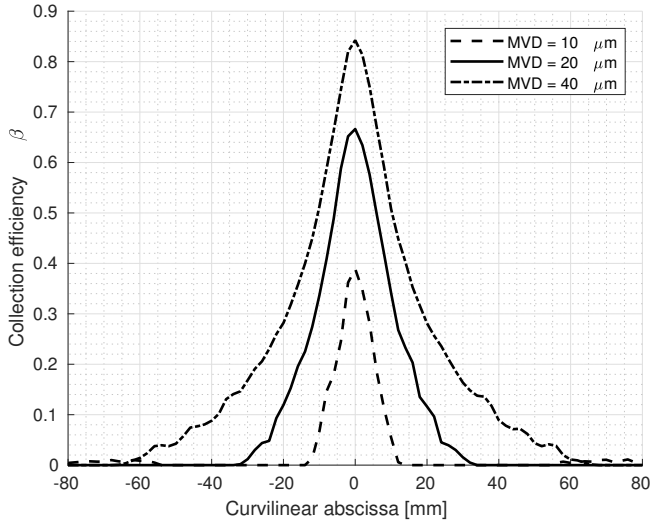

Figure 5.7: Evaluation of the effect of the cloud MVD on the collection efficiency value and impingement limits for a NACA 0012 airfoil at $\alpha = 0$ deg.

If the droplet diameter is reduced impingement limits are consequently reduced as parcels are more likely to follow streamlines and thus a smaller portion of cloud droplets impinges on the airfoil. On the contrary, an higher cloud MVD leads to higher collection efficiency and wider impingement limits as bigger droplets have higher inertia and are more likely to impact on the airfoil (Fig. 5.7). If droplets with $d_p = 10\ \mu m$ are used, impingement limits reduce to $\pm$ 13.98 mm and thus even the smallest SHS is sufficient to prevent ice accretion. Indeed, as it is shown in Fig. 5.8(a) the collection efficiency is null for both SHS. If instead the droplet diameter is doubled with respect to the reference case and droplets with a MVD of 40 μm are tracked, impingement limits are considerably increased. In this case (Fig. 5.8(b)) neither of the two surfaces is sufficient to totally avoid ice formation, since droplets impinge on the surface up to a curvilinear abscissa of $\pm$ 67.93 mm.

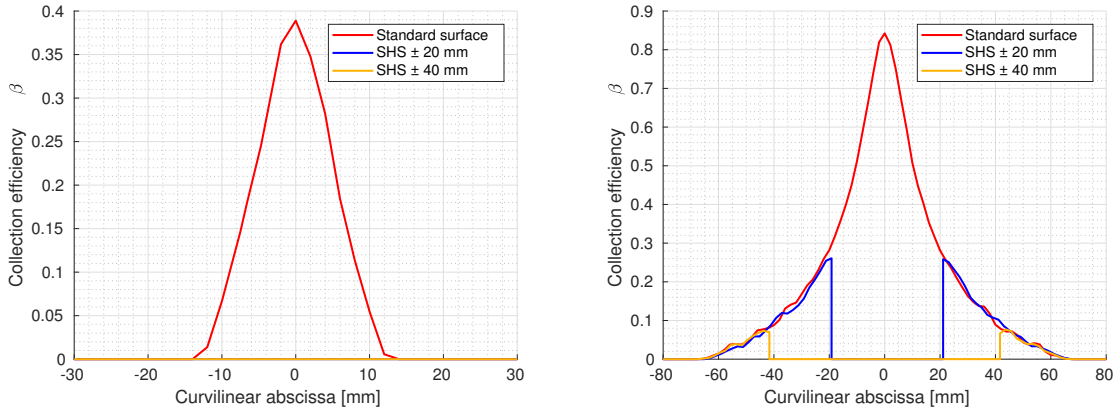

(a) MVD= 10 μm

(b) MVD= 40 μm

Figure 5.8: Collection efficiency as a function of the curvilinear abscissa: comparison between different extensions of the SHS for a NACA 0012 airfoil at $\alpha = 0$ deg for different cloud MVD.

Another important parameter to be considered when evaluating impingement limits is the asymptotic flow field velocity. Two different values are taken into account and corresponding simulations are run on the standard surface and on the two SHS. As it is shown in Fig. 5.9, impingement limits increase as V_∞ increases. This effect is due to the parcel inertia as it has been explained for the MVD case. Considering these velocities variations and comparing Fig. 5.9 with Fig. 5.7, it can be observed that halving or doubling the asymptotic speed has a much lower effect with respect to halving or doubling the MVD. This is due to the fact that the parcel momentum is proportional to the cube of the MVD and linearly proportional to the parcel speed, which is almost equal to flow field velocity. For the $V_\infty = 50$ m/s case in Fig. 5.10(a) both surfaces are sufficient to give an almost null collection efficiency on the whole surface as impingement limits are reduced to $\pm$ 25.97 mm.

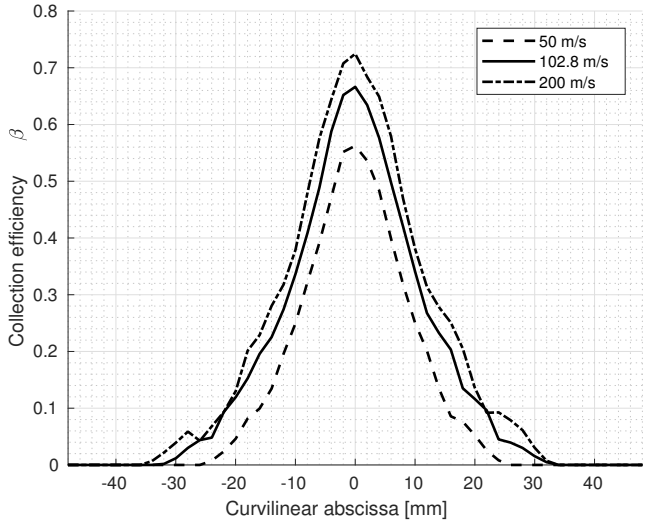

Figure 5.9: Evaluation of the effect of the asymptotic flow field velocity on the collection efficiency value and impingement limits for a NACA 0012 airfoil at $\alpha = 0$ deg with a cloud MVD of 20 μm.

On the contrary, for an asymptotic speed of 200 m/s impingement limits are not significantly changed with respect to the reference case. Since new impingement limits are increased to ± 35.96 mm, the wider SHS can still provide a null collection efficiency on the whole body, while results for the ± 20 mm SHS are qualitatively unchanged (Fig. 5.10(b)).

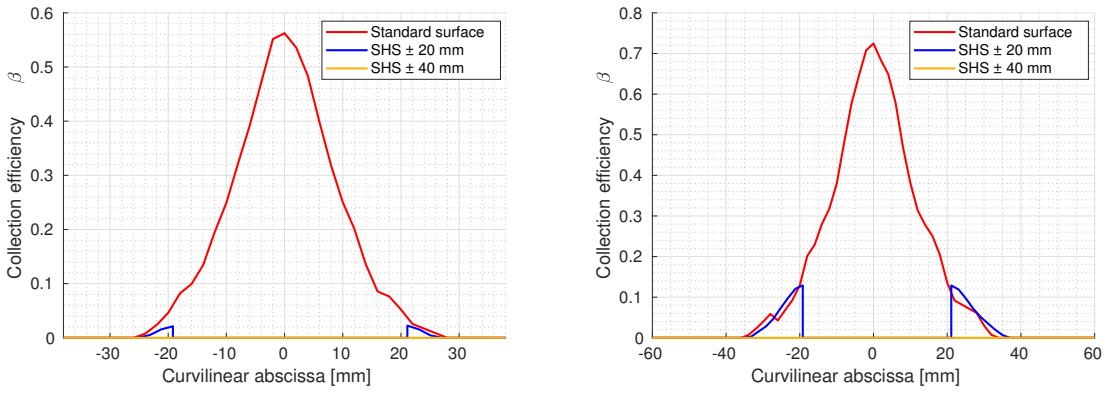

(a) $V_\infty = 50m/s$ (b) $V_\infty = 200m/s$

Figure 5.10: Collection efficiency as a function of the curvilinear abscissa: comparison between different extensions of the SHS and different V_∞ for a NACA 0012 airfoil at $\alpha = 0$ deg with a cloud MVD of 20 μm.

The last parameter influencing impingement limits considered in this work is the angle of attack. In fact, in a flight condition with non-null incidence the flow field becomes

asymmetric, consequently influencing the particle trajectories and the collection efficiency trend.

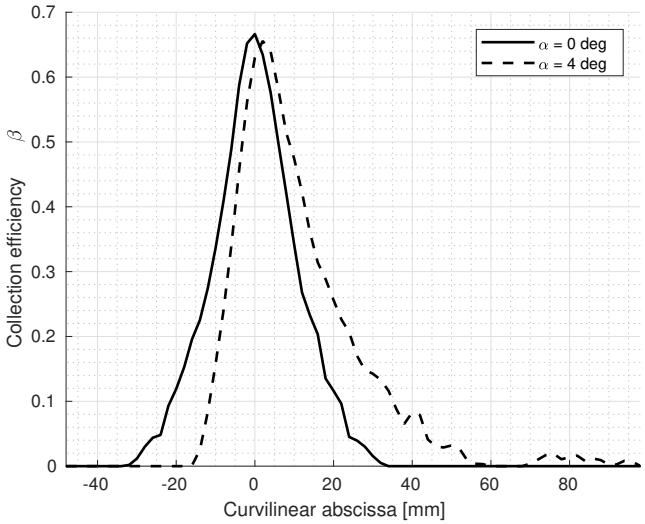

Figure 5.11: Evaluation of the effect of the angle of attack on the collection efficiency value and impingement limits for a NACA 0012 airfoil at $\alpha = 0$ deg with a cloud MVD of 20 μm.

In Fig. 5.11 and 5.12(a) results for $\alpha = 4$ deg are shown. The collection efficiency peak is displaced slightly towards the lower side and impingement limits decrease on the upper side (-17.98 mm) and increase on the lower side (+59.94 mm). For this reason the SHS is sufficient to prevent ice accretion over the upper side but it is far too limited to avoid water deposition on the lower side.

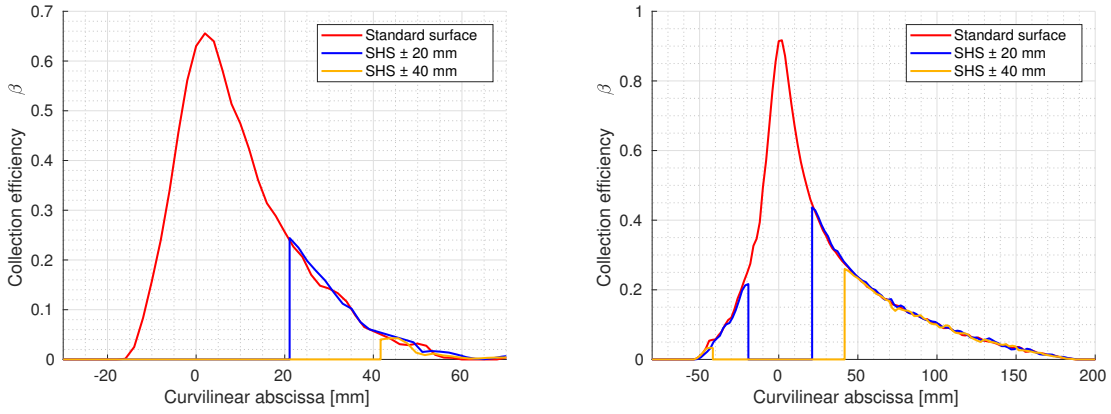

(a) MVD= 20 μm (b) MVD= 80 μm

Figure 5.12: Collection efficiency as a function of the curvilinear abscissa: comparison between different extensions of the SHS for a NACA 0012 airfoil at $\alpha = 4$ deg for different cloud MVD.

This effect is enhanced if greater droplets are considered, as it is shown in Fig. 5.12(b) where impingement limits reach the values of -53.94 mm on the upper side and +187.8 mm on the lower side. Consequently, to avoid ice accretion in these flight conditions the SHS should be extended more towards the lower side of the airfoil as the angle of attack is increased.

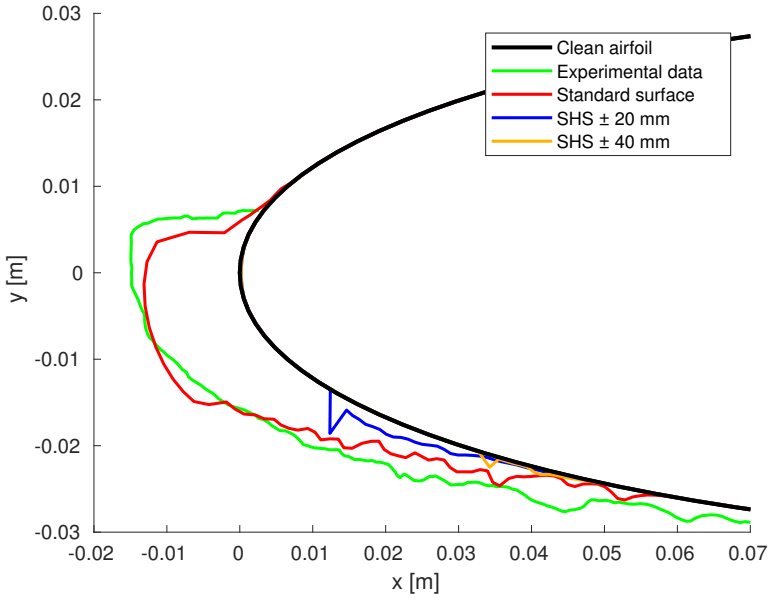

Figure 5.13: Ice shapes comparison between different extensions of the SHS for a NACA 0012 airfoil at $\alpha = 4$ deg with a cloud MVD of 20 μm.

Fig. 5.13 shows ice shapes obtained at $\alpha = 4$ deg with MVD= 20 μm. Comparison is performed between the two SHS and the standard surface. For the ice accretion over the standard surface both the numerical and experimental shape are reported (see Case 2, Sec. 2.6.1). As regards the two SHS, they both manage to avoid ice accretion in correspondence of the leading edge, but a small amount of ice accretes on the lower side of the airfoil, since impingement limits are higher than the SHS extension. However, even if ice accretion is not completely avoided, the amount of ice formed on the airfoil is considerably reduced.

	Standard surface	SHS ± 20 mm	SHS ± 40 mm
Mass $[g/m]$	313.4	37.0	8.7
Δ mass % $[-]$	-	-88.19	-97.22
Max Thickness value $[mm]$	13.57	4.65	1.44
Distance from leading edge s $[mm]$	2.0	21.1	43.64

Table 5.3: Total mass of ice accreted on the airfoil and maximum thickness. Comparison between different SHS extensions at $\alpha = 4$ deg.

Tab. 5.3 reports results for the total mass and maximum thickness of the ice accreted over the different surfaces considered. The maximum thickness location is displaced towards the lower side of the airfoil (positive curvilinear abscissa by convention) with respect to the $\alpha = 0$ deg case and the ice shapes exhibit an evident asymmetry. Moreover, as the SHS extension increases, the maximum thickness location is displaced downstream. This is due to the fact that the SHS manages to avoid ice accretion in proximity of the leading edge but water is deposited on the wall when reaching the standard surface. Thus, two horns accrete on the lower side of the airfoil, on which rebounded droplets may re-impinge. However, the mass of ice associated to these horns is considerably reduced with respect to the amount of ice accreted on the standard surface. Therefore, the SHS is effective in reducing the deposited water that may freeze on the surface and consequently the energy needed for the IPS to eliminate it.

Another aspect to be taken into account is the performance degradation due to ice accretions. In this case the symmetric airfoil has an angle of attack $\alpha = 4$ deg and the asymmetric flow field generates a non-null lift. Thus, both the C_L and the C_D are significant parameters to evaluate the performance degradation. In particular, the lift-to-drag ratio is considered as a measure of the aerodynamic efficiency. Results for the two coefficients for the clean airfoil and different ice accretions are listed in Tab. 5.4.

	Clean airfoil	Standard surface	SHS ± 20 mm	SHS ± 40 mm
C_L	0.226194	0.213030	0.227367	0.226111
C_D	0.001157	0.007095	0.001237	0.001169
C_L/C_D	195.50	30.03	183.81	193.42
$\Delta\ C_L/C_D$ % [−]	-	-84.64	-5.98	-1.06

Table 5.4: Performance degradation due to ice accretion. Comparison between different SHS extensions at $\alpha = 4$ deg.

As far as the ice accretion over the standard surface s concerned, it has a remarkable effect on the airfoil performances due to the consistent mass of ice formed around the leading edge. The lift coefficient decreases and the drag coefficient undergoes a significant increase with respect to the clean airfoil values, resulting in a huge reduction of the aerodynamic efficiency (-84.64%). On the contrary, the horns generated in the two SHS cases have a much lower effect on the performances as the amount of ice is considerably reduced thanks to super hydrophobicity. The C_D increases while the C_L is practically unaffected. In particular for the wider SHS the lift coefficient undergoes a slight decrease, while the ± 20 mm SHS leads to a modest increase in lift. This fact might be explained considering that the particular shape of the horn could have the effect of increasing the airfoil camber. Indeed, computing the flow field for the same iced airfoil at null incidence the obtained C_L is 0.019061, which is increased with respect to the corresponding value for the clean airfoil (see

Tab. 5.2). Another aspect to be considered is that the computation of the flow field around an iced airfoil becomes harder as horns and irregularities could cause recirculation problems behind them. However, in general, the trend of ice accretions is that of degrading the airfoil performances, i.e. increasing the C_D and decreasing the C_L, thus decreasing the lift-to-drag ratio. In any case, as it is shown by the per cent variation of the lift-to-drag ratio in Tab. 5.4, performances degradation is reduced as the extension of the SHS increases.

In conclusion it is possible to say that no unique extension of the SHS can be defined to be valid for every flight and atmospheric condition. Thereby, if SHS are used as the sole anti-icing system, they should be designed to be effective in the worst possible situation (i.e. higher impingement limits) considering operating ranges for the cloud MVD, the airspeed and the angle of attack. Otherwise, they can be used in addition to another standard anti-icing system in order to reduce the power needed to prevent water from freezing [68]. Indeed, as it is reported in Tab. 5.1 and Tab. 5.3, when using a SHS, a smaller amount of water is deposited on the surface, especially in correspondence of the collection efficiency peak. Thus, the mass of deposited liquid water and/or the mass of ice to be melted is considerably reduced. Moreover, Tab. 5.1 and Tab. 5.3 show that in most cases, introducing a SHS in correspondence of the wing leading edge, results in an improvement of the aerodynamic efficiency. However, in some cases the accretion of horns at the end of the SHS may affect performances, increasing the drag coefficient with respect to the ice accretion on the standard surface.

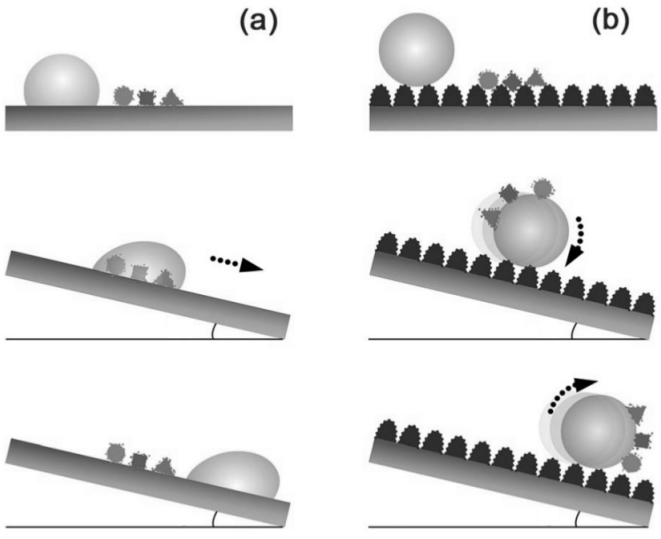

Figure 5.14: Schematic illustration of the self-cleaning mechanism (a) on a standard smooth surface, and (b) on a super hydrophobic surface. Ref. [67].

Another aspect to be considered is the difficulty of keeping the super hydrophobic surface clean. As it has been studied by Zhang et al. [67], SHS exhibit self-cleaning properties. Indeed, compared to a standard smooth surface, a water droplet on a super hydrophobic surface has a quasi-spherical shape. When the surface tilt angle is different from zero the drop rolls off the surface and it picks up external dirt particles (Fig. 5.14(b)), which show relatively strong adherence to water in comparison to a solid surface. In this way, super hydrophobic surfaces can keep their surface clean. However, this phenomenon occurs only when water droplets are shed away from the surface by aerodynamic forces. Instead, if the droplet impinges on a dirty surface its behaviour upon impact might be affected. In fact, dirt deposited on the surface may alter super hydrophobicity preventing droplets from bouncing. If this occurs, the super hydrophobic surface is not fully effective in preventing water deposition and if water freezes forming an ice layer, the surface hydrophobicity is completely overcome by the ice layer properties. However, if ice accretes on the super hydrophobic surface, ice adhesion forces are low due to the icephobicity property of SHS and shear forces needed to remove ice from the structure are reduced. Thus, although super hydrophobic coatings cannot be employed as a standalone solution to icing, they can enhance the efficiency of standard anti-icing systems and lead to a substantial reduction of the energy consumption.

Chapter 6

Conclusions and future works

In this work the ice accretion software PoliMIce was coupled with the open-source CFD solver SU2 and with PoliDrop, the lagrangian particle tracking code developed ad hoc at the Department of Aerospace Science and Technology of the Politecnico di Milano. Different ice accretion simulations were performed to assess the accuracy of the updated simulation framework and a good agreement with experimental data was found. The impingement limits and the ice layer thickness close to the stagnation point are well caught by the numerical simulations. However, discrepancies are observed in the representation of irregular shapes such as horns.

In this regard, the present thesis extended the PoliDrop software to the simulation of Supercooled Large Droplets (SLD). Indeed, comparisons of numerical results obtained applying the standard stick model with reference solutions and experimental data revealed that the standard stick model is able to predict the collection efficiency when small droplets are involved, while its reliability is reduced when considering droplets with a greater diameter. One of the issues related to SLD is that, compared to droplets with smaller diameter, they have a greater tendency to deform under the influence of aerodynamic shear forces, resulting in an increased aerodynamic drag. To account for the deformation of the droplet, an extended drag coefficient model was introduced, which computes the droplet drag coefficient as the weighted mean between the C_D of a sphere and that of a disk. However, it was found that appreciable differences with respect to the sphere model are introduced only for big particles at high relative Reynolds numbers, while no remarkable differences can be detected if the parcel relative Reynolds number is low, as it is the case in most in-flight applications. Furthermore, SLD are more likely to splash or rebound upon impact on the surface and, if this occurs, only a portion of the approaching mass is deposited at the predicted impingement location, while the splashed or rebounded mass fraction is re-introduced into the flow field. Droplet-wall interaction models were thus analysed in detail in order to give a better description of the droplet behaviour upon impact. The model proposed by Honsek and Habashi for droplet-wall interaction on liquid films was taken as a starting point for further developments. This model employs

Trujillo and Lee model for a representative description of the splashing phenomenon occurring for big droplets with an high impact velocity. Moreover, an additional splashing condition was introduced, in the light of physical considerations made by Trontin and Villedieu, in order to allow for splashing also for slow parcels impacting on the wall at low incidence angles. PoliDrop simulations revealed that the new developed splashing model lowers the collection efficiency peak in proximity of the stagnation point and brings the collection efficiency curve closer to experimental data in proximity of the impingement limits. A desirable outcome of the introduction of the splashing model was the significant improvement in the collection efficiency computation for SLD with diameters in the range between 50 and 150 μm. As far as small droplets are concerned, the resulting collection efficiency is practically unaffected with respect to the one obtained with the basic stick model and the accordance with experimental data is preserved.

Eventually, the possibility of exploiting Super Hydrophobic Surfaces (SHS) as anti-icing systems was studied. Indeed, thanks to water repellency and high droplet mobility, liquid drops show low adhesion on the super hydrophobic coating and consequently a low amount of water is deposited on the body surface. The rebound model by Bai and Gosman was used to simulate the behaviour of a liquid droplet impinging on SHS. PoliDrop simulations were run changing the angle of attack, the diameter of the droplets and the extension of the SHS. As expected, it was found that no unique extension of the SHS can meet the operational requirements for every flight and atmospheric condition. However, in order for a SHS to be effective as the sole anti-icing system, it is important that its extension is greater than the widest possible impingement limits. Indeed, from ice accretion simulations it resulted that, even if the mass of ice formed on the surface is considerably reduced, the accretion of horns at the interface between the unprotected surface and the super hydrophobic coating may lead to a degradation of the performances. As an alternative, SHS can be used in addition to other standard anti-icing systems in order to reduce the power needed to fully evaporate the water deposited on the surface. For a proper simulation of this condition, it would be necessary to modify the icing model in order to take into account the presence of an anti-icing system, imposing a specific value of the heat flux or of the surface temperature at the wall.

Another recommendation for further investigation is the modelling of the flow of the water layer. In the current implementation the water layer is assumed to have constant thickness (100 μm) and to flow in the direction of the wall shear stress, regardless of its intensity. Improvement of the predicted ice shapes could be achieved by adding terms modelling the water layer dynamics, including the accumulation and the reduction of the water content of a cell if the shear stress changes in module or in direction. These modifications of the current model are expected to lead to higher accuracy in the description of run-back ice conditions, enabling the simulation of rivulets and post de-icing situations in case a full-evaporative system is not available. This aspect is of particular interest in case of SLD conditions. In fact, since a

large amount of supercooled liquid water is intercepted by the aircraft, it is likely that the ice protection system cannot provide enough energy to fully clear ice and liquid water and run-back ice problems may appear. Multi-zone models could also be developed in order to account for the different local characteristics and surface roughness conditions of the accreted ice. In this context, a coupling between the ice accretion tool and particle tracking software might be necessary, in order to modify wall interaction conditions on the basis of the properties of the iced surface and of the presence of the liquid layer.

The geometry deformation and mesh update modules of the code should also be considered for future developments. In this work, ice accretion simulations were run deforming the body geometry along the normal direction computed on the clean surface. This expedient was adopted in order to avoid front collisions in the grid generation process, but it prevents the correct representation of complex ice shapes. Thus, it would be necessary to fix meshing issues in order to accrete the ice along the normal direction computed on the iced configuration. Moreover, mesh generation is performed at each time step starting from the updated geometry, using a tool which is suitable only for two dimensional cases. In order to treat three dimensional problems, a different meshing tool should be employed. Otherwise, the implementation of a mesh morphing algorithm could be considered, which would also lead to a considerable reduction of the computational time.

Bibliography

[1] F.T. Lynch and A. Khodadoust. Effects of ice accretions on aircraft aerodynamics. *Progress in Aerospace Sciences*, 37(8):669–767, 2001.

[2] W.J. Baars, R.O. Stearman, and C.E. Tinney. A Review on the Impact of Icing on Aircraft Stability and Control. *Journal of Aeroelasticity and Structural Dynamics*, 2(1), 2010.

[3] D. Lou and D.W. Hammond. Heat and mass transfer for ice particle ingestion inside aero-engine. *Journal of Turbomachinery*, 133(3):031021, 2011.

[4] N. Dalili, A. Edrisy, and R. Carriveau. A review of surface engineering issues critical to wind turbine performance. *Renewable and Sustainable Energy Reviews*, 13(2):428–438, 2009.

[5] L. Makkonen. Modeling power line icing in freezing precipitation. *Atmospheric Research*, 46(1-2):131–142, 1998.

[6] M.B. Bragg, A.P. Broeren, and L.A. Blumenthal. Iced-airfoil aerodynamics. *Progress in Aerospace Sciences*, 41(5):323–362, 2005.

[7] Helicopter magazine. `https://www.helicoptersmagazine.com`.

[8] B.J. Mason. *The physics of clouds*. Clarendon press: Oxford University Press, 1971.

[9] T. Cebeci and F. Kafyeke. Aircraft icing. *Annual review of fluid mechanics*, 35(1):11–21, 2003.

[10] R.W. Gent, N.P. Dart, and J.T. Cansdale. Aircraft icing. *Philosophical Transactions of the Royal Society of London A: Mathematical, Physical and Engineering Sciences*, 358(1776):2873–2911, 2000.

[11] E. Linacre and B. Geerts. Cloud liquid water content, drop sizes, and number of droplets. `http://www-das.uwyo.edu/~geerts/cwx/notes/chap08/moist_cloud.html`, 1999.

[12] B.L. Messinger. Equilibrium temperature of an unheated icing surface as a function of air speed. *Journal of the Aeronautical Sciences*, 20(1):29–42, 1953.

[13] Ice accretion simulation on wings. `http://www.enginsoft.it/applications/aerospace/ice.html`.

[14] Modeling What's Cool. `http://www.nasa.gov/offices/oct/home/tech_life_kestrel_prt.htm`.

[15] Icing conditions in flight. `http://www.pilotfriend.com/safe/safety/icing_conditions.htm`.

[16] W. Wright. User's manual for LEWICE version 3.2. 2008.

[17] I. Paraschivoiu and F. Saeed. Ice accretion simulation code CANICE. In *Technical Report, International Aerospace Symposium, Bucharest, Romania*, 2001.

[18] T. Hedde and D. Guffond. ONERA three-dimensional icing model. *AIAA journal*, 33(6):1038–1045, 1995.

[19] R.W. Gent. TRAJICE 2, A combined water droplet and ice accretion prediction program for aerofoil. In *Royal Aerospace Establishment(RAE) Technical Rept. TR 90054, Farnborough, Hampshire*, 1990.

[20] F. Morency, H. Beaugendre, G. Baruzzi, and W. Habashi. FENSAP-ICE – A comprehensive 3D simulation system for in-flight icing. In *15th AIAA Computational Fluid Dynamics Conference*, page 2566, 2001.

[21] G. Mingione, V. Brandi, and B. Esposito. Ice accretion prediction on multielement airfoils. *Journal of Aircraft*, 35(2):240–246, 1998.

[22] G. Gori, M. Zocca, M. Garabelli, A. Guardone, and G. Quaranta. PoliMIce: A simulation framework for three-dimensional ice accretion. *Applied Mathematics and Computation*, 267:96–107, 2015.

[23] F. Palacios, M.R. Colonno, A.C. Aranake, A. Campos, S.R. Copeland, T.D. Economon, A.K. Lonkar, T.W. Lukaczyk, T.W.R. Taylor, and J.J. Alonso. Stanford University Unstructured (SU2): An open-source integrated computational environment for multi-physics simulation and design. *AIAA Paper*, 287:2013, 2013.

[24] SU2. The Open-Source CFD code. `https://su2code.github.io/`.

[25] M. Garabelli and G. Gori. PoliMIce: un ambiente di simulazione per la previsione dell'accrescimento di ghiaccio su velivoli. Master's thesis, Politecnico di Milano, 2013.

[26] T.G. Myers. Extension to the Messinger model for aircraft icing. *AIAA journal*, 39(2):211–218, 2001.

[27] J. Stefan. Über die Theorie der Eisbildung, insbesondere über die Eisbildung im Polarmeere. *Annalen der Physik*, 278(2):269–286, 1891.

[28] G. Gori, M. Zocca, G. Parma, and A. Guardone. A model for in-flight ice accretion based on the exact solution of the unsteady Stefan problem. 2015.

[29] S. Rebay. Efficient unstructured mesh generation by means of Delaunay triangulation and Bowyer-Watson algorithm. *Journal of computational physics*, 106(1):125–138, 1993.

[30] D. Dussin, M. Fossati, A. Guardone, and L. Vigevano. Hybrid grid generation for two-dimensional high-Reynolds flows. *Computers & Fluids*, 38(10):1863–1875, 2009.

[31] J. Shin and T.H. Bond. Results of an Icing test on a NACA 0012 airfoil in the NASA Lewis Icing Research Tunnel. 1992.

[32] J. Shin and T.H. Bond. Experimental and computational ice shapes and resulting drag increase for a NACA 0012 airfoil. 1992.

[33] R.W. Gent. TRAJICE2-A combined water droplet trajectory and ice accretion prediction program for aerofoils. *RAE TR-90054, Nov.*, 1990.

[34] Y. Bourgault, W.G. Habashi, J. Dompierre, and G.S. Baruzzi. A finite element method study of eulerian droplets impingement models. *International Journal for Numerical methods in fluids*, 29(4):429–449, 1999.

[35] R. Clift, J.R. Grace, and M.E. Weber. *Bubbles, drops, and particles*. Courier Corporation, 2005.

[36] L. Quartapelle and F. Auteri. *Fluidodinamica incomprimibile*. Casa editrice ambrosiana, 2013.

[37] D. Sangaletti. Un modello semplificato per l'accrescimento di ghiaccio su profili alari oscillanti. Master's thesis, Politecnico di Milano, 2017.

[38] M. Papadakis, K. E Hung, G.T. Vu, H.W. Yeong, C.S. Bidwell, M.D. Breer, and T.J. Bencic. Experimental investigation of water droplet impingement on airfoils, finite wings, and an s-duct engine inlet. 2002.

[39] P.R. Spalart and S.R. Allmaras. A one-equation turbulence model for aerodynamic flows. In *30th aerospace sciences meeting and exhibit*, page 439, 1992.

[40] Code of Federal Regulations. 14 CFR 25.1419-1420, Revised as of Nov. 4, 2014.

[41] Public Inquiries Section. Aircraft Accident Report: in-flight icing encounter and loss of control, Simmons Airlines, d.b.a. Americal Eagle flight 4184, Avions de Transport Regional (ATR) model 72-212, N401AM, Roselawn, Indiana, October 31, 1994. Technical report, National Transportation Safety Board, 1996.

[42] T. Hu, Y. Li, H. Lv, and B. Tian. Study on airworthiness problems of operating in supercooled large drops icing conditions for transport category airplanes. *Procedia Engineering*, 80:467–478, 2014.

[43] Federal Aviation Administration. Federal Register Vol. 79 No. 213, 14 CFR Parts 25 and 33, Airplane and Engine Certification Requirements in Supercooled Large Drop, Mixed Phase, and Ice Crystal Icing Conditions; Final Rule. Technical report, Department of Transportation, 2014.

[44] Y. Yuan and T.R. Lee. Contact angle and wetting properties. In *Surface science techniques*, pages 3–34. Springer, 2013.

[45] Science for all Brainwaves. `http://www.sciencebrainwaves.com/ultra-ever-dry/`.

[46] T. Petrova and R.B. Dooley. Revised release on surface tension of ordinary water substance. *The International Association for the Properties of Water and Steam, IAPWS, Moscow, Russia*, 2014.

[47] R. Mareš and J. Kalová. The experimental determination of surface tension of supercooled water. In *EPJ Web of Conferences*, volume 67, page 02072. EDP Sciences, 2014.

[48] T. Kékesi, G. Amberg, and L.P. Wittberg. Drop deformation and breakup. *International Journal of Multiphase Flow*, 66:1–10, 2014.

[49] R. Honsek and W.G. Habashi. FENSAP-ICE: Eulerian modeling of droplet impingement in the SLD regime of aircraft icing. *AIAA Paper*, 465:2006, 2006.

[50] A.L. Yarin. Drop impact dynamics: splashing, spreading, receding, bouncing.... *Annu. Rev. Fluid Mech.*, 38:159–192, 2006.

[51] R. Rioboo, C. Tropea, and M. Marengo. Outcomes from a drop impact on solid surfaces. *Atomization and Sprays*, 11(2), 2001.

[52] R. Rioboo, M. Marengo, and C. Tropea. Time evolution of liquid drop impact onto solid, dry surfaces. *Experiments in fluids*, 33(1):112–124, 2002.

[53] C. Bai and A.D. Gosman. Development of methodology for spray impingement simulation. Technical report, SAE Technical Paper, 1995.

[54] P. Brambilla and A. Guardone. Automatic tracking of corona propagation in three-dimensional simulations of non-normal drop impact on a liquid film. *Computing*, 95(5):415–424, 2013.

[55] R. Rioboo, C. Bauthier, J. Conti, M. Voué, and J. De Coninck. Experimental investigation of splash and crown formation during single drop impact on wetted surfaces. *Computing*, 35:648–652, 2003.

[56] M.F. Trujillo, W.S. Mathews, C.F. Lee, and J.E. Peters. Modelling and experiment of impingement and atomization of a liquid spray on a wall. *International Journal of Engine Research*, 1(1):87–105, 2000.

[57] G. Cossali, A. Coghe, and M. Marengo. The impact of a single drop on a wetted solid surface. *Experiments in fluids*, 22(6):463–472, 1997.

[58] J. Shu and D. Zhu. A numerical study of Supercooled Large Droplets' impingement on airfoils. In *23rd AIAA Computational Fluid Dynamics Conference*, page 4291, 2017.

[59] A.L. Yarin and D.A. Weiss. Impact of drops on solid surfaces: self-similar capillary waves, and splashing as a new type of kinematic discontinuity. *Journal of Fluid Mechanics*, 283:141–173, 1995.

[60] C.D. Stow and R.D. Stainer. The physical products of a splashing water drop. *Journal of the Meteorological Society of Japan*, 55(5):518–531, 1977.

[61] C.H.R. Mundo, M. Sommerfeld, and C. Tropea. Droplet-wall collisions: experimental studies of the deformation and breakup process. *International journal of multiphase flow*, 21(2):151–173, 1995.

[62] M. Papadakis, S.C. Wong, A. Rachman, K.E. Hung, G.T. Vu, and C.S. Bidwell. Large and small droplet impingement data on airfoils and two simulated ice shapes. 2007.

[63] G. Cossali, A. Bisighini, C. Tropea, and I. Roisman. Single drop impact onto a deep pool: experimental observations and theoretical model for the crater evolution. In *23rd Annual Conference on Liquid Atomization and Spray Systems (ILASS–Europe 2010)*. ILASS-Europe, 2010.

[64] W.C. Macklin and G.J. Metaxas. Splashing of drops on liquid layers. *Journal of applied physics*, 47(9):3963–3970, 1976.

[65] P. Trontin and P. Villedieu. Revisited Model for Supercooled Large Droplet Impact onto a Solid Surface. *Journal of Aircraft*, 2016.

[66] W. Barthlott and C. Neinhuis. Purity of the sacred lotus, or escape from contamination in biological surfaces. *Planta*, 202(1):1–8, 1997.

[67] Y. Zhang, H. Xia, E. Kim, and H. Sun. Recent developments in superhydrophobic surfaces with unique structural and functional properties. *Soft Matter*, 8(44):11217–11231, 2012.

[68] C. Antonini, M. Innocenti, T. Horn, M. Marengo, and A. Amirfazli. Understanding the effect of superhydrophobic coatings on energy reduction in anti-icing systems. *Cold Regions Science and Technology*, 67(1-2):58–67, 2011.

[69] C. Antonini, F. Villa, I. Bernagozzi, A. Amirfazli, and M. Marengo. Drop rebound after impact: The role of the receding contact angle. *Langmuir*, 29(52):16045–16050, 2013.

[70] D. Quéré. Non-sticking drops. *Reports on Progress in Physics*, 68(11):2495, 2005.

[71] C. Antonini, F. Villa, and M. Marengo. Oblique impacts of water drops onto hydrophobic and superhydrophobic surfaces: outcomes, timing, and rebound maps. *Experiments in fluids*, 55(4):1713, 2014.

[72] A.B.D. Cassie and S. Baxter. Wettability of porous surfaces. *Transactions of the Faraday society*, 40:546–551, 1944.

[73] R.N. Wenzel. Resistance of solid surfaces to wetting by water. *Industrial & Engineering Chemistry*, 28(8):988–994, 1936.

[74] D. Bartolo, F. Bouamrirene, E. Verneuil, A. Buguin, P. Silberzan, and S. Moulinet. Bouncing or sticky droplets: Impalement transitions on superhydrophobic micropatterned surfaces. *EPL (Europhysics Letters)*, 74(2):299, 2006.

[75] R. Rioboo, M. Voué, A. Vaillant, and J. De Coninck. Drop impact on porous superhydrophobic polymer surfaces. *Langmuir*, 24(24):14074–14077, 2008.

Ringraziamenti

Arrivati alla fine di questo lavoro di tesi è giunto il momento di ringraziare tutte le persone che hanno reso possibile questa esperienza e mi sono state vicine durante il percorso. Persone che hanno alleviato la fatica di un lungo percorso stimolante, ma anche impervio e spesso in salita e che hanno contribuito al raggiungimento di questa tappa conclusiva. Ma non è facile ringraziare tutti in una pagina o poco più senza correre il rischio di tralasciare qualcuno o risultare banale.
In primis vorrei ringraziare coloro che hanno contribuito direttamente a questo lavoro di tesi, dandomi la possibilità di mettermi alla prova con un lavoro di ricerca interessante e di confrontarmi con l'ambito accademico in un ambiente sereno e stimolante. In particolare il prof. *Alberto Guardone* per avermi consigliata e guidata nella giusta direzione, spronandomi sempre a fare meglio. *Marta* per la sua disponibilità e i suoi preziosi consigli. *Gianluca* per il suo costante supporto e infinita pazienza dal primo all'ultimo giorno senza i quali questo lavoro di tesi non sarebbe stato quello che è. Grazie al loro esempio ho imparato davvero molto.
Non posso poi dimenticare di ringraziare tutti gli *amici conosciuti all'università* in questi cinque anni, quelli ancora vicini e quelli ormai lontani, al fianco dei quali ho percorso questo cammino. Amici che hanno sempre allietato le giornate di lezione con la loro presenza, le chiacchiere e le risate contagiose e con cui ho condiviso il peso dello studio intenso prima degli esami. Insieme abbiamo superato ostacoli che a volte ci sembravano insormontabili, senza mai farci mancare il buonumore.
Grazie anche agli *amici di sempre*, che anche se non hanno contribuito direttamente a questo lavoro, sono sempre stati presenti. Anche se i diversi percorsi della vita ci hanno portato ad allontanarci, i momenti passati insieme sono sempre i più divertenti.
Un ringraziamento particolare va a *Matteo*, che è sempre stato presente in questi ultimi due anni. Insieme abbiamo affrontato questo percorso supportandoci e sopportandoci l'un l'altro e aiutandoci a vicenda, sia emotivamente che tecnicamente, a superare le difficoltà di questo lavoro di tesi. La sua costante presenza è stata un rifugio nei momenti difficili e un raggio di sole nei momenti di svago.

Infine, ma più importanti di tutti, i ringraziamenti alla mia famiglia. Ad *Andrea*, fratello, amico, complice e compagno di avventure e di litigi. Che mi ha sempre sopportata e con la sua infinita energia mi ha dato la carica e mi ha spinta a puntare in alto. A *mamma* e *papà* senza i quali non sarei qui oggi. Perché se sono la persona che sono è merito loro, che hanno stimolato la mia curiosità fin da piccola e che hanno sempre creduto in me, costruendo la fiducia in me stessa che mi ha permesso di portare a termine questo cammino. Che mi sono sempre stati accanto supportandomi e confortandomi, ma lasciandomi libera di scegliere la mia strada. Che non mi hanno mai fatto mancare nulla. A loro dedico questo lavoro con infinita gratitudine.

Giorgia
Milano, Aprile 2018